EUSKAL HERRIKO UNIBERTSITATEA - UNIVERSIDAD DEL PAIS VASCO

MATERIALEN FISIKA SAILA - DEPARTAMENTO DE FÍSICA DE MATERIALES

Functional Hybrid Thin Film Coatings for Antimicrobial, Photocatalytic, and Agricultural Applications

Marina Borraz Casanova

PhD Thesis

Thesis supervisors:

Prof. Dr. Mato Knez

Dra. Catalina Mansilla Sánchez

Donostia-San Sebastián, 2025

This PhD thesis has been carried out at:

CIC nanoGUNE

Nanomaterials group

Donostia-San Sebastián, Spain

Coating Technologies

Donostia-San Sebastián, Spain

RESUMEN

El trabajo recogido dentro de esta tesis doctoral se centra en el estudio y desarrollo de materiales híbridos orgánico-inorgánicos mediante técnicas de deposición en fase vapor, específicamente Atomic Layer Deposition (ALD) y Molecular Layer Deposition (MLD), así como su combinación. El objetivo general ha sido diseñar y obtener recubrimientos funcionales con propiedades antibacterianas, antifúngicas, fotocatalíticas y de utilidad potencial en aplicaciones agrícolas como la germinación de semillas, todo ello desde una aproximación fundamentada tanto en la investigación básica como en su aplicabilidad industrial.

Las técnicas de MLD y ALD/MLD, basadas en reacciones químicas secuenciales y autocontroladas, permiten el crecimiento de películas nanométricas con un control muy riguroso del espesor y la composición, incluso sobre superficies con geometrías complejas. La estrategia ALD/MLD combinada permite, además, la síntesis de materiales híbridos que integran componentes orgánicos e inorgánicos con propiedades sinérgicas.

El primer bloque experimental de esta tesis se centró en la síntesis de películas delgadas de poliamida 6,3 (PA63) mediante MLD, utilizando cloruro de malonilo (MC) y hexametilendiamina (HD) como precursores orgánicos. La deposición se realizó a diferentes temperaturas y fue cuidadosamente caracterizada mediante técnicas como XRR (Reflectividad de Rayos X), ATR-FTIR (Espectroscopía Infrarroja con Reflexión Total Atenuada), QCM (Microbalanza de Cristal de Cuarzo), y XPS (Espectroscopía de Fotoelectrones de Rayos X). Se realizó un estudio de su estabilidad química frente a ácidos y bases. Estas técnicas confirmaron la formación homogénea de las películas y permitieron determinar su composición, grosor, grado de crecimiento por ciclo, y estabilidad química.

Posteriormente, se desarrollaron materiales híbridos combinando estos precursores orgánicos con precursores inorgánicos como dietilzinc (DEZ) o tetracloruro de titanio ($TiCl_4$) y agua (H_2O), logrando la formación de estructuras orgánico-inorgánicas denominadas “metalcones”, con propiedades sinérgicas. Las películas híbridas fueron también caracterizadas estructural y químicamente, mostrando buena calidad superficial y una integración eficaz de ambos componentes en el caso del hibrido MC-Zn, formado a partir de cloruro de malonilo (MC), dietilzinc (DEZ) y H_2O.

Una parte fundamental del trabajo fue evaluar el potencial antibacteriano de los recubrimientos obtenidos. Se realizaron ensayos con cepas modelo de bacterias Gram-positivas (*Staphylococcus*

aureus) y Gram-negativas (*Escherichia coli*), demostrando que tanto las películas de PA63 como el material hibrido MC-Zn lograban una reducción significativa en la adhesión y proliferación bacteriana.

Además, se realizaron ensayos antifúngicos utilizando el hongo filamentoso *Aspergillus nidulans*, un organismo ampliamente distribuido y termotolerante, ideal para evaluar recubrimientos expuestos a ambientes variables. Se realizaron dos tipos de pruebas: una enfocada en la inhibición del crecimiento radial de las hifas, y otra en la germinación de esporas. Los resultados mostraron una capacidad antifúngica limitada, lo que pone de manifiesto la necesidad de profundizar en la investigación en este ámbito.

En paralelo, se realizaron ensayos de resistencia al moho (antimoho), simulando diferentes condiciones. Las superficies recubiertas mostraron una notable resistencia al desarrollo de colonias de moho en comparación con los controles sin recubrimiento, lo cual refuerza su aplicabilidad en ambientes húmedos, como ocurre en el envasado de productos frescos o en contextos agrícolas.

Otro aspecto innovador de la tesis fue la aplicación de estos recubrimientos en el proceso de germinación de semillas. Se realizaron ensayos colocando semillas de lenteja sobre muestras de algodón recubiertas con las películas desarrolladas. Se evaluó la germinación en términos de tiempo, viabilidad, desarrollo del brote y resistencia a la formación de moho. Los recubrimientos no impidieron la germinación y, en algunos casos, mejoraron las condiciones sanitarias del entorno de crecimiento. Estos resultados apuntan a una posible utilidad en tecnologías de recubrimiento de semillas, orientadas a mejorar la protección y rendimiento agrícola sin recurrir a pesticidas químicos.

Una segunda línea de trabajo abordada en la tesis fue la fabricación de recubrimientos híbridos sobre sustratos vítreos, utilizando una estrategia combinada de ALD y MLD con precursores de titanio y espaciadores orgánicos (etilenglicol, glicerol y hidroquinona). Estos recubrimientos, tras tratamientos térmicos específicos, permitieron la eliminación de la fase orgánica y la generación de estructuras porosas de TiO_2 con alta cristalinidad tipo anatasa. Estas películas porosas fueron evaluadas por su actividad fotocatalítica en la degradación de NO bajo irradiación UV, conforme a la norma ISO 22197-1:2007. Los recubrimientos mostraron actividad sostenida en múltiples ciclos de prueba, evidenciando su potencial para aplicaciones en la purificación del aire y eliminación de contaminantes atmosféricos.

Como parte de la colaboración industrial, con la empresa Ctechnano, se evaluó un prototipo de reactor ALD con cámara de volumen ajustable, diseñado para permitir deposiciones en

fracciones independientes o combinadas. El sistema fue validado mediante ensayos de deposición con Al_2O_3 y ZnO, evaluando la homogeneidad del crecimiento, la influencia del volumen y la necesidad de aislamiento físico entre zonas. El diseño flexible de la cámara demostró ser efectivo para estudios comparativos, optimización de parámetros y escalabilidad industrial.

La tesis se completa con un capítulo dedicado a la colaboración industrial con la empresa, se participó en proyectos de funcionalización de superficies, desarrollo de soluciones a medida para clientes y transferencia tecnológica. Se incluyeron trabajos aplicados sobre madera deslignificada, tejidos, plásticos y otros materiales con requerimientos específicos. Parte de los resultados de esta colaboración son confidenciales por motivos de propiedad industrial, pero se documenta de forma transparente toda la información susceptible de ser divulgada.

ABSTRACT

The work presented in this doctoral thesis elaborates on the development of organic–inorganic hybrid materials through vapor-phase deposition techniques, specifically Molecular Layer Deposition (MLD) and the combined Atomic Layer Deposition/Molecular Layer Deposition (ALD/MLD) strategy. The research is oriented toward the fabrication of functional coatings with antibacterial, antifungal, and photocatalytic properties, with a clear emphasis on real-world applications in fields such as food packaging and agriculture.

MLD and ALD/MLD techniques enable precise engineering of thin films at the nanometer scale, thanks to the sequential and self-limiting nature of the surface reactions involved. These methods allow for uniform deposition of materials even on complex substrates, offering atomic-level control over thickness, composition, and structure.

The first experimental section of this thesis focused on the synthesis of polyamide 6,3 (PA63) thin films via MLD, using malonyl chloride (MC) and hexamethylenediamine (HD) as organic precursors. Depositions were carried out at various temperatures and thoroughly characterized using techniques such as X-ray Reflectivity (XRR), Attenuated Total Reflectance Fourier-Transform Infrared Spectroscopy (ATR-FTIR), Quartz Crystal Microbalance (QCM), and X-ray Photoelectron Spectroscopy (XPS). Subsequently, hybrid materials were developed by combining these organic precursors with inorganic ones such as diethylzinc (DEZ) or titanium tetrachloride ($TiCl_4$) and water (H_2O), yielding organic–inorganic compositions known as “metalcones,” which exhibited synergistic properties.

A key component of this work involved evaluating the antibacterial potential of the resulting coatings. Tests were conducted using model strains of Gram-positive (Staphylococcus aureus) and Gram-negative (Escherichia coli) bacteria, demonstrating that both PA63 films and hybrid materials achieved a significant reduction in bacterial adhesion and proliferation. In addition, antifungal assays were carried out using the filamentous fungus Aspergillus nidulans, a thermotolerant and widely distributed organism suitable for evaluating coatings under variable environmental conditions. The results showed limited antifungal efficacy, highlighting the need for further research in this area.

In parallel, mold-resistance (antimildew) tests were performed under simulated environmental conditions. Coated surfaces exhibited notable resistance to mold colony development compared to uncoated controls, reinforcing their applicability in humid environments such as fresh goods packaging or agricultural contexts.

Another innovative aspect of the thesis was the application of these coatings in seed germination processes. Coated cotton was used as a substrate for lentil germination, evaluating not only antifungal performance but also the impact on seed viability and germination speed. The results were positive: the coatings did not inhibit germination and, in some cases, improved seed protection against environmental contamination. These findings demonstrate the potential of the ALD/MLD approach in sustainable agricultural applications, such as seed coating or treated soils.

A second line of work in the thesis focused on the fabrication of hybrid TiO_2 coatings on glass substrates using a combined ALD/MLD strategy with various organic spacers (ethylene glycol, glycerol, hydroquinone) and inorganic precursors such as $TiCl_4$ and H_2O. After thermal treatments, the organic phase was removed, leading to the formation of porous TiO_2 structures with anatase crystallinity. These porous films were evaluated for their photocatalytic activity in NO degradation under UV irradiation, in accordance with ISO 22197-1:2007. The coatings showed sustained activity over multiple test cycles, demonstrating their potential for air purification and atmospheric pollutant removal.

As part of the industrial collaboration with the company Ctechnano, an ALD reactor prototype with an adjustable-volume chamber was evaluated. This system was designed to allow depositions in independent or combined reactor volume fractions. It was validated through deposition tests using Al_2O_3 and ZnO, assessing film growth under different conditions. The flexible design of the chamber proved effective for comparative studies, parameter optimization, and industrial scalability. In addition, participation in applied projects, client services, and the development of functional surface solutions with real industrial applications—including the functionalization of wood, plastics, and textiles—enabled validation of the ALD/MLD approach in industrial settings, addressing practical aspects such as scalability, reproducibility, and technology transfer.

Contents

LIST OF FIGURES

LIST OF TABLES

ABBREVIATIONS

ALCVD: Atomic Layer Chemical Vapor Deposition

ALD: Atomic Layer Deposition

ALE: Atomic layer epitaxy

AMM: *Aspergillus* minimal culture medium

ATCC: American Type Culture Collection

ATR: Attenuated Total Reflection

ATR-FTIR: Attenuated Total Reflection Fourier transformed infrared

AZO: Aluminun-zinc doped

BR: Bacterial reduction

CFU: Colony Forming units

CVD: Chemical Vapor Deposition

DEZ: Diethylzinc

EDS: Energy-Dispersive X-Ray Spectroscopy

EG: Ethyleneglycol

FBR: Fluidized bed reactor

GIXRD: Grazing Incident X-Ray Diffrantion

GL: Glycerol

GPC: Growth per cycle

HD: Hexamethylenediamine

HQ: Hidroquinone

HRTEM: High Resolution Transmission Electron Microscopy

IR: Infrared

LB: Luria Broth

MC: Malonyl Chloride

ML: Molecular layering

MLD: Molecular Layer Deposition

MPI: Multiple Pulse Infiltration

OD: Optical density

PA: Polyamide

PA63: Polyamide 6,3

PBS: Phosphate buffered saline

PET: Polyethylene terephthalate

PVD: Physical vapor deposition

QCM: Quartz Crystal Microbalance

RT: Room Temperature

SEM: Scanning Electron Microscopy

SIS: Sequential Infiltration Synthesis

SVI: Sequential Vapor Infiltration

TEM: Transmission Electron Microscopy

TFEL: thin film electroluminescent

TMA: Trimethylaluminium

TSB: Tryptic Soy Broth

UV: Ultraviolet

VPI: Vapor phase infiltration

XPS: X--ray Photoelectron Spectroscopy

XRD: X-Ray Diffraction

XRR: X-ray reflectivity

Chapter 1 GENERAL INTRODUCTION

1.1 THIN FILM DEPOSITION

Thin films are functional materials whose 3rd dimension shows thicknesses ranging from a few nanometers to about 100 micrometers. By using thin film deposition techniques many properties of bulk materials can be modified, often improved. Examples of these properties include electrical, optical, mechanical or antibacterial properties.[1,2,3] Surface coating is consequently being used for antireflective coatings, energy technologies, optics, sensors, microelectronics, biotechnology-biomedicine and microelectromechanical systems (MEMS). [4,5,6,7,8,9]

Physical and chemical vapor deposition (PVD and CVD, respectively), including sputtering, spin and dip coatings, and spray pyrolysis are common methods for thin film deposition. While physical methods commonly rely on phase transformation (e.g. solid-vapor), CVD typically employs chemical precursor molecules to deposit thin films. The processes rely on a reaction or decomposition of precursors, followed by the condensation of the product on the substrate, thereby growing the film. The precursors are typically supplied as gases, vaporized liquids or sublimed solids.

In this thesis, atomic layer deposition (ALD), molecular layer deposition (MLD), and vapor phase infiltration (VPI), which are variants of CVD, have been used.

1.2 ATOMIC LAYER DEPOSITION (ALD)

The principle of Atomic Layer Deposition (ALD) was independently discovered as "molecular layering" (ML) in the Soviet Union during the 1960s, and as "Atomic Layer Epitaxy" (ALE) in Finland in the 1970s, led by Dr. Tuomo Suntola. The development of the process technology was driven by the need of producing high quality ZnS thin films for thin film electroluminescent (TFEL) flat panel displays. With broadening the process material portfolio and realization that most of the thus created films do not grow epitaxially, the name was changed to Atomic Layer Deposition (ALD), a term that became generally accepted by the end of the twentieth century.[10]

ALD is a chemical gas phase thin film deposition method based on sequential, self-limiting surface reactions. The process, in analogy to chemical vapour deposition (CVD), is based on chemical reactions between two or more precursors, however, in contrast to CVD, where the substrate is simultaneously exposed to all the precursors, in ALD the precursors are temporally

separated. Consequently, in ALD the chemical reaction does not occur in the space above the substrate, but at the solid-gas interface, where the vaporized precursor reacts with the counter precursor previously immobilized on the surface of the substrate. Each precursor dosing is followed by a purging step to remove the excess of the precursor upon saturation and reaction by-products. This assures that a maximum of one monolayer of precursor is bound to the surface in each cycle.

In a typical ALD process (**Figure 1.1**[11]) there are two precursors involved. One of them is the metal source; typically, an organometallic, metal organic or metal halide molecule, while the other one defines the nature of the deposited material (whether it is an oxide, a nitride, a sulfide, etc.). During each half-reaction, one precursor is pulsed into a vacuum chamber with the contained substrate for a given time to allow the precursor to fully react with the substrate surface, this process is self-limiting and leaves up to one monolayer at the surface. The chamber is afterwards purged with an inert carrier gas (typically N_2 or Ar) to remove any excess precursor and the reaction by-products. This is followed by a pulse and purge of the second precursor, creating up to one layer of the desired material. This cycle is then repeated until the desired film thickness is reached.

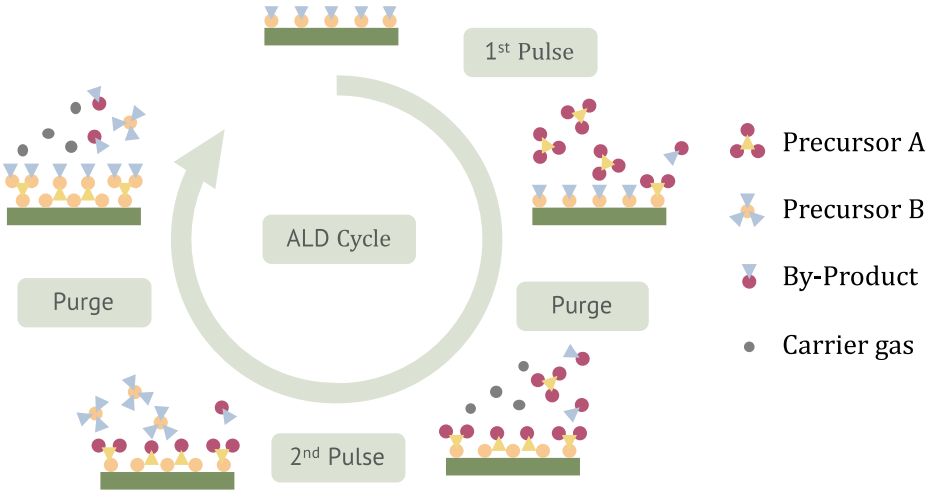

***Figure 1.1**: Scheme of an ALD cycle. Reproduced from Growth of Boron Nitride by Atomic Layer Deposition, Ana Álvarez Yenes, Master's Thesis, 2021. Used with permission.*

The adsorption of the precursor to the surface is predominantly thermally driven. This means that a minimum substrate temperature is required for the ALD process to take place. However, very high temperatures can lead to decomposition of the reactant. The range of temperatures in which a self-saturating process can occur is called the ALD temperature window and it is determined by the precursors involved in the deposition process. Common process temperatures range between 50 and 350°C. The thickness of the deposited film depends on the

number of cycles, and the size of the substrate is only restricted by the reaction chamber. The main limitation of ALD is that it is a slow process, it has growth rates on the order of Å/cycle, but given the increasingly high demand of thin films, this drawback is becoming less significant.[12,13]

1.3 MOLECULAR LAYER DEPOSITION (MLD)

In 1991, Yoshimura and colleagues introduced a process for organic thin films which is analogous to ALD. This process was defined as "Molecular layer deposition (MLD)". Like ALD, MLD is a vapor-phase process controlled by surface interactions where organic monomers are sequentially assembled to oligomeric or polymeric thin film materials.[14]

During a typical MLD process using two homobifunctional precursors (**Figure 1.2**), one precursor reacts with reactive surface functionalities via the corresponding linking chemistry to add a molecular layer to the substrate surface, exposing its own functional groups as new reactive sites. After the chamber is purged to remove any excess precursor and the reaction by-products, the second precursor is supplied and reacts with the reactive sites introduced by the first precursor. Subsequently, another purge step is applied. Repeating the four steps, MLD processes can realize polymeric film growth with accuracy at the molecular level.

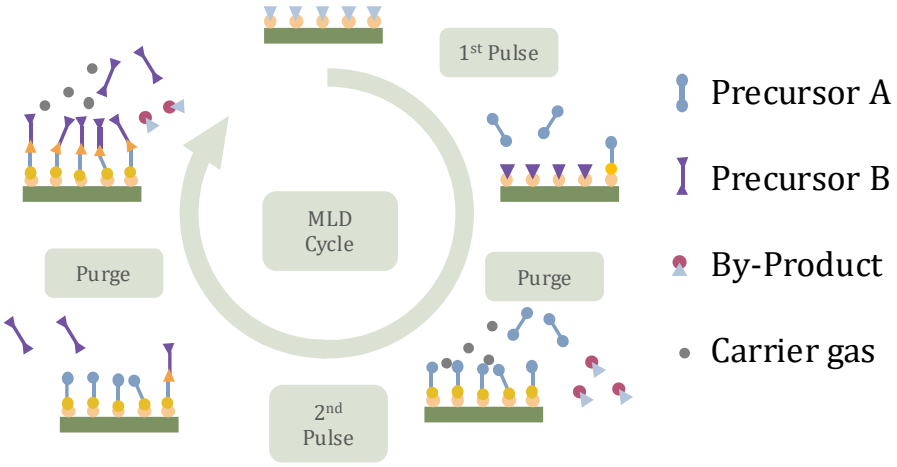

***Figure 1.2**: Scheme of a MLD cycle. Adapted from reference 11.*

MLD has initially been applied to deposit all-organic polymers, like nylon 66 from hexamethylene diamine and adipoyl chloride.[15] In 2008, George's group initiated studies on metal-based hybrid polymers, by combining ALD and MLD precursors, obtaining polymeric metal alkoxide films (i.e., metalcones). In the simplest case, diols were used to replace H_2O in a reaction with trimethylaluminum (TMA). Those materials show many interesting properties.[16]

1.4 VAPOR PHASE INFILTRATION (VPI)

Vapor Phase Infiltration (VPI) is a technique derived from ALD. When the substrate is a soft material, such as a polymer, the precursors will not only bind to the surface, but can also diffuse into the substrate, leading to subsurface growth.[17,18] Initially considered as an undesirable side effect of ALD, this subsurface growth was later found to significantly enhance the properties of certain substrates. In consequence, the process was adapted to optimize the precursors diffusion. An exposure step was introduced between the precursor pulse and purge, providing sufficient time for the precursors to penetrate and effectively infiltrate the material. This method was introduced first by the group of Knez in 2009 under the name multiple pulsed infiltration (MPI).[19] Once the potential of this technique for creating hybrid materials became evident, several research groups developed their own variations with different process parameters and names, including sequential infiltration synthesis (SIS)[20], and sequential vapor infiltration (SVI)[21]. However, as asserted by Leng and Losego, the atomic-scale mechanisms remain identical across all variations, allowing them to be collectively grouped under the more general term, VPI.[22] The depth and density of the inorganic fraction inside the organic substrate can be tuned by controlling some processing parameters, such as the temperature, exposure time, and number of cycles.[23]

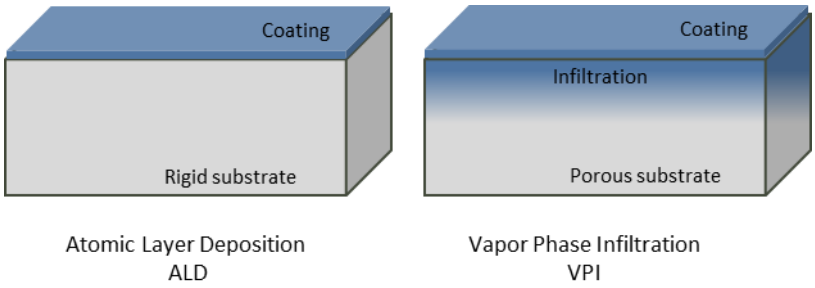

***Figure 1.3**: Comparison of the structures obtained after ALD and VPI.*

During VPI a molecularly porous substrate is subjected to sequential pulses of two or more distinct vaporized precursor molecules. The precursors alternately infiltrate the substrate and undergo chemical reactions. The first precursor typically binds to the functional groups on the surface and in the bulk of the substrate, while the second precursor reacts with the first bound precursor. Even in the case of an inert material, subsurface growth can occur, as the precursor can be physically trapped or physisorbed.[24] An ideal VPI cycle begins with the introduction of the first precursor into the reactor chamber, where it adsorbs onto the substrate surface and diffuses into the matrix. Unlike ALD, VPI incorporates an extended exposure step to allow sufficient time

for the precursor to penetrate the substrate and interact with subsurface reactive sites. Following this, an inert gas is used to purge excess precursor and byproducts from the chamber. A second precursor is then introduced, reacting with the infiltrated material. A final purge removes any unreacted precursor and byproducts, completing the cycle.

1.5 HYBRID MATERIALS SYNTHESIZED BY ALD/MLD

Hybrid materials, combining organic and inorganic components, have existed in nature for billions of years, some examples include bones, mollusc shells, and crustaceans. The organic components offer sustainability, recyclability, and flexible processing, while the inorganic components contribute to thermal stability, mechanical strength, and electrical properties.[25] Hybrid materials exist not only in nature, but there are also manmade hybrids. One of the earliest known examples is Maya Blue, a highly durable pigment used by the ancient Maya in murals, pottery, sculptures, and codices.[26]

The properties of hybrid materials are driven not just by the individual contributions of their components, but also by their synergistic effects. This is the reason why the different hybrid materials were classified into two main families depending on the nature of the interactions between the components. Class I hybrids show trapped or encapsulated materials within a matrix with weak interactions between organic and inorganic moieties, such as Van-der-Waals, hydrogen bonding, or electrostatic interactions. Class II defines hybrid materials in which the organic and inorganic components are linked by covalent or ionocovalent chemical bonds. Hybrid materials often exhibit both types of interactions, but when the influence of strong chemical bonds predominates in determining their properties, they are classified as Class II.[27]

A wide variety of fabrication methods are available in the literature to produce hybrid materials, most of which are solution based including blending, sol-gel methods, emulsion polymerization, photopolymerization and electrochemical synthesis.[28] In 2006, Nilsen et al. patented a process for preparing thin films using a gas-phase deposition technique, specifically for organic-inorganic thin films, preferably utilizing the Atomic Layer Chemical Vapor Deposition (ALCVD) method.[29]

The incorporation of ALD and MLD techniques for synthesizing hybrid materials represents a significant advancement in nanostructure fabrication, utilizing a bottom-up approach. ALD/MLD operates at low temperatures, enabling the incorporation of organic molecules to enhance tunability and facilitate new material discovery. Moreover, it modifies both material and

structure, allowing for surface penetration and the enhancement of soft materials like polymers.[30]

1.6 OBJECTIVE AND STRUCTURE OF THE THESIS

This thesis aims to explore the potential of MLD for the synthesis of organic and multifunctional hybrid organic-inorganic materials.

Chapter 2 overviews the experimental techniques and methods used in this thesis for the chemical and physical characterization of the samples.

In **Chapter 3** the development of purely organic and organic-inorganic hybrid MLD materials is described. A variety of experimental (FTIR, QCM, XPS, XRR…) studies were performed to confirm the film growth and characterize their composition and structure. The antibacterial properties of the obtained nylon and hybrid films were studied by investigating the binding behavior of both Gram-negative and Gram-positive bacteria in vitro. Additionally, the antifungal behavior was investigated using filamentous fungi. The results demonstrate that the developed hybrid metal-organic materials function as versatile antimildew agents. Antimildew tests were conducted under various conditions, and the application of these properties to the seed germination process was explored.

Chapter 4 describes the use of a combined ALD/MLD deposition strategy with $TiCl_4$, H_2O, and various organic precursors (ethylene glycol, glycerol, and hydroquinone) to fabricate hybrid thin films on soda-lime glass substrates. Upon thermal annealing, the organic spacers are removed, yielding porous TiO_2 coatings with anatase-rich composition. These coatings were evaluated for their photocatalytic activity under UV light following ISO 22197-1:2007, using the oxidation of nitric oxide (NO) as a model reaction. The porous structure and crystallinity of the films, confirmed by SEM, TEM, Raman spectroscopy, and XRR, were found to play a key role in their photocatalytic performance, as evidenced by the reduction in NO concentration over multiple testing cycles.

Chapter 5 is involving the engineering of a new reactor design and is devoted to the validation of a new reactor with a flexible and separable chamber volume. Deposition tests were performed in three individual volume fractions, evaluating various deposited materials (Al_2O_3 and ZnO) and process temperatures. A dedicated experiment was carried out to assess the feasibility of operating without a seal between the volumes, thereby simplifying the reactor design.

The work presented in **Chapter 6** details on my collaborative work with Ctechnano Coating Technologies S.L. in an industrial setting as part of this industrial doctoral thesis. My role involved

providing client services, collaborating on various projects, and offering technical support. Due to the proprietary nature of some of the information, certain details in this chapter cannot be disclosed, as they contain confidential intellectual property (IP) owned by the clients. However, we have included all relevant data that can be shared while adhering to confidentiality agreements.

Finally, a summary of the research and future perspectives are given in **Chapter 7**.

Chapter 2 EXPERIMENTAL TECHNIQUES

In this chapter, an overview over the experimental methods employed in this thesis is presented. Details on some specific testing methods, such as for the evaluation of antibacterial and antifungal properties, are described in the relevant sections. The following techniques are described in the order in which they appear throughout the manuscript.

2.1 ATTENUATED TOTAL REFLECTANCE - FOURIER TRANSFORM INFRARED SPECTROSCOPY (ATR-FTIR)

ATR-FTIR is a modification of FTIR which allows infrared spectroscopy (IR) in near-surface areas of a sample.

IR is a non-destructive technique for the qualitative analysis of gaseous, liquid, or solid samples. This technique provides information about the analysed sample through absorption of discrete frequencies of infrared light caused by chemical functional groups. The electromagnetic spectrum in the infrared can be divided into three sections: the far infrared (FIR), which ranges from 400 to 10 cm^{-1}; the mid infrared (MIR), which ranges from 4.000 to 400 cm^{-1}; and the near infrared (NIR), which ranges from 14.000 to 4.000 cm^{-1}. The MIR is the range where fundamental vibrational transitions in organic molecules are induced.[31]

When exposing molecules to an infrared light beam, an absorption of photons causes excitation of molecular bonds to higher vibrational energetic states. The absorption of energy is specific and varies with the nature of the absorbing chemical bonds. The wavelengths that are absorbed by the sample are characteristic of the nature of the chemical bonds and thus of the molecular structure of the sample. As a result of the analysis, a spectrum is obtained, where absorption bands reveal the various types of molecular bonds present in the sample.

In the case of FTIR, the absorption is simultaneously measured at all infrared frequencies. For that, a Michelson interferometer (**Figure 2.1**) is used, that splits the incident light beam into two beams. One of them being reflected by a fixed mirror, and the other by a moving mirror. Finally, the two beams are recombined and, as they have followed different paths, they show interference. As a result, an interferogram is obtained which is a time domain signal and needs to be converted into a frequency domain, by means of a Fourier Transform.

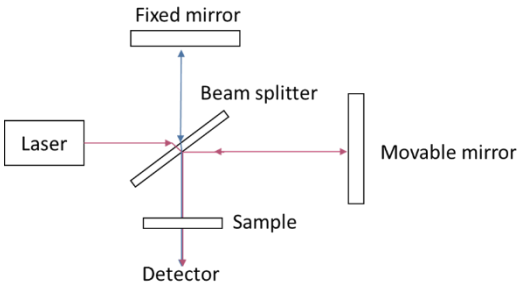

***Figure 2.1**: Diagram of Michelson interferometer.*

The ATR setup is frequently used for near surface characterization of a sample. In ATR, the infrared beam is coupled into a crystal (e.g., zinc selenide), typically with an angle of incidence of 45º, see **Figure 2.2** for a schematic of a cell used in ATR-FTIR spectroscopy. When the beam reaches the interface of crystal and air or the analyte, the difference of the refractive indices of both will cause a reflection of the light. Depending on the angle of incidence, this reflection can be quantitative, with 100% of the light reflected back into the crystal rather than transmitted into the adjacent medium. This is called total internal reflection. In this condition, some small amount of the light energy extends to a short distance (0.1–5 µm) into the surrounding medium beyond the crystal surface. This generates an evanescent wave on the crystal surface. In the IR region of the spectrum, where the sample absorbs energy, the evanescent wave will be attenuated. The attenuated beam is recorded by the detector of the spectrometer and used to generate an FTIR spectrum as it contains spectral information about the sample in vicinity of the crystal surface.[32]

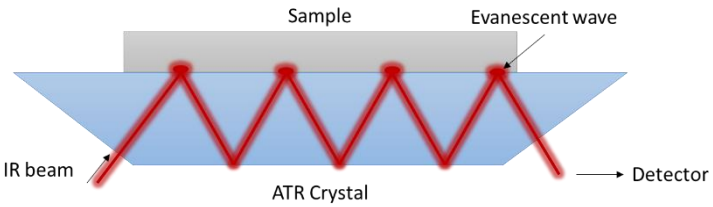

***Figure 2.2**: Schematic of a cell for ATR-FTIR spectroscopy.*

The ATR-FTIR spectroscopy in this thesis was done with a PerkinElmer Frontier spectrometer with an ATR setup.

2.2 X-RAY REFLECTIVITY (XRR)

Electromagnetic waves exhibit reflection when interacting with a sample surface, generating specular, refracted, and diffused reflections. For X-rays, total reflection occurs when the incident angle on a flat material surface is smaller than the total reflection critical angle (θc), and the incident X-rays do not penetrate the material. X-ray reflectivity decreases rapidly with the

incident angle θ increasing above θc. By analysing the X-ray reflection intensity curves from a grazing incident X-ray beam, various characteristics of a thin film, such as thickness, density, and roughness, can be obtained.[33]

As the angle increases, the penetration depth of the beam increases. At each interface with changing electron density, a part of the X-rays is reflected, causing interference, which is seen in form of oscillations in the intensity of the measured reflection.

Figure 2.3 shows schematically the X-ray optics for the cases of incident angles being smaller, equal to, and greater than the critical angle for total reflection, θc.

The XRR measurements in this thesis were carried out with a PANalytical X'Pert Pro diffractometer using a Cu Kα (λ=0,154 nm) X-ray source. The working voltage and current were 45 kV and 40 mA, respectively.

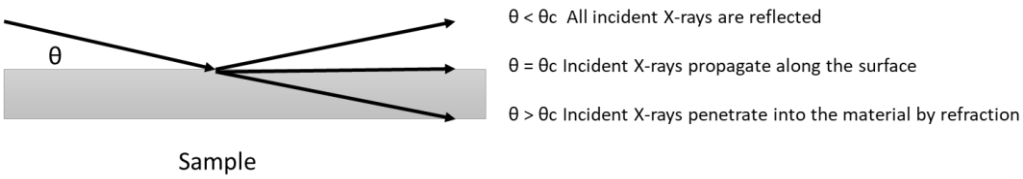

***Figure 2.3**: Reflection and refraction of X-rays at the material surface in dependence of the incident angle.*

2.3 X-RAY DIFFRACTION (XRD) AND GIXRD.

X-Ray diffractometry (XRD) is a non-destructive technique that provides detailed information about the crystallographic structure, chemical composition, and physical properties of a material.

When a beam of X-rays strikes a material, the electron clouds of the atoms cause elastic scattering into various directions. If the wavelength of the X-rays is comparable to the distance between the atoms, interference can occur.[34] The interaction of the incident X-ray beam with the sample produces constructive interference when the conditions satisfy Bragg's law:

$$n\lambda = 2\mathrm{d}\sin\theta,$$

where d is the spacing between the diffracting planes, θ the incident angle of the beam and λ is the wavelength of the beam. [35]

These diffracted X-rays are detected and processed. By scanning the sample over a range of 2θ angles, the spacing between atomic planes (d) can be determined using Bragg's law, allowing the assignment of the crystal structure. The full diffraction pattern, including intensity and phase information, is then used to generate an electron density model of the crystal via Fourier transform. This information helps to determine the sample's composition.

In a variant of the technique, known as Grazing Incidence X-Ray Diffraction (GIXRD), a beam of X-rays is directed onto a sample at a very low angle of incidence, typically less than one degree. This causes the X-rays to interact with only the top few nanometres of the material, resulting in a diffraction pattern that is highly sensitive to the crystallographic properties of the surface region.

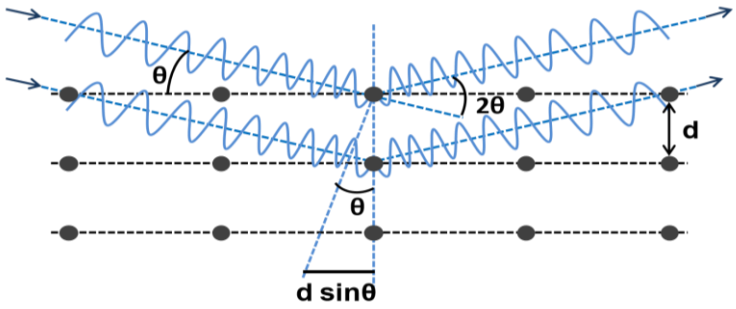

***Figure 2.4**: Schematic of the XRD principle.*

The XRD/GIXRD measurements shown in this thesis were carried out with a PANalytical X'Pert Pro diffractometer using a Cu Kα (λ=0,154 nm) X-ray source. The working voltage and current were 45 kV and 40 mA, respectively.

2.4 X-RAY PHOTOELECTRON SPECTROSCOPY (XPS)

X-ray photoelectron spectroscopy (XPS) is a surface-sensitive analytical technique, in which x-rays impact the surface of a material and eject core electrons from the sample as photoelectrons. The kinetic energy and number of emitted electrons are measured and are characteristic of the chemical composition of the sample, qualitative and quantitative. This is expressed mathematically following the photoelectric effect equation:

$$h\nu = \mathrm{BE} + \mathrm{KE} + \Phi_{spec.}$$

where BE and KE are the binding energy and the kinetic energy of the photoemitted electron, respectively, hν is the energy of the incident photon and Φspec is the work function of the spectrometer. The binding energy of an electron is a material property, independent of the X-

ray source, but influenced by the atom's chemical environment. The peak intensity in XPS is related to the element's concentration, with consideration of its relative sensitivity factor. XPS allows the analysis of an atom's chemical state and environment. [36]

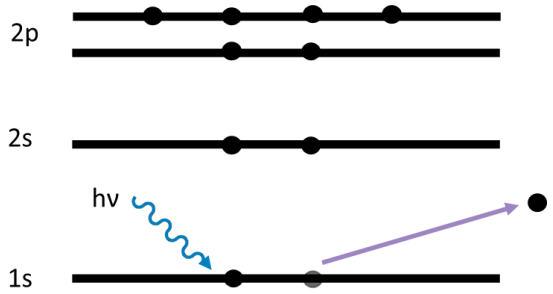

***Figure 2.5**: Schematic of the photoelectron emission process.*

The chemical composition of the hybrid samples in this thesis was studied by XPS with a SPECS instrument equipped with a monochromatic X-rays source (Ephoton=1486.7 eV) and a hemispherical electrostatic energy analyser Phoibos MCD 100. To study the state of chemical elements in the bulk of the hybrid, the surface material was removed by sputtering with a low-energy argon ion beam of 2 keV and a current of 10 μA. The pass energy was 50 eV for all survey scans and was reduced to 10 eV for the high-resolution scans. The measurements were performed by Dr. Iva Šarić Janković and Dr. Robert Peter at the Faculty of Physics, University of Rijeka, Croatia.

2.5 IN-SITU QUARTZ CRYSTAL MICROBALANCE (QCM)

A Quartz Crystal Microbalance (QCM) is a highly sensitive device used to measure small changes in mass by detecting variations in the frequency of a quartz crystal resonator. It operates based on the piezoelectric effect, where mechanical stress on the quartz crystal generates electrical signals. When a small amount of mass (like molecules or particles) accumulates on the surface of the quartz crystal, it changes the resonant frequency of the crystal. By measuring these frequency shifts, the QCM can determine minute mass changes on the order of nanograms per cm^2 through the Sauerbrey equation:

$$\Delta f = -n\frac{2f_0^2}{\upsilon\rho}\Delta m$$

Here, Δf is the change in the resonant frequency of the quartz crystal (Hz), n is the harmonic mode number, f is the resonant frequency of the quartz resonator, Δm is the mass change, υ is the wave velocity (speed of sound) in the quartz plate 3400 m/s and ρ is the quartz density,

being ~2.648 g/cm^3. In most standard QCM measurements, the fundamental frequency (n=1) is used. Using this frequency versus mass dependence allows detecting mass changes up to 10^{-12} kg (pg) (for crystals with frequencies up to 15 MHz), which exceeds the sensitivity limit of any currently used laboratory balance. [37]

The deposition process in this thesis was monitored in-situ with a quartz crystal microbalance (QCM), using an AT cut, 6 MHz resonance frequency, polished, gold-plated, quartz crystal sensor (Phillip Tech.). The QCM crystal was mounted in a bakeable sensor housing (Inficon) and sealed using high-temperature epoxy glue (Epoxy Technology, U.S.A.). The QCM mass resolution was ~0.3 ng/cm^2. The quartz crystal of the QCM was pre-coated with an ALD-grown, 60-80 Å thick Al_2O_3 film prior to any new measurement, to generate identical conditions for all processes.

2.6 ANTIBACTERIAL PROTOCOL

In this thesis, coatings are investigated as means to prevent microbial attachment and proliferation on surfaces. Staphylococcus aureus, strain ATCC 43300, and Escherichia coli, strain ATCC 25922, were used as representative models for Gram-positive and Gram-negative bacteria, respectively.

The testing protocol[38] consisted of the following steps:

1) Bacterial Culture Preparation

A single colony of *S. aureus* or *E. coli* was inoculated into 5 mL of Tryptic Soy Broth (TSB) or Luria Broth (LB), respectively, and incubated at 37°C for 18 hours. The optical density (OD) at 600 nm was measured and adjusted to approximately 5×10^5 colony forming units per mililitre (CFU/mL) using sterile broth.

To establish the relationship between optical density (OD) and bacterial concentration in CFU/mL, an initial OD was randomly chosen and plated onto TSB or LB agar plates. The CFU/mL concentration was determined by colony counting. Using the mathematical relationship between OD and CFU/mL, the required OD for the experiments was calculated. The calculated OD was then verified by plating and colony counting to ensure the accuracy of the relationship.

A concentration of approximately 5×10^5 CFU/mL corresponded to an OD value of ~0.25 for *S. aureus* and ~0.23 for *E. coli*.

2) Surface Inoculation and Incubation

A drop of 400 µL of bacterial suspension was added to each sample of 2x2 cm^2, which was then covered with a 4×4 cm piece of Parafilm and allowed to distribute. Samples were incubated at 37°C overnight.

3) Washing and Bacterial Recovery

After incubation, samples were washed with 5 mL of sterile phosphate buffered saline (PBS) to remove non-adherent bacteria. The samples were then transferred to 50 mL Falcon tubes containing 10 mL PBS and sonicated for 10 minutes to dislodge adherent bacteria.

4) CFU Determination

Serial dilutions of the bacterial suspension were prepared in a 96-well plate, and 3x10 µL drops of each dilution were plated on TSB or LB agar plates in Petri dishes. Plates were incubated at 37°C overnight, and CFUs were counted to calculate the bacterial concentration (CFU/mL) using the formula:

$$\frac{\text{CFU}}{\text{mL}} \text{in the sample} = \text{no. of colonies x dilution factor (DF)} x\ aliquote\ factor\ (AF)$$

2.7 ANTIFUNGAL PROTOCOL

To evaluate a potential antifungal/fungistatic activity of the coatings, two different strategies were employed, using Aspergillus nidulans as a reference model of a saprophytic filamentous fungus. The first strategy involved studying the effect of the coatings on spore germination, while the second focused on their ability to inhibit polar extension of actively growing hyphae. These experiments were designed by Dr. Oier Etxebeste (University of the Basque Country).

The first experiment focused on the coatings' ability to inhibit radial extension of actively growing A. nidulans colonies. Samples of 1x1 cm^2 were placed as indicated in **Figure 2.6a** and asexual spores (conidia) of A. nidulans were point inoculated at the center of Petri dishes filled with Aspergillus minimal culture medium (AMM). After 24 hours incubation at 37 ºC, the fungal growth was visually monitored as hyphae at the periphery of the colony that approached the coatings.

In the second experiment, conidia of Aspergillus nidulans were collected from 72 hours-old cultures, washed twice with tween 20 (0.02%), quantified using a Thoma cell counter and diluted in melted AMM. Before solidification, the spore solution (10^5 conidia) was spread onto AMM plates containing the samples of 1x1 cm^2 (**Figure 2.6b**) and the plates were incubated at 37 °C for 2 days. Germination and growth were monitored visually by observing the expansion of the mycelium over time.

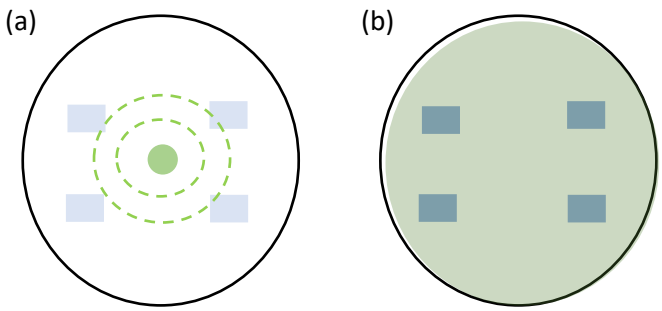

***Figure 2.6**: Schematic representation of the antifungal experiments: (a) study of the ability to inhibit fungal polar extension of actively growing hyphae and (b) study of the effect on spore germination. Blue squares represent the position of the samples in the Petri dish, green circles represent the fungi, and green dashed lines indicate expected hyphal expansion over time.*

2.8 ANTIMILDEW PROTOCOL

To evaluate the antimildew properties of the coatings, experiments were conducted under two distinct environmental conditions to simulate scenarios where mildew formation is likely.

For the first set of samples, 2 mL of water were added directly onto the surface of each sample to create a high-humidity microenvironment. These samples were then sealed to maintain moisture and incubated in the dark at 37°C. For comparison a second set of samples was left open to ambient air without the addition of water. Visual monitoring was conducted periodically in both setups to detect any signs of mildew formation. An original methodology was designed by the authors for the purposes of this work.

2.9 GERMINATION PROTOCOL

To assess the germination process, lentil seeds were placed on the cotton sample inside 55 mm diameter Petri dishes. A volume of 2 mL of water was added to each dish to provide the necessary moisture for the germination. The Petri dishes were then sealed to maintain humidity and prevent water loss.

The samples were kept under ambient environmental conditions, and the germination process was monitored visually. Observations included the emergence and growth rate of seedlings, the appearance of the radicle and cotyledons, and mold formation. Additionally, the timing and conditions under which the seedlings ceased to grow or died were recorded to assess the overall performance of the material in supporting germination. An original methodology was designed by the authors for the purposes of this work.

2.10 PHOTOCATALYTIC ACTIVITY

The photocatalytic activity of the coated glasses was measured in an inert flat-bed photoreactor, designed and manufactured by the company Ariño Duglass according to ISO 22197- 1:2007.[39] Details on the experimental setup, including the gas supply, photoreactor, and analytical system, and test conditions, are provided in **chapter 4**.

2.11 RAMAN SPECTROSCOPY

Raman spectroscopy is a versatile, non-destructive spectroscopic technique that yields detailed information about the chemical structure of an analyte. When a sample is illuminated using monochromatic laser light (visible or near-infrared spectrum), most of the incoming light is scattered without a change in energy—this is termed Rayleigh scattering (elastic scattering). However, a small portion of photons is scattered with a loss or gain of energy caused by molecular vibrations in the analyte, a phenomenon called the Raman effect, or Raman scattering (inelastic scattering). When photons lose energy (shift to a longer wavelength) the phenomenon is called Stokes scattering, while when photons gain energy (shift to a shorter wavelength), it is referred to as anti-Stokes scattering. The energies of these vibrations are specific to the composition and chemical structure of the molecules, which is why Raman is referred to as a chemical fingerprint technique. [40]

Raman spectra often exhibit rich and unique collections of sharp peaks that can be used to determine identity, concentration, phase, morphology, and many other properties of the sample. A Raman spectrum tracks intensity versus wavelength shifts and is commonly recorded between 250 and 4,000 cm^{-1}. In this spectral range, the region between 400 and 1,500 cm^{-1} is called the fingerprint region. Each peak in a Raman spectrum represents a specific molecular bond vibration. While the Raman peak position provides information about the bonds present in a molecule, the Raman spectral intensity is proportional to the concentration.

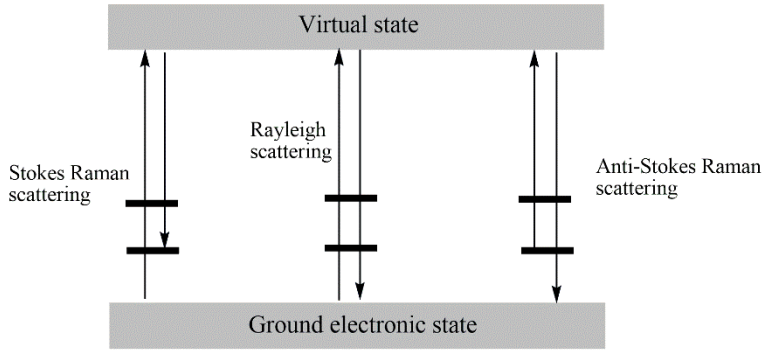

***Figure 2.7**: Schematic energy diagram indicating the various scattering events in Raman spectroscopy.*

2.12 ELECTRON MICROSCOPY

Electron microscopy is a fundamental technique for visualizing and characterizing materials at the molecular, nanoscale, and microscale across various scientific disciplines, including food science. It can provide information about the surface and about bulk features of samples. Unlike light microscopy, electron microscopy techniques utilize accelerated electron beams for illumination. The wavelength of these electron beams, and thus the achievable resolution, is inversely proportional to the accelerating voltage. To maintain image quality, conventional electron microscopes require a vacuum environment, which prevents the electron beam from being scattered by gas molecules. The term "electron microscopy" refers to a group of techniques, with the two primary methods being transmission electron microscopy (TEM) and scanning electron microscopy (SEM).[41]

2.12.1 Scanning Electron Microscopy (SEM)

In SEM, an electron beam scans the specimen surface line by line, across a rectangular cross-section. During the measurement the primary beam electrons (PEs) interact with the specimen surface and are either scattered inelastically as secondary electrons (SEs, **Figure 2.8a**) or elastically as back-scattered electrons, (BSEs, **Figure 2.8b**). The scattered electrons from the surface of the sample contain a variety of information and are therefore collected and analysed. The number of emitted SEs depends on the topography of the sample, while the intensity of the BEs depends on the atomic number Z. Additionally, X-Rays are generated upon exposure of the sample to the PE and can be used to determine the chemical composition of the sample with a technique called Energy Dispersive X-Ray Spectroscopy (EDS).[10]

For the SEM experiments performed in this thesis, a Quanta TM 250 FEG (FEI) SEM was used. The imaging of the samples was carried out using a large field detector (LFD), at 70 Pa and with 10 kV accelerating voltage.

2.12.2 Transmission electron microscopy (TEM)

In the case of TEM, electrons are transmitted through a sample and are detected to generate an image. As the electrons must pass through the sample, only thin samples (less than 100 nanometres thick) can be analysed. The transmission of the electron beam depends on the interaction of the beam with the sample and thus on the atomic number (Z). Low Z permits a transmission of the beam and vice versa, which makes the sample acting like a shadow mask for the electron beam. The interaction of the beam with both high Z and low Z regions eventually generates a contrast in a TEM image. The achievable resolution in TEM is typically higher than in SEM and with a well-adjusted TEM, even crystalline lattices of materials or single atoms can be observed.

The TEM experiments in this thesis were carried out on a FEI Titan 80-300 microscope (Thermo Fisher) by expert operators from the Structural-Morphology Characterization Service of CIC NanoGUNE.

2.12.3 Energy-dispersive X-ray spectroscopy (EDS)

EDS is an analytical technique for the elemental composition of a material. It detects characteristic X-rays emitted when an inner-shell electron is ejected by a PE and replaced by an outer-shell electron. The energy of the emitted X-ray is characteristic of an emitting atom, allowing identification of the elements present in a sample (**Figure 2.8c**). Therefore, EDS allows determination of the elemental composition of a sample.

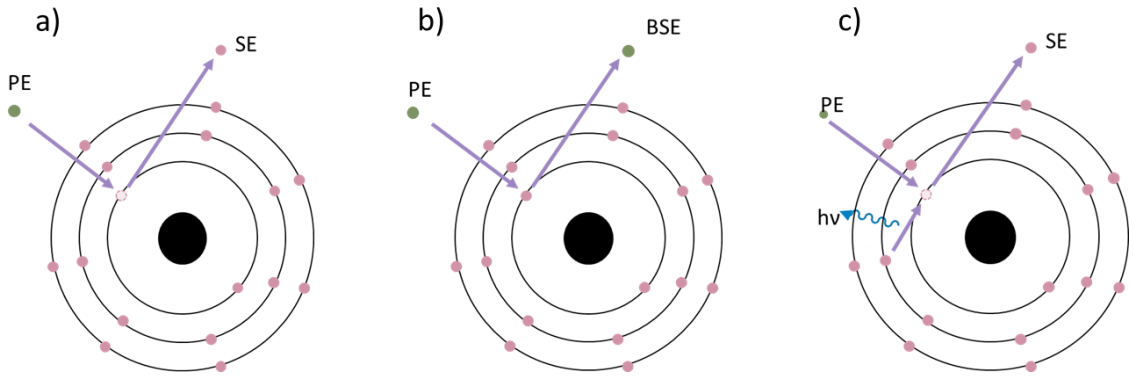

***Figure 2.8**: Schematic representation of the emission mechanisms for (a) secondary electrons, (b) backscattered electrons, and (c) characteristic X-ray radiation from specimen atoms.*

EDS is commonly performed alongside SEM or TEM imaging to correlate the elemental composition with structural or topographical information. In this thesis, elemental mapping was performed to analyse the distribution of elements in the samples, providing insights into their composition and structure.

Chapter 3 HYBRID MATERIALS BY MOLECULAR LAYER DEPOSITION

3.1 INTRODUCTION

3.1.1 Polyamides

Polyamides (PA) are synthetic polymers characterized by their repeating amide bonds. The most common fabrication processes include polycondensation of diamines and diacids (typically provided as acyl dichlorides or anhydrides) or of amino acids, and polyaddition of lactams. The former reaction is most common and led to the discovery of the first polyamide. In 1935, a team of scientists from the chemical company DuPont, led by Wallace Carothers, created polyamide 6,6 using adipic acid and hexamethylenediamine (**Figure 3.1**). The "6,6" designation refers to the number of carbon atoms in the chains of each of the constituting monomers (ISO 16396). DuPont started the industrial production of PA 6,6 under the trade name Nylon®.

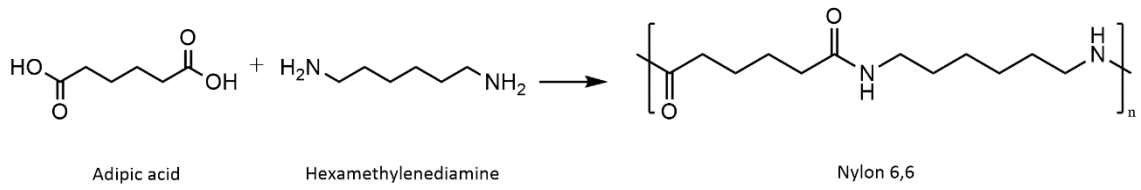

***Figure 3.1**: Synthesis of polyamide 6,6 (Nylon 6,6).*

Polyamides are characterized by great chemical stability and mechanical performance. As the important engineering plastics, polyamides are widely used in the textile industry, oil industry, automotive industry, machinery, marine, electronics, medical devices, domestic appliances, and so on.[42,43,44,45,46]

An important application field of polyamides is food packaging. They are primarily utilized in flexible packaging formats, which extend the shelf life of food by protecting it from external factors such as UV light, oxygen, and moisture, thereby preserving the quality, taste, and aroma of the food. Their excellent permeation barrier properties prevent environmental and food odours from intermingling, which is critical for maintaining the quality of the packaged product.

Polyamides are commonly used in laminate constructions, where they can be employed alone or in combination with other materials, such as polyolefins and foils. They are also a key component in coextruded multi-layer films, often used for vacuum-sealed bags, thermoform-fill-

seal applications, and packaging for perishable items like meat, cheese, and fresh products. The polyamides' ability to withstand high-temperature treatments, such as pasteurization and sterilization, makes them ideal for packaging ready-to-eat meals and processed foods. In addition to their functional properties, polyamides are well-regarded for their mechanical strength, resistance to perforation, and thermal stability, ensuring the safety and durability of packaging during transportation and storage. [47]

Despite the many advantages, polyamides face challenges, such as their tendency to absorb moisture, which can reduce the barrier performance for gases and water vapor. However, these limitations can be mitigated by combining polyamides with other materials or by developing nanocomposites to enhance their properties.[48]

The traditional polyamide synthesis relies heavily on fossil sources, such as aromatic/aliphatic dicarboxylic acids, diamines, amino acids, and lactams.[49] The rapidly increasing consumption of fossil resources and resulting severe environmental issues have triggered negative attention to petroleum-based polymers. Consequently, the development of sustainable polymers from biomass-based feedstocks has become a hot topic in both academia and industry.

MLD allows for the deposition of ultra-thin molecular layers atop environmentally friendly materials, enabling considerable reduction of polyamide use. With MLD it is also possible to upgrade the polyamide by merging with other materials in a more controlled and efficient way than with traditional methods.

3.1.2 Hybrid materials with titanium or zinc.

Hybrid materials that incorporate oxides of titanium or zinc combine the properties of these ceramics with other matrix materials, often polymers, to create advanced, multifunctional materials. Those can be very valuable for a variety of different applications, including optics, electronics, and medicine.[50] Today, several MLD processes have already been developed for a variety of hybrid materials, called 'metalcones', by combining known metal–organic ALD precursors with suitable organic monomers. **Figure 3.2** schematically shows titanicones grown with $TiCl_4$ and ethylene glycol (EG) or glycerol (GL).[51]

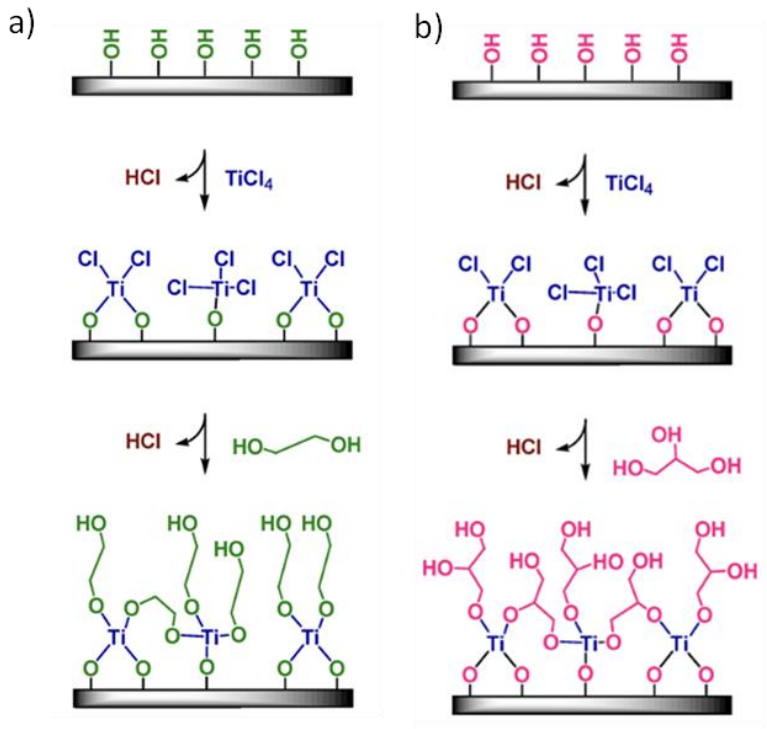

***Figure 3.2**: Schematic representation of titanicone MLD formed by $TiCl_4$ and EG (a) or GL (b).*

An example of zinc-organic hybrid layers is shown in **Figure 3.3**. Such layers can be formed with a three-step MLD sequence with diethylzinc (DEZ), ethanolamine (EA), and maleic anhydride (MA). [52]

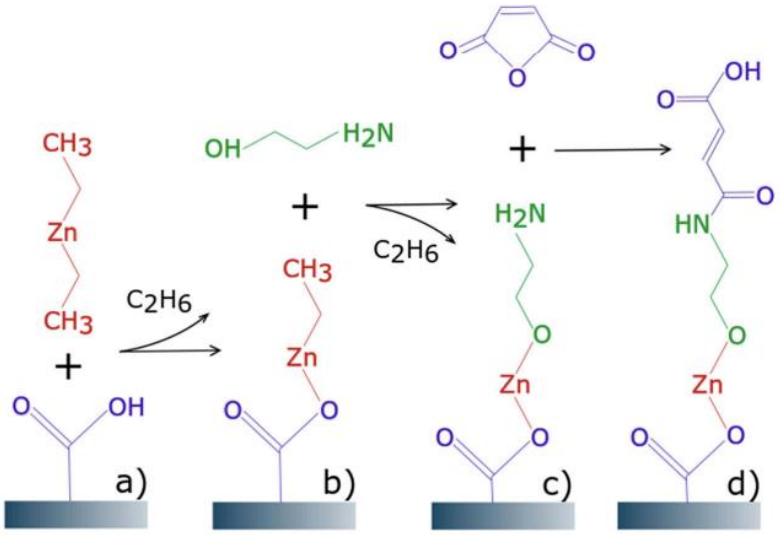

***Figure 3.3**: MLD reaction scheme: (a) Diethyl zinc (DEZ) reacting with surface hydroxyl group coming from the previous cycle, releasing C_2H_6 as byproduct; (b) ethanolamine (EA) reacting with surface-bound ethyl-zinc, releasing another C_2H_6 as byproduct; (c) maleic anhydride (MA) ring-opening reaction and binding to the surface-bound amine; (d) monolayer formed after one MLD cycle, restoring the surface functionality for the next cycle.*

3.1.3 Antibacterial, antifungal and antimildew properties

In daily life, contact with various bacteria, fungi, and other microorganisms, is inevitable. These microorganisms can grow and multiply under the right environmental conditions, spreading diseases upon contact and posing health risks. With the COVID-19 pandemic, the society became more concerned about safety and hygiene, leading to a significant increase in interest and demand for antibacterial and antiviral nanocoatings.[53,54] Such coatings play a role in a multiplicity of applications, including food packaging, which we address here.

Spoilage from yeast and mold leads to significant economic losses in the food industry and is also harmful to consumer health.[55] To combat this, traditionally, antibacterial agents were mixed directly into food formulations as preservatives.[35] However, the use of those is controversial due to potential health concerns, taste alteration, and limited effectiveness caused by interactions with food components, dilution, or evaporation. Furthermore, excessive fungicide use in agriculture has promoted resistant pathogens, requiring higher doses and increasing toxic residues in food. To address these challenges, incorporating antibacterials and antifungals into the packaging, rather than the food itself, can help preventing growth of those pathogens on food surfaces, potentially reducing the need for large quantities of antibacterial agents and extending the lifetime of the antibacterial activity throughout storage, transport, and use.[56,57]

Developments in materials research have led to a broad range of compounds that have potential for serving as antibacterial coatings. Among the various coating techniques, ALD stands out as it enables the synthesis of high-purity inorganic nanocoatings, covalently bound even to surfaces of complex shape and topography, with precise control over thickness and composition.[58]

ALD-based coatings have demonstrated effective antibacterial properties against common pathogens, including *Staphylococcus aureus* and *Escherichia coli*, while maintaining biocompatibility with human cells.[59]

Organic nanocoatings grown by MLD offer greater flexibility and adaptability than inorganic nanocoatings. MLD facilitates the incorporation of specific functional groups into the coating structure, which can enhance interactions with microorganisms and increase antibacterial efficacy.[60] Additionally, polymers are usually lighter than inorganic materials and, in many cases, more cost-effective to produce, which demarks further benefits for the use of such materials.

By combining ALD and MLD, hybrid materials can be created, which can display the properties of both components and additionally synergistic effects may occur.

In this thesis, polyamide 6,3 was grown from malonyl chloride (MC) and 1,6-hexanediamine (HD) by MLD. The hybrid materials were grown using diethyl zinc and titanium tetrachloride as metal containing sources and malonyl chloride and hexamethylene diamine as sources of the organic component.

Staphylococcus aureus and *Escherichia coli,* two of the most commonly used bacteria for studying antibacterial effects, were chosen as model organisms to evaluate the antibacterial activity of the coatings against Gram-positive (GRAM+) and Gram-negative(GRAM-) bacteria.

Aspergillus nidulans is a saprophytic filamentous fungus that is found virtually everywhere. It grows on various substrates, especially in soils and decomposing materials (such as plant matter, construction materials, etc.). It is thermotolerant, able to survive between 12°C and 57°C. For this reason, *Aspergillus nidulans* was selected as the exemplary fungus for our antifungal experiments.[61]

3.1.4 Coating on seeds for germination control

High temperatures, prolonged droughts, and unpredictable rainfall variations, due to climate change, have a negative impact on the seed germination. The use of natural polymers in agriculture, especially in seed coating, is a growing trend.[62] Seed coating can influence the microenvironment of each seed, enhancing seed quality and health by protecting it against various soil, air and seed borne diseases. Additionally, this technology can help preventing mold formation.

An alternative to seed coating is the application of ALD/MLD directly to the substrate where the seeds will be placed for germination.

3.2 EXPERIMENTAL SECTION

3.2.1 Deposition processes

The experiments for the deposition of nylon 6,3 (PA63) were performed in a commercial ALD reactor (Savannah S100, Cambridge NanoTech Inc). Two precursors, malonyl chloride (MC) and 1,6-hexanediamine (HD), both purchased from Sigma-Aldrich, were used to grow nylon 6,3 by MLD. According to the literature, deposition of PA63 by MLD has not been previously described.

MC is liquid and HD is solid at room temperature. During the deposition HD was heated at 42°C. The reactor was evacuated together with a concurrent N_2 gas purge at a flow rate of 10 sccm (10^{-2} mbar). Nylon 6,3 MLD was grown at reactor temperatures of 60, 70, 80, 90, 100 and 120°C.

Organic-inorganic hybrids were deposited using two reactors: the Savannah S100 for hexamethylenediamine-based hybrids, and the Play Series tool from Coating Technologies S.L. for malonyl chloride-based hybrids. Diethylzinc (DEZ) and titanium tetrachloride ($TiCl_4$) were used as inorganic precursors. The organic-inorganic hybrid materials were deposited at temperatures of 120°C (using $TiCl_4$) and 100°C (using DEZ). The lower temperature for DEZ was necessary because temperatures above 100 °C cause it to stain the denim fabric.

3.2.2 Characterization

The thickness and crystallographic features of the deposited films were measured by XRR and XRD, respectively, using a PANalytical X'Pert Pro diffractometer with a Cu Kα (λ=0,154 nm) X-ray source. ATR-FTIR was measured with a PerkinElmer Frontier spectrometer at room temperature. The chemical composition and bonding state of the films were examined by XPS using a SPECS instrument equipped with a hemispherical electron analyser and a monochromatized source of Al Kλ x-rays. The calibration of the energy scale in all XPS spectra was done by placing the binding energy of characteristic C 1s peak at 284.5 eV. The XPS spectra were deconvoluted into several sets of mixed Gaussian-Lorentzian (G-L) functions with Shirley background subtraction. Si (100) was used as substrate for the XPS analyses.

3.2.3 Antibacterial properties

The bacteriostatic activity of the samples was evaluated against the bacterial strains Staphylococcus aureus (S. aureus, ATCC 35556) and Escherichia coli (E. coli, ATCC 25922), the most common model organisms for gram-positive (GRAM+) and gram-negative (GRAM-) bacteria, respectively.

The attachment and proliferation of Gram-positive and Gram-negative bacteria on the polyamide 6,3 and hybrid material surface were evaluated for jeans, PET, cotton and carton following the protocol described in **chapter 2** and and using the corresponding untreated substrates as positive control.

In a typical experiment, the bacterial culture was diluted to a level which contains approximately 5×10^5 colony-forming units (CFUs) per millilitre (CFU/ml). Samples ($2x2cm^2$) were inoculated with 400 µl of the bacterial suspension and incubated at 37°C overnight.

After incubation, the samples were washed with phosphate-buffered saline (PBS) to remove non-adherent bacteria and then sonicated for 10 min in PBS to release the bacteria that remained attached. This solution is serially diluted, plated and incubated at 37°C overnight to obtain the

number of viable bacteria attached to the sample. The number of viable bacteria in the sample (CFU/mL) was determined by the Standard Plate count method.

$$\frac{\text{CFU}}{\text{mL}} \text{in the sample} = \text{no. of colonies x dilution factor (DF)} x\ aliquote\ factor\ (AF)$$

The "bacterial reduction (BR) percentage" is a measure of the effectiveness of an antibacterial treatment or material in reducing bacterial population. It is typically calculated using the following formula:

$$Bacterial\ Reduction\ percentage = \left(\frac{Initial\ CFU - Final\ CFU}{Initial\ CFU}\right) x\ 100$$

For a material to be considered antibacterial, it must present a minimum %BR value of 99%, according to ISO 22196.[63]

3.2.4 Antifungal properties

The effect of the coatings on spore germination, and their ability to inhibit polar extension of actively growing hyphae, were studied. The protocol is described in **chapter 2**. PA63 and MC-Zn hybrids, deposited on jeans, PET, carton, and cotton, were tested. Quantification of the growth was performed, analyzing changes in fungal growth and hyphal extension, compared to the untreated control samples. No reports on the antifungal activity of PA63 or hybrids materials with zinc were found in literature. In contrast, ZnO nanoparticles have been introduced as promising antifungal agents.[64]

3.2.5 Antimildew properties

The prevention of mold growth was studied without external addition of fungi. The protocol is described in **chapter 2**. PA63 and MC-Zn hybrids, deposited on jeans, carton, cotton, and birch wood, were tested. The evaluation was visual, monitoring the presence or absence of mold on the surface over time. No reports on the antimildew activity of PA63 or hybrids materials with zinc were found in literature.

3.2.6 Effect of the antifungal and antimildew properties on seed germination

Lentil seeds were planted on cotton substrates, untreated and coated with PA63 and MC-Zn hybrids. The protocol is described in **chapter 2**. The samples were then placed in Petri dishes containing the respective substrates under varying conditions. This methodology aimed to assess

the impact of the PA63 and hybrid coatings on the germination process, focusing on growth patterns, mold development, and overall seed health in comparison to untreated substrates.

3.3 RESULTS

3.3.1 Deposition of polyamide 6,3 by MLD

The proposed surface reactions for nylon 6,3 are as follows:

$$(A)\ -NH2\ *+ClCOCH2\ COCl \rightarrow -NHCOCH2\ COCl*(A)\ -NH_2{}^* + ClCOCH_2\ COCl\ \rightarrow$$
$$-NHCOCH_2\ COCl^* + HCl\ (1)$$

$$(B)\ -NHCOCH_2\ COCl^* +\ H_2\ N(CH_2)_6NH_2$$
$$\rightarrow\ -NHCOCH_2\ CO - NH(CH_2)_6NH_2{}^* + HCl\ (2)$$

Here the asterisks indicate the surface species. In the reaction "A", the MC reacts with the surface-bound amine (-NH_2) species and terminates the surface with -COCl*. When HD is subsequently supplied in reaction "B", it reacts with the terminal -COCl species and restores the -NH_2*-terminated surface. As a result of an ABAB sequence, a nylon 6,3 film is grown. Note that the initial reaction occurs on the initial surface functional groups, which are defined by the substrate and might be hydroxyls, amines, etc.

Figure 3.4 shows the saturation curves for the MLD nylon 6,3 process at 90°C after 50 MLD cycles. The saturation GPC (Growth Per Cycle) is achieved with pulsing times of 0.03 seconds for MC and 5 seconds for HD. This phenomenon indicates that the GPC no longer increases with longer precursor pulse times, signifying a complete surface reaction.

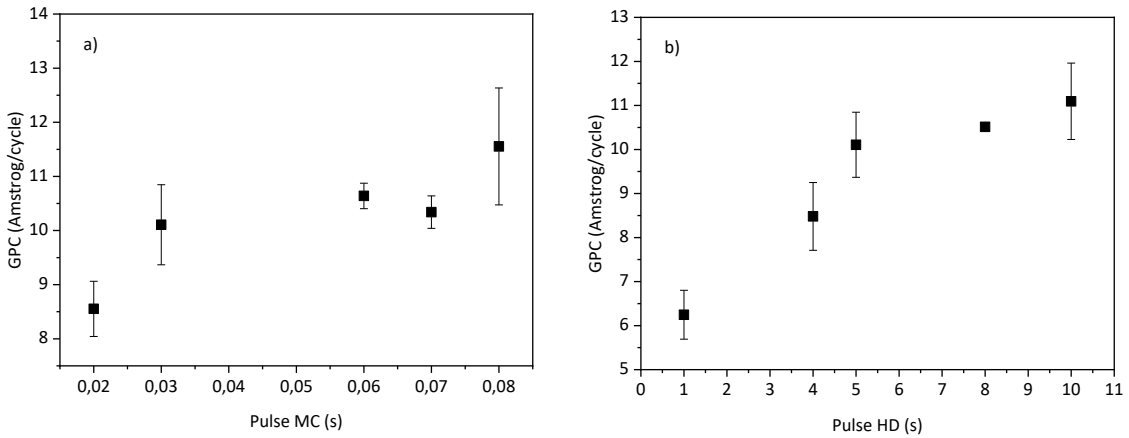

***Figure 3.4**: Saturation curves for the nylon 6,3 MLD process using MC and HD as precursors at 90°C and 50 MLD cycles. The pulse durations of MC (a) or HD (b) were respectively varied, while the pulse time of the counter precursor was kept constant.*

Figure 3.5 shows the thicknesses of the nylon 6,3 films grown on silicon (100) wafers, determined by XRR, as a function of the number of MLD cycles at processing temperatures of 60, 70, 80, 90, 100 and 120°C. The thicknesses of the films increase linearly with the number of cycles, indicating that each MLD cycle contributes a consistent and uniform amount of material to the film. This growth behaviour is observed from other polyamides deposited using MLD.[15, 65]

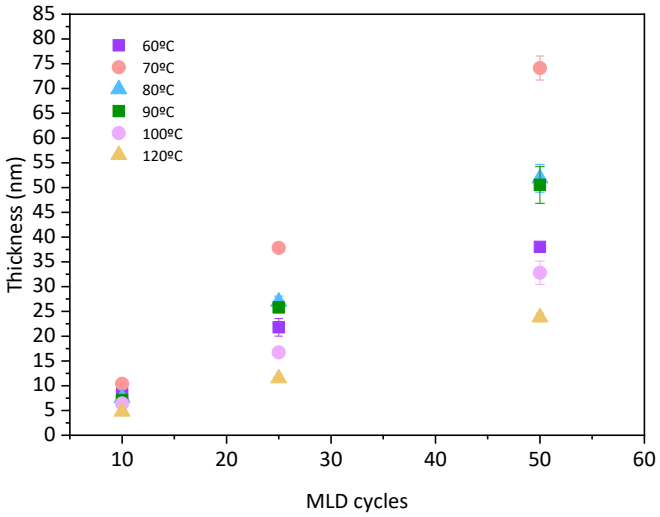

***Figure 3.5**: Nylon 6,3 film thickness vs. number of MLD cycles, grown on silicon (100) substrates at various processing temperatures. The thicknesses were obtained from XRR measurements.*

In **Figure 3.6**, the dependence of the GPC on the number of cycles is shown for the different deposition temperatures. The initial GPC is lower and increases with the increment of cycle numbers. This is a common observation in ALD and MLD processes, where the surface coverage at the initiation of growth is incomplete and requires several cycles to form a complete layer. Once the substrate surface is fully covered, this effect becomes less appreciable and linear MLD growth can be observed.[66]

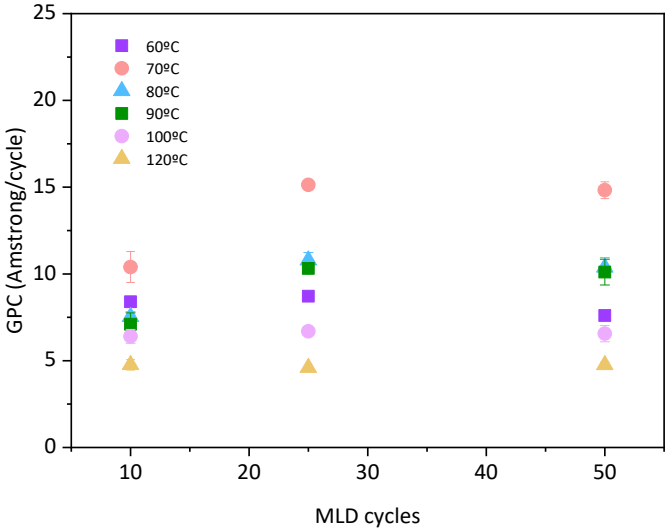

***Figure 3.6**: Nylon 6,3 GPC vs. the number of MLD cycles, grown on silicon (100) substrates at various processing temperatures.*

Figure 3.7 shows the temperature-dependence of the GPC. It increases with increasing temperature up to 70°C and afterwards decreases upon further temperature increments. Temperature-dependent GPCs have also been observed in MLD processes of other polyamides. One possible explanation, as suggested for similar polyamide systems such as Nylon 2,6, is the occurrence of double reactions, where precursors react at both reactive sites simultaneously, reducing the number of available functional groups for subsequent cycles.[15,65, 67]

Since there are no specific data for nylon 6,3, an estimation of its chain length is made based on the values provided for comparable polyamides. For nylon 2,6, Myers and George report an expected length of 13 Å and for nylon 4,6, Bermudez et al. stated a chain-period length of 14.7 Å, corresponding to a fully extended conformation. Therefore, for nylon 6,3, an intermediate can be assumed, likely closer to 14 Å.[13,15] At 70 °C, a GPC of ∼15 Å was determined by XRR. Given the closeness to the theoretically expected value, it is plausible to conclude that the chain growth on the substrate is perpendicular to the surface orientation. The slightly higher GPC than expected may further indicate some contribution from parasitic CVD-type of polymer growth.

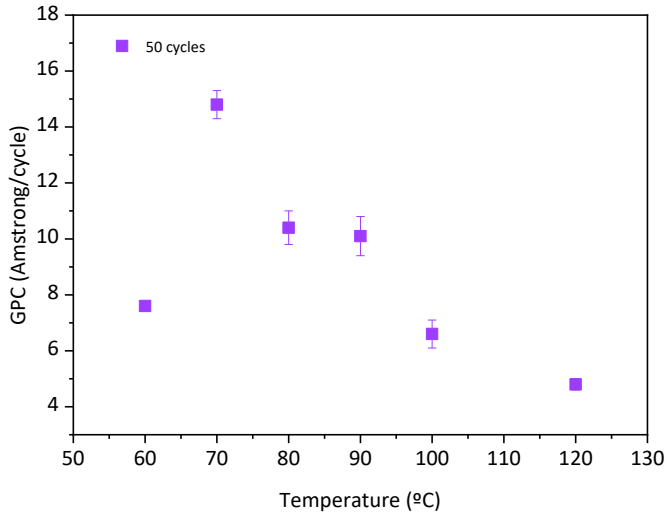

***Figure 3.7**: Temperature-dependence of the GPC for the MLD-growth of nylon 6,3.*

To understand the growth process, we performed in-situ quartz crystal microbalance (QCM) studies of the film growth at 100°C. The QCM results, showing the mass gain versus time, are displayed in **Figure 3.8**. The pulse-purge timing sequence for the process was 0.3s/35s/1s/35s for MC/N_2/HD/N_2, respectively. The in-situ QCM monitoring showed a reproducible and linear increase of the mass with increasing cycle number. The MC dosing led to a mass gain of 18 ng/cm^2, and the HD dosing to 10 ng/cm^2.

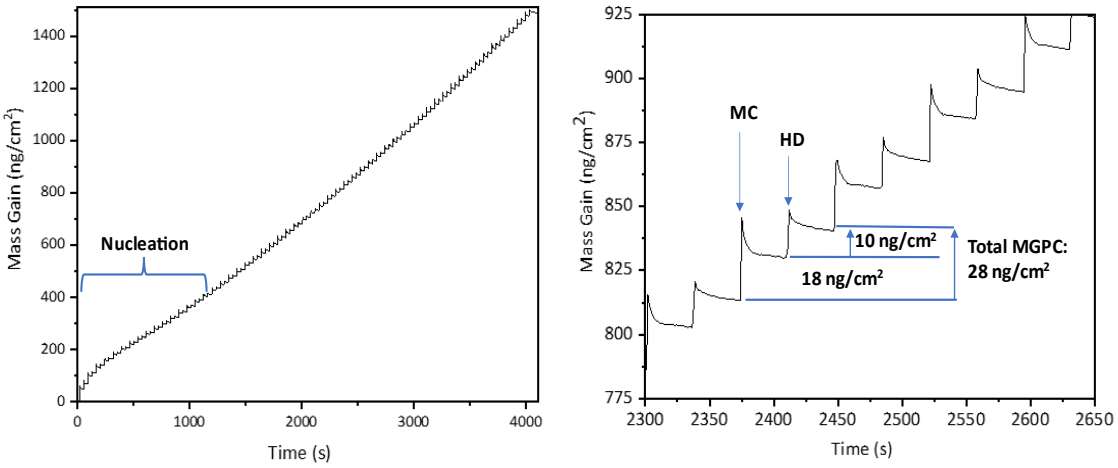

***Figure 3.8**: QCM measurements of the mass gain vs. time for the nylon 6,3 MLD process on an Al_2O_3 ALD pre-deposited surface at 100°C. The growth was monitored over 55 reaction cycles using a pulse-purge timing sequence of 0.3s/35s/1s/35s MC/N_2/HD/N_2, respectively. The graph on the right presents a magnified view of the selected region from the full dataset shown on the left.*

Figure 3.9 compares the ATR-FTIR spectra of MC, HD, and nylon 6,3, grown at 80°C on pellets of pressed ZrO_2 powder. The pellets were chosen as substrates because of their high surface area and consequently higher volume fraction of the nylon film, which eases the detection by ATR-FTIR. The film shows characteristic amide peaks at 3267 cm^{-1} (N-H stretching vibration), 1640 cm^{-1} (C=O stretching vibration), and 1535 cm^{-1} (and C-N stretching vibration). The spectra do not show peaks of residual precursors, indicating successful chemical reaction and sufficient purge time.

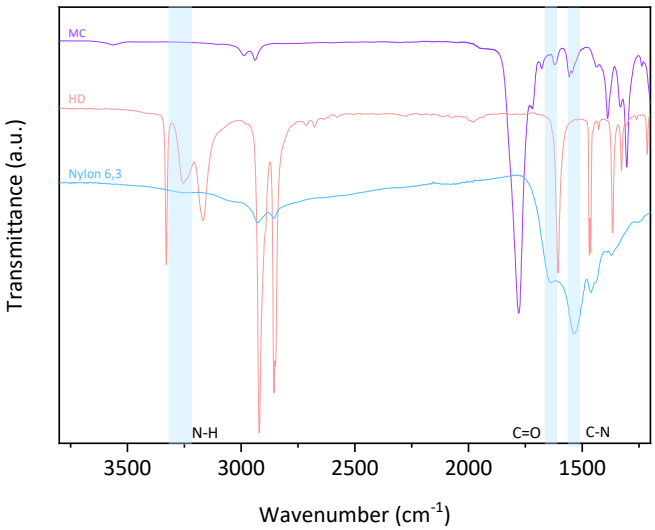

***Figure 3.9**: ATR-FTIR spectra of MC (purple), HD (red) and nylon 6,3 (blue), grown at 80ºC on ZrO_2 pellets.*

The XPS survey spectrum of the sample **(Figure 3.10a**) shows presence of carbon, nitrogen and oxygen atoms in nylon 6,3. The deconvoluted C 1s XPS spectrum (**Figure 3.10b**) shows involvement of several carbon species in the signal, including C-C, C-N, C=O and C-O. The N 1s XPS spectrum (**Figure 3.10c**) shows contributions of C-N and N-O. The O 1s XPS spectrum **Figure 3.10d**) shows presence of C=O and C-O species. The signals corresponding to C-O and N-O are likely to stem from surface contamination. More importantly, there is no peak corresponding to Cl 2p, indicating quantitative precursor conversion in the developing film. The measured composition of the sample is 11.0 at. % nitrogen, 19.3 at. % oxygen and 67.6 at. % carbon, which align well with the expected composition of nylon 6,3. There may be some uncertainty due to a likely contribution of carbon from air exposure.

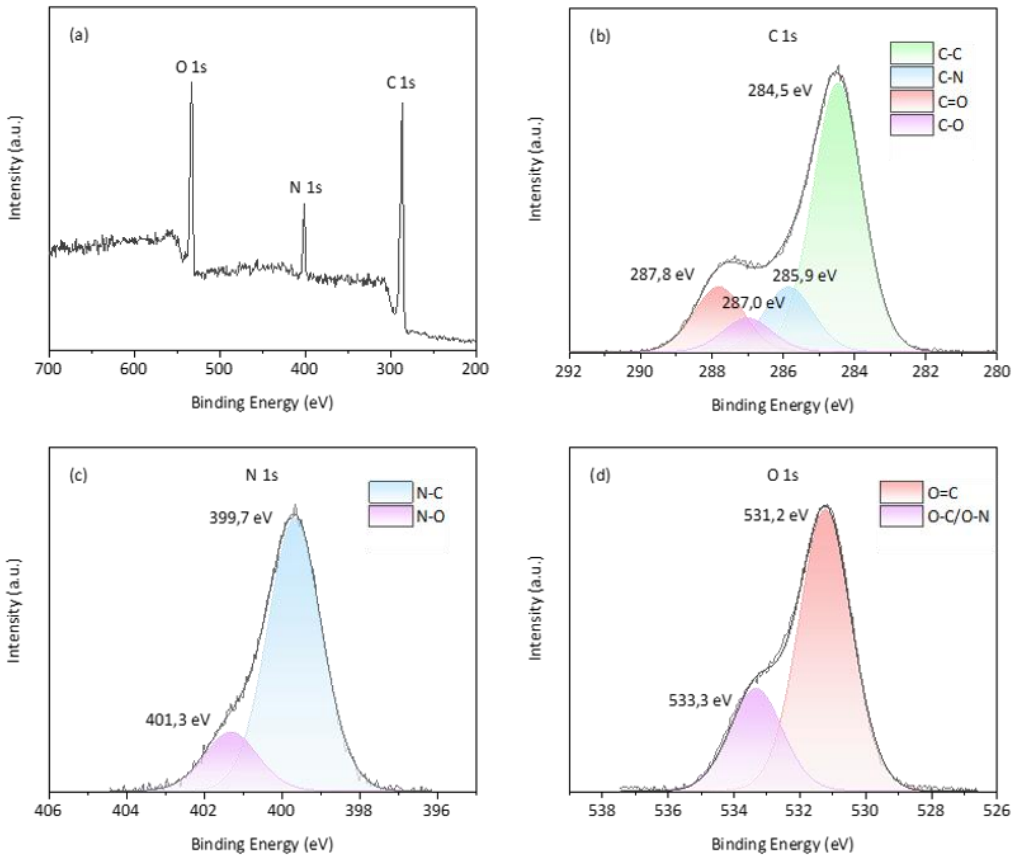

***Figure 3.10**: (a) XPS survey spectrum of a nylon 6,3 film grown on Si (100) and (b) high-resolution spectra of C 1s, (c) N 1s, and (d) O 1s.*

The chemical stability of the nylon 6,3 films was tested by exposing the films to solutions at various pH values (**Figure 3.11**) to assess their properties as a chemical and protective barrier for food and agricultural products, which are their main applications in this thesis. The coated wafers were immersed into a strong base (KOH) and a strong acid (HCl) at different concentrations,

followed by rinsing with deionized water. The changes in the film thickness were measured by XRR.

The film was not dissolved even after 4 days in 10^{-4} M KOH solution (pH=10). However, the film was completely removed within 2 hours in a 0.01M KOH solution (pH=12), which can be derived from the changes in film thicknesses. No film thickness change was observed after more than 5 days in either 0.01 M (pH=2) or 10^{-4} M (pH=4) HCl solutions, confirming a great chemical stability of the films.

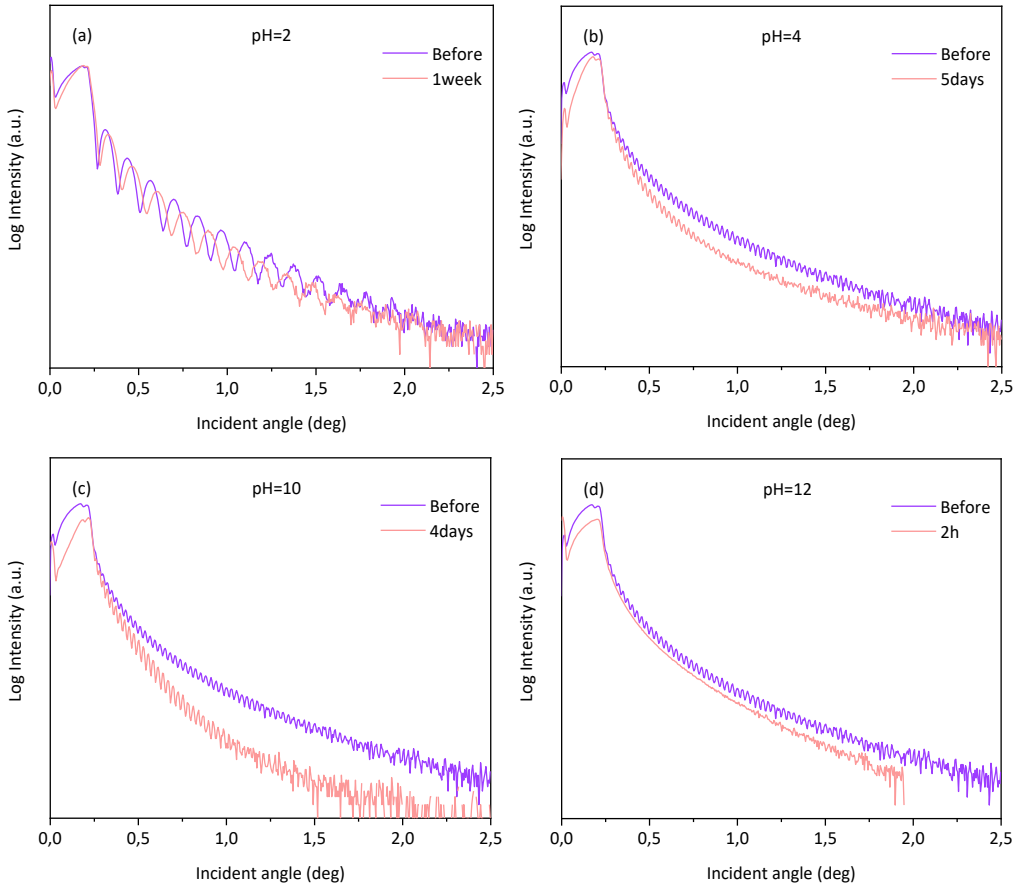

***Figure 3.11**: XRR measurements of nylon 6,3 films, deposited on Si wafers, upon immersion into solutions with (a) pH=2, (b) pH=4, (c) pH=10, and (d) pH=12.*

3.3.2 Organic-inorganic hybrid materials deposited by ALD/MLD

By combining $TiCl_4$ or DEZ as inorganic precursors with malonyl chloride (MC) or hexamethylenediamine (HD) as organic precursors, four different hybrid materials were designed.

Hybrids with malonyl chloride (MC) were analyzed, and the XPS spectra of the MC–Zn hybrid are presented in **Figure 3.12**. The MC-Zn hybrid shows a C-O bond and Zn-O, which is coherent with the presence of C-O-Zn in the film. Also, Cl peaks are observed, likely due to residual malonyl chloride.

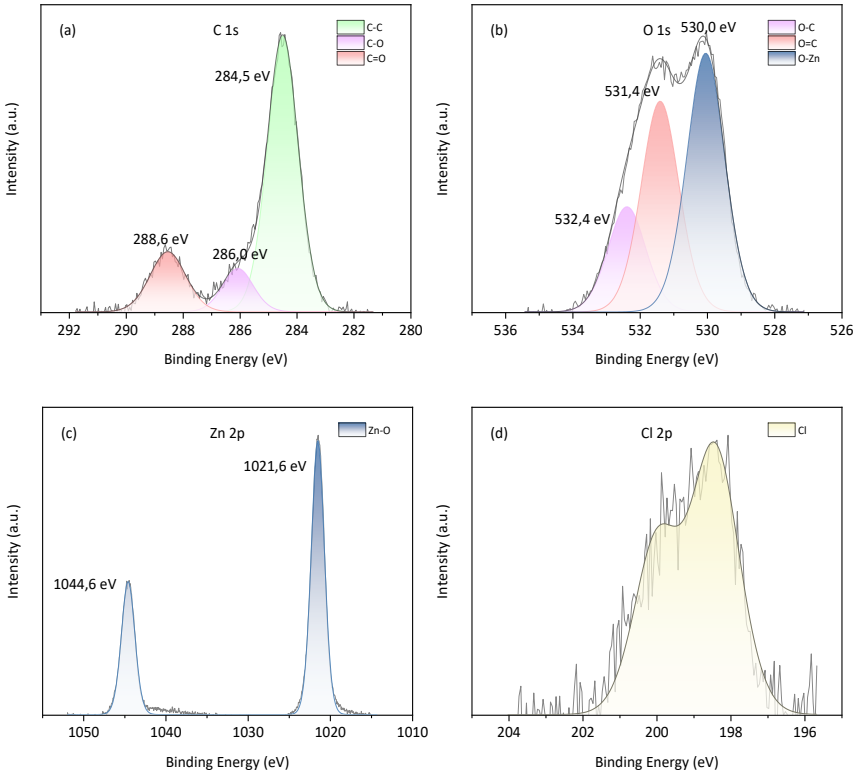

***Figure 3.12**: High-resolution XPS spectra of (a) C 1s, (b) O 1s, (c) Zn 2p, and (d) Cl 2p of the MC-Zn hybrid.*

For further confirmation, XRD measurements were performed. In Figure 3.13, a comparison of the cotton reference (purple) with ZnO-coated (coral) and MC-Zn-coated (blue) cotton is made. No ZnO peaks were detected.

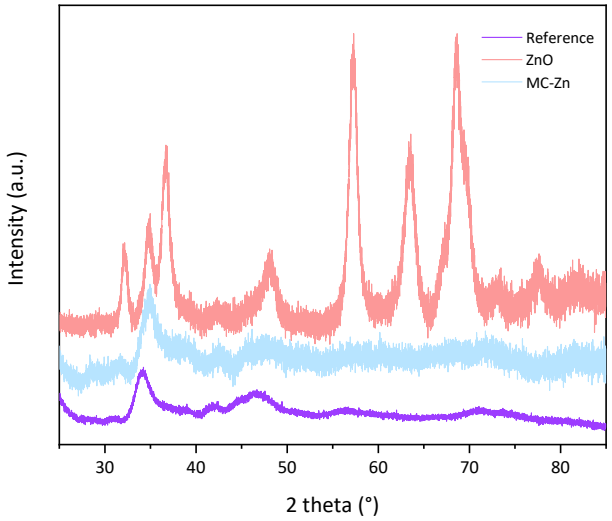

***Figure 3.13**: XRD patterns of cotton reference (purple), ZnO-coated (coral) and MC-Zn-coated (blue) cotton.*

The XPS spectra of MC-Ti (**Figure 3.14**) show the presence of carbon, oxygen and titanium. Based on the strong Ti-O signals, a predominant formation of titanium oxide can be assumed. The presence of C=O bonds without C-Ti and C-O bonding implies that the MC did not effectively react with titanium.

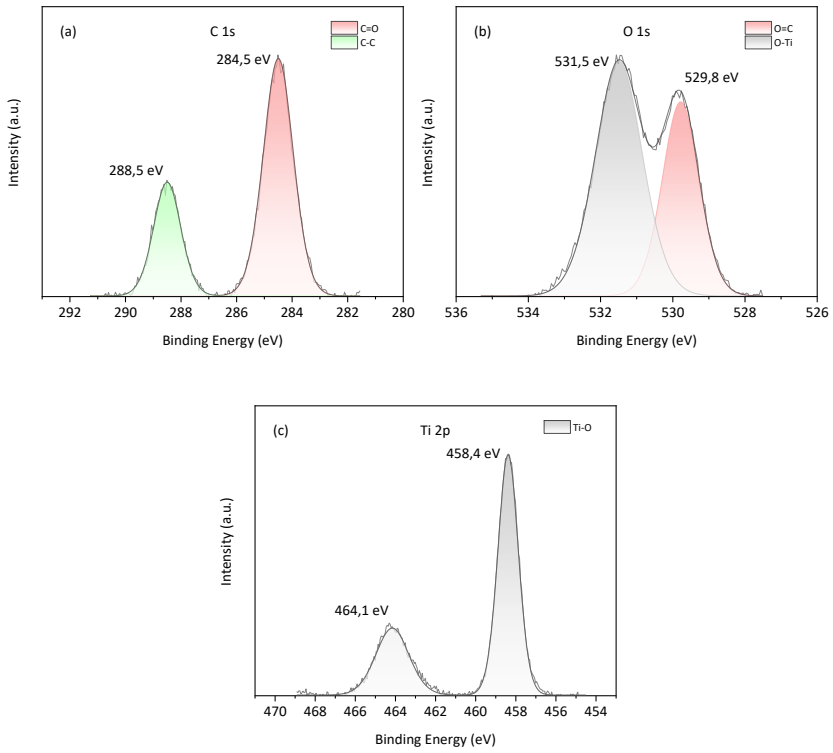

***Figure 3.14**: High-resolution spectra of (a) C 1s (a), (b) O 1s, and (c) Ti 2p of the MC-Ti hybrid.*

Hybrid materials with HD as the organic component should not exhibit oxygen bonds, given the lack of oxygen in the involved precursors. However, the XPS spectra in **Figure 3.15a,b** show that both Zn and Ti-based hybrid materials contain M-O bonds. To eliminate the possibility of surface contamination, both samples were etched with 1 keV argon ions for 10 minutes in vacuum prior to the XPS analysis. This procedure removes the top surface layer and allow analysis of the subsurface of the grown film. Despite this treatment, the films still exhibited M-O bonds and contained less than 4% nitrogen. Furthermore, both titanium and zinc are only bound to oxygen as can be seen from **Figure 3.15c,d**. The presence of Cl in the spectra indicates presence of remaining malonyl chloride, which could react with the inorganic precursors more easily than HD, thereby suppressing the formation of the M-HD hybrid. Therefore, we can conclude that no hybrids with HD were formed, as the metals reacted with oxygen from impurities instead. The formation of Ti–N and Zn–N bonds likely requires considerable energy—especially for Ti–N, indicating that the deposited film may exist as a metastable intermediate. Once exposed to

atmospheric moisture after removal from the reactor, it may undergo further transformation into TiO_2 or ZnO.

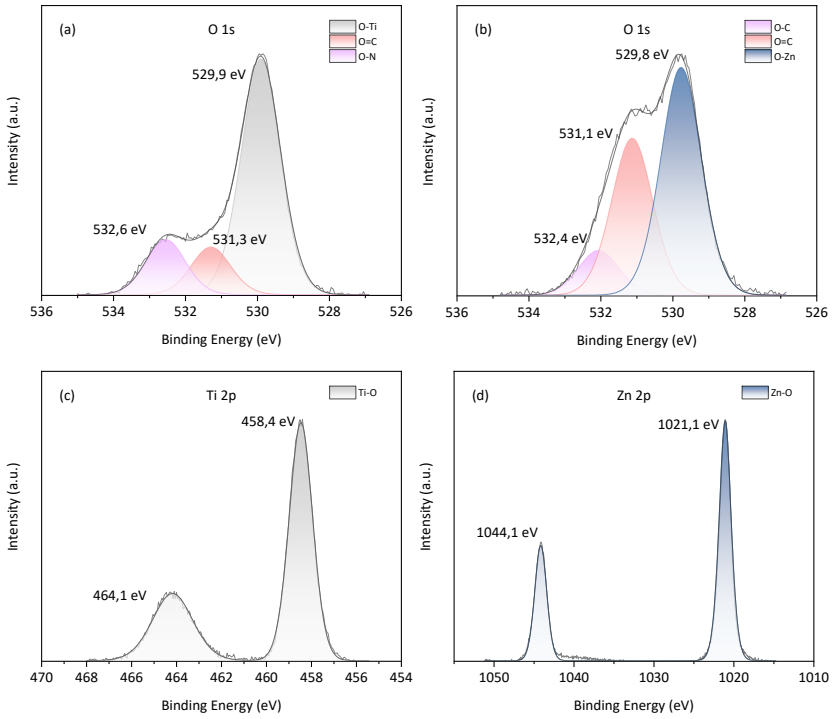

***Figure 3.15**: XPS spectra of O 1s of (a) hybrid Ti-HD and (b) Zn-HD, and (c) Ti 2p of hybrid Ti-HD, and (d) Zn 2p of Zn-HD.*

In conclusion, among the four hybrids (MC–Zn, MC–Ti, HD–Zn, and HD–Ti) , only the MC–Zn hybrid was successfully formed, revealing a clear preference for the reaction of malonyl chloride with zinc over titanium or the HD-based systems. For this reason, subsequent studies were focused exclusively on the properties of the MC–Zn hybrid.

3.3.3 Antibacterial properties of PA63 and MC-Zn hybrid material.

Both PA63 and MC-Zn hybrid coatings were tested for their antibacterial properties as described in the experimental section. **Figure 3.16** shows the number of viable bacteria on the uncoated substrates (jeans reference, PET reference, Carton reference, and Cotton reference), substrates coated with nylon 6,3 (PA63) and the MC-Zn hybrid. While untreated jeans permit bacterial attachment, jeans coated with either of the two films show no attachment of either of the bacteria. In contrast, the PET, coated with PA63 and MC-Zn, exhibited bacteriostatic activity against *S. aureus*, but not against *E. coli*. Cotton and carton inhibited the attachment completely after MC-Zn coating. However, only Carton coated with PA63 demonstrated bacteriostatic activity against *S. aureus*.

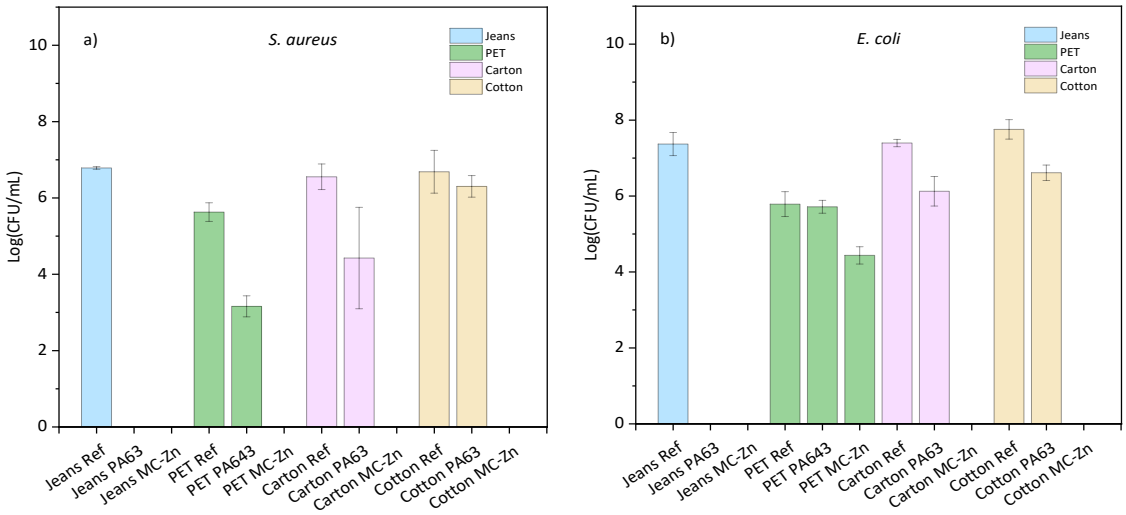

***Figure 3.16**: Antibacterial activity of the samples expressed as log (CFU/mL) against the bacteria Staphylococcus aureus (a) and Escherichia coli (b).*

Table 3.1 summarizes the results for the Bacterial Reduction Percentage (% BR). For being antibacterial, a material must show a minimum value of 99%, according to the ISO standard 22196. Overall, all the coated samples showed a reduction in bacterial attachment, although not all of them met the required bacterial reduction of >99% standard to be considered antimicrobial.

***Table 3.1**: Bacterial reduction percentage of the PA6,3 and MC-Zn coated substrates.*

	S. aureus	***E. coli***
Jeans PA63	100%	100%
Jeans MC-Zn	100%	100%
PET PA63	99,7%	24,6%
PET MC-Zn	100%	95,9%
Carton PA63	99,9%	93%
Carton MC-Zn	100%	100%
Cotton PA63	80,2%	93,1%
Cotton MC-Zn	100%	100%

Samples coated with the MC–Zn hybrid generally exhibited higher bacterial reduction (%BR) values than their PA63 counterparts. Jeans coated with either material achieved 100% BR for both bacterial strains. PET coatings were antibacterial against *S. aureus* but not against *E. coli*. Carton and cotton coated with PA63 showed similar bacterial reduction against *E. coli*, however, carton coated with PA63 displayed a bacteriostatic effect against *S. aureus*, whereas cotton coated with PA63 reached only 80.2% BR. Both substrates coated with MC–Zn achieved the maximum %BR.

The higher antibacterial activity observed for MC-Zn coatings compared to PA63 may be related to the presence of Zn^{2+} ions[68,69] or other chemical properties of the hybrid film, although the precise mechanisms were not directly investigated in this study. Differences in substrate behaviour, such as the lower effectiveness on PET, could be due to variations in surface morphology and chemistry. PET's smoother and more hydrophobic surface may affect bacterial adhesion, whereas the porous and fibrous structure of cotton and carton may influence coating-substrate interactions.

Thin film coatings can induce antibacterial activity in a substrate, but the effectiveness strongly depends on the nature of the coating material and the targeted microbes, as antibacterial effects are not universal across all bacterial types. The observed variation in activity across different substrates highlights the significant role of substrate morphology and surface chemistry in bacterial adhesion.[70] Interestingly, even after coating, the surface properties of the substrate influence bacterial interactions, likely due to differences in roughness and microstructure.

A similar effect to that reported in the literature for metal oxides was observed. The bacteriostatic activity of metal oxides relies on damaging the cell membranes of the bacteria through direct contact with metal ions and surface features, producing physical stress and electrostatic interactions. Although the cell walls of GRAM+ bacteria have a thicker peptidoglycan layer than GRAM- bacteria, it is directly accessible and more susceptible. GRAM-bacteria have an outer membrane that acts as a barrier, protecting this layer and making them more resistant to antibacterial methods and antibiotics than GRAM+ bacteria.[71]

Overall, these findings support the potential of MC–Zn hybrid coatings for antibacterial applications while emphasizing that effectiveness strongly depends on both the coating material and substrate properties. Further investigations with additional bacterial strains and substrate types are needed to identify general patterns and establish design rules for antibacterial coatings.

3.3.4 Antifungal properties of PA63 and hybrid MC-Zn

An experiment was designed to reveal antifungal properties of the two different coatings. It focused on the coatings' ability to inhibit the radial extension of actively growing *A. nidulans* colonies. **Figure 3.17a** shows two jeans samples (reference, PA63) positioned on a petri dish with a centrally seeded radial fungal growth. **Figure 3.17b** shows the same, but with cotton samples (Reference, PA63). The fungal colony grows without visible signs of local growth hindrance by any of the samples. Indeed, the samples become partly overgrown. Moreover, cotton reference seems to have hosted a dormant microbial species which activated during the incubation,

expanding to the medium and forming pink colonies that compete with A. nidulans. This species could not be identified but seems to be a biofilm-producing bacterium. It was effectively eliminated during the infiltration process due to the prolonged exposure to a higher temperature.

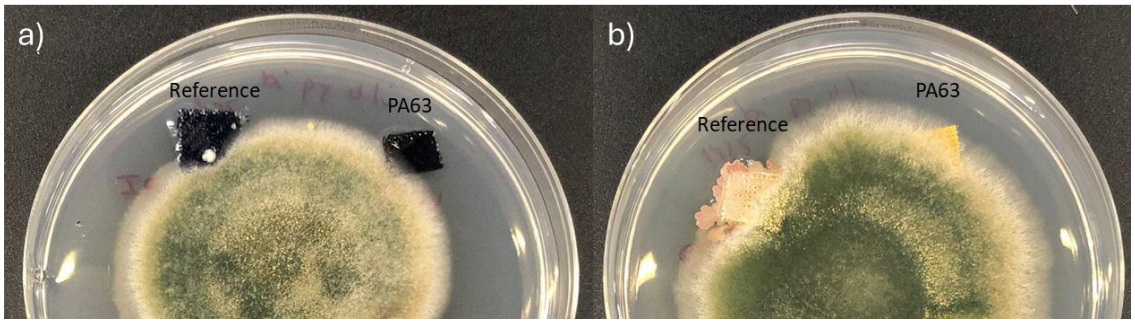

***Figure 3.17**: Effect of the coatings on the inhibition of radial extension growth of A. nidulans for jeans (a) and cotton (b).*

Once a fungus is growing as hyphae, it becomes more difficult to stop due to its continuous branching and adaptability to harsh conditions, such as nutrient deprivation.[72] Inhibiting hyphal growth requires interfering with these ongoing cellular processes, which is generally more challenging than targeting a single germination event. The results of the initial tests were unsatisfactory, as the employed strategy did not inhibit fungal growth. Consequently, we changed the approach and focused on testing spore germination in the second experiment.

Here, the initiation of growth from the seeded spores is in focus. For this, the four types of samples, i.e. (a) jeans, (b) PET, (c) carton, and (d) cotton, with and without coatings, were positioned on an agar plate and subjected to a spore solution and incubated. **Figure 3.18** presents the plates after 2 days of incubation for the different substrates.

ZnO coated jeans and cotton obtained from a separate project were included as a reference to compare their properties with those of the hybrid coatings.

Figure 3.18a shows a photograph of the uncoated (Reference) and coated (ZnO, PA63, and MC-Zn) jeans samples after incubation. The uncoated sample showed fungal growth. The PA63 coating reduced spore germination, but less than ZnO. The hybrid coating (MC-Zn) reduced the spore germination best, possibly due to accelerated Zn ion leaching from the sample.

In **Figure 3.18b** the PET-based samples after incubation are shown. Due to the thickness of the PET substrate, fungal growth patterns are not clearly visible. However, a reduction in spore germination appears to be present for the MC–Zn-coated PET, whereas the uncoated reference shows uniform fungal growth and the PA63-coated PET exhibits only minimal inhibition. These

observations suggest that MC–Zn may provide some antifungal effect on PET surfaces, although the effect is less visually pronounced due to the substrate morphology.

Figure 3.18c shows a Petri dish with different carton-based samples after incubation. The reference carton sample shows visible microbial growth. The MC-Zn sample exhibits some antifungal effect, although fungal presence is still noticeable. The PA63 sample appears significantly clearer, suggesting a stronger antifungal effect than the in other samples.

Figure 3.18d shows a Petri dish with cotton-based samples after incubation. The reference sample exhibits visible fungal growth, indicating no noteworthy activity. The ZnO and MC-Zn samples appear lighter, suggesting some antifungal effect. The PA63 sample shows almost no improvement in comparison with the uncoated sample. These results suggest that Zn-based coating exhibits the strongest activity among the tested materials.

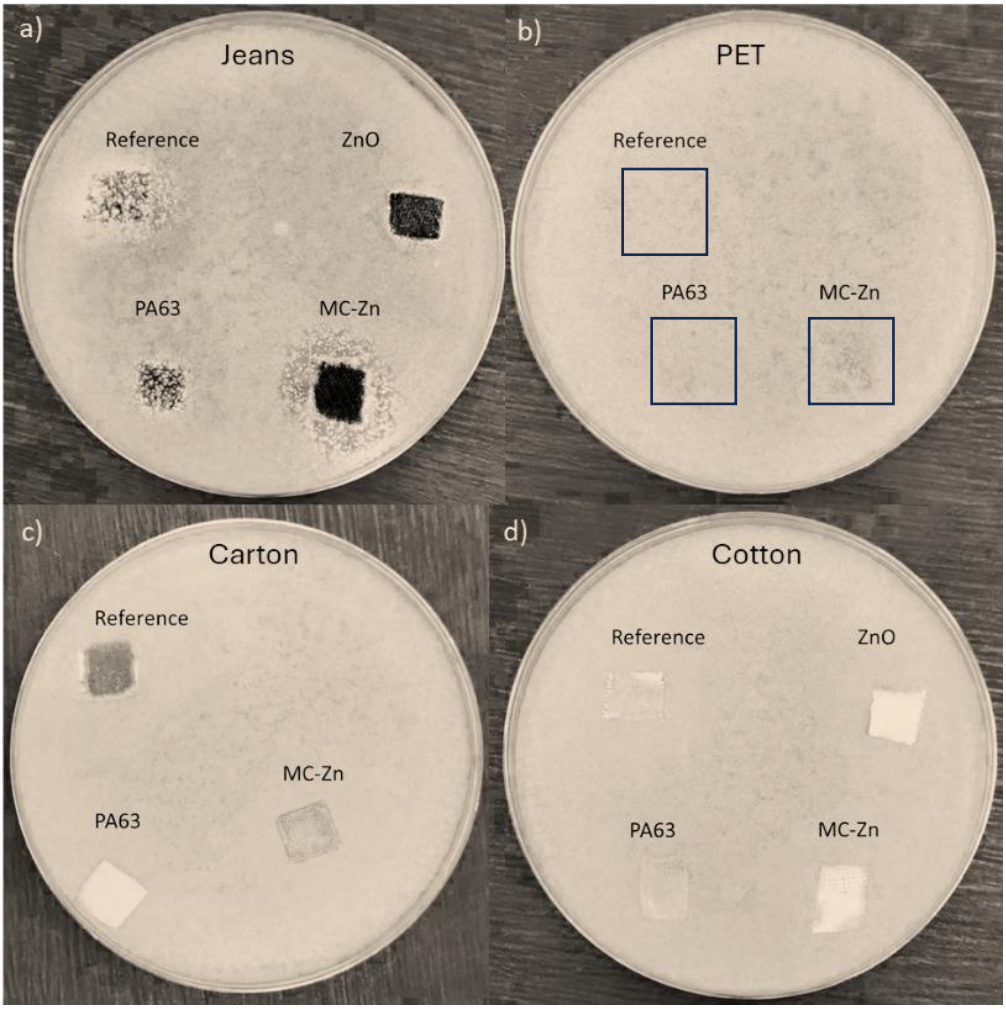

***Figure 3.18**: Effect of the coatings on spore germination on (a) jeans, (b) PET (note that the PET samples are transparent and difficult to recognize in the image), (c) carton, and (d) cotton.*

The antifungal performance of the different coatings varied with varying the substrate. Across all tested materials, the hybrid MC-Zn coating showed the most effective reduction in fungal spore

germination, particularly on jeans, likely due to enhanced Zn ion leaching. On carton substrates, PA63 demonstrated the strongest antifungal activity, while on cotton, both ZnO and MC-Zn coatings showed moderate effectiveness. Overall, Zn-based coatings exhibited superior antifungal properties compared to PA63 alone, confirming their potential for surface protection against fungal contamination.

The observations suggest that both the surface chemistry and the morphology play a role. While the flat PET samples do not have any considerable effect on the spore germination, the corrugated samples do. This implies that the surface structure is the dominating factor for antifungal properties. Nevertheless, the adopted surface chemistry (in form of coating) has an additional influence. The Zn-based coatings have a strong impact on jeans and cotton with the hybrid coating being more effective than ZnO in reducing spore germination. In the case of carton, the PA63 coating outperformed the Zn-based coatings. The reason for this discrepancy is not clear yet and appears to be more complex than in the other samples, thus it will be matter of future investigation.

3.3.5 Antimildew properties of PA63 and hybrid MC-Zn

The antimildew properties of the PA63 and MC-Zn coatings were tested on birch wood, cotton and carton substrates. For the analysis, both treated and untreated samples were exposed to the outdoor ambient environment for 15 days. The presence of mold was evaluated, and the samples were compared.

In **Figure 3.19**, birch wood samples are shown, which were kept for 15 days in ambient conditions. The samples in the upper row are the reference samples, while the samples in the lower row are MLD-treated with PA63. All samples were made in triplicate to ensure reproducibility. A visible reduction in mold growth is observed in the coated samples; however, all PA63-coated samples still exhibited some mold spots, indicating that the protective effect is only partial. This suggests that PA63 slows down fungal colonization but does not prevent it entirely. The observed reduction could be related to barrier effects of the polymer film, such as decreasing water absorption or limiting the availability of nutrients at the wood surface. At the same time, one possible reason for the remaining fungal growth is that the deposited coating may not be fully homogeneous across the wood surface. Due to the intrinsic porosity and roughness of wood, achieving uniform coverage with MLD can be challenging, and incomplete coating could leave sites available for fungal colonization. To address this, further experiments should be performed by modifying MLD parameters, such as precursor exposure time, number

of cycles, or surface pre-treatment, in order to improve coating uniformity and evaluate whether the residual mold formation is due to process limitations or to the intrinsic properties of PA63.

***Figure 3.19**: Birch wood samples exposed to ambient conditions for 15 days. Upper row: Untreated reference samples, and lower row: samples coated with PA63.*

To evaluate the antifungal properties of PA63 coatings on a different substrate, cotton samples were tested under the same ambient conditions as the birch wood experiments. Three sample types were prepared: untreated, uncoated but heated in vacuum under identical MLD conditions (heat control), and PA63-coated. After 15 days of environmental exposure, all samples were placed on Sabouraud Dextrose agar plates (a solid culture medium, specifically enriched to promote the isolation and growth of fungi, including yeasts, molds, and dermatophytes) and incubated overnight at 37 °C in darkness. This step allowed any viable fungi present to grow under controlled conditions, enabling direct comparison of fungal colonization.

Some mold was still observed on all coated samples, which may be related to the structure of the cotton surface or variations in coating coverage. These results are consistent with the observations on birch wood, indicating that PA63 coatings can provide partial protection against fungal colonization on different substrates. **Figure 3.20** shows that untreated and heat-treated cotton exhibited extensive mold growth, whereas PA63-coated samples showed a clear reduction in fungal colonization.

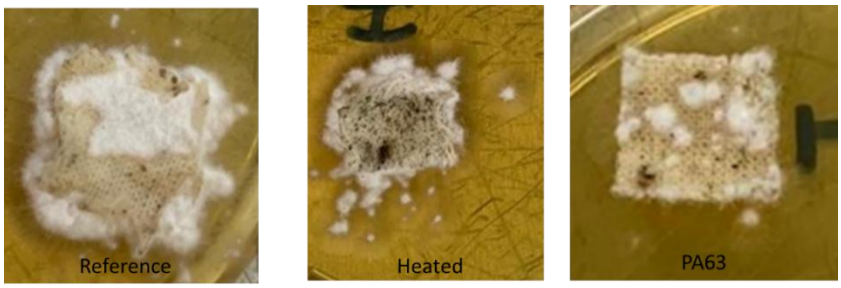

***Figure 3.20**: Cotton reference, heated cotton, and cotton coated with PA63 after exposure to ambient conditions for 15 days.*

This confirms that PA63 slows down fungal growth on cotton, while the heat control demonstrates that the effect is due to the coating and not thermal treatment. Some mold was still observed on all coated samples, which may be related to the structure of the cotton surface or variations in coating coverage. These results are consistent with the observations on birch wood, indicating that PA63 coatings can provide partial protection against fungal colonization on different substrates.

In the second set of experiments, 2 mL of water were added directly onto the surface of each sample (birch wood, cotton and carton) to create a high-humidity environment. The samples were incubated at 37°C in darkness for 21 days. The incubation period was extended in comparison with the previous experiments due to the less aggressive condition. Because the samples were maintained in a controlled high-humidity environment, any observed mold growth can be attributed solely to the substrate's moisture content and nutrient availability. This setup enables a focused assessment of the antifungal properties of the PA63 coating.

The photograph in **Figure 3.21** shows birch wood samples, uncoated (top row) and coated with PA63 (bottom row) after the incubation. The uncoated samples show remarkable mildew formation, whereas the PA63-coated samples exhibit reduced contamination, suggesting a potential antifungal effect of the coating. Among the three PA63-coated samples, one showed fungal growth, which may be attributed to inhomogeneity in the deposited coating, highlighting the importance of uniform coverage for optimal antifungal performance. These findings are consistent with previous experiments under ambient conditions.

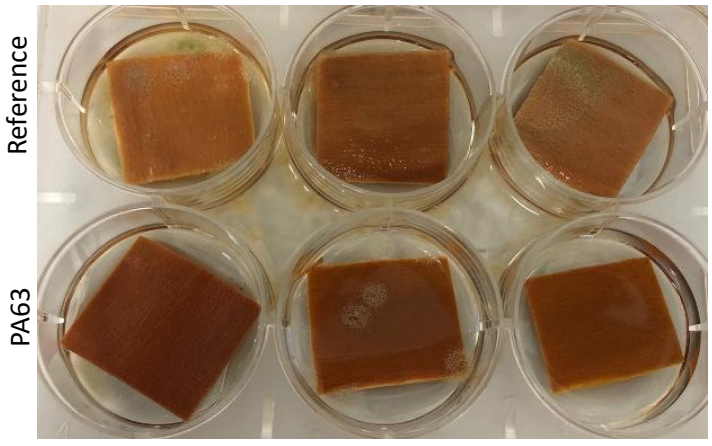

***Figure 3.21**: Reference wood samples (top) and wood samples coated with PA64 (bottom) after 21 days of storage at 37°C in darkness.*

To further evaluate the antimildew performance of the coatings across different substrates, the same high-humidity incubation experiment was extended to include MC-Zn-coated cotton and

carton samples, in addition to PA63-coated samples. This allowed a direct comparison of the antimildew efficacy of the hybrid MC-Zn coating with PA63 under identical controlled conditions.

In the case of carton (**Figure 3.22**), the reference sample showed visible mildew formation, while PA63-coated samples exhibited reduced contamination. MC-Zn-coated samples showed no apparent mildew, indicating a stronger antimildew effect of the hybrid coating under the tested conditions. These results are consistent with the trends observed in the antibacterial tests, where MC-Zn coatings generally outperformed PA63. Presence of Zn^{2+} ions is known to contribute to antibacterial effects, and it is likely that a similar mechanism contributes to the reduced mildew formation observed.[68,69,71]

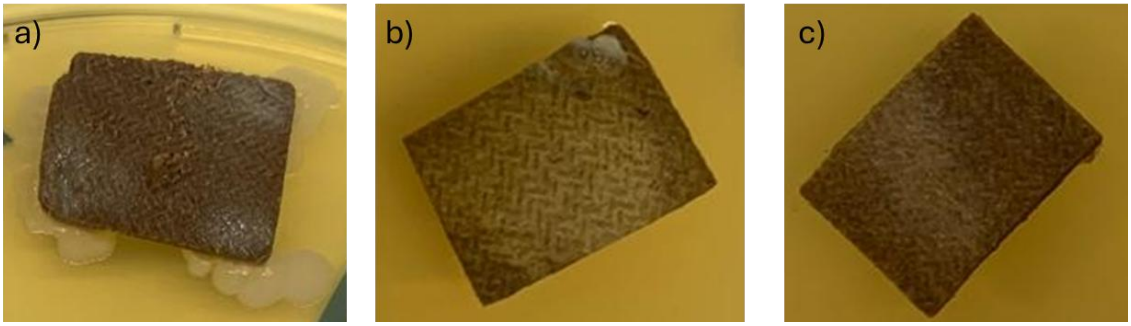

***Figure 3.22**: Antimildew test for carton samples: (a) reference, (b) PA63-coated and (c) MC-Zn-coated.*

The same test was also done with cotton samples, see **Figure 3.23**. The reference sample showed the most pronounced mildew growth, while PA63- and MC-Zn-coated samples exhibited little to no apparent mildew, indicating a stronger antimildew effect. The observed performance of PA63 may be attributed to improved coating homogeneity on this substrate and the less aggressive conditions of the controlled antimildew test. The results for MC-Zn are consistent with previous observations, confirming its superior antimildew efficacy.

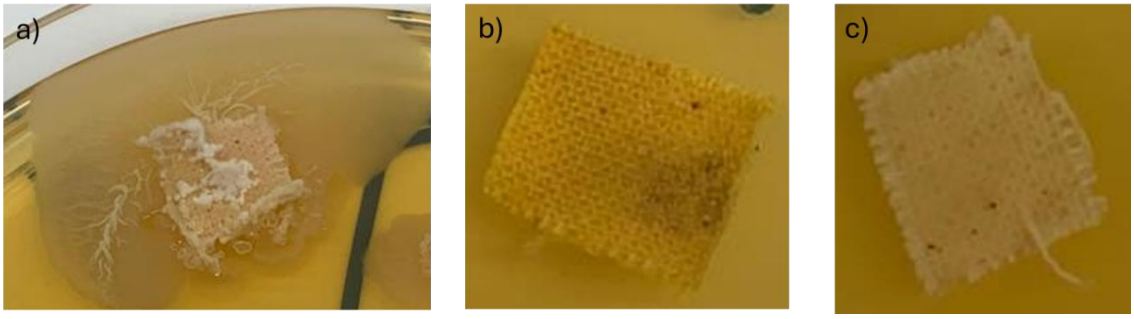

***Figure 3.23**: Antimildew test for cotton samples: (a) reference, (b) PA63-coated and (c) MC-Zn-coated.*

The antimildew tests on PA63 and MC-Zn coatings demonstrated effective mildew prevention across different substrates. On birch wood, PA63-coated samples showed reduced mold growth compared to untreated ones, both in ambient exposure and under high-humidity incubation,

confirming its protective effect. In carton samples, visible mildew was observed on the uncoated reference, while PA63 provided moderate inhibition. MC-Zn-coated samples remained free of visible mildew, indicating a stronger antimildew performance. For cotton, the untreated sample exhibited significant mold formation. In contrast, PA63 reduced mildew presence, likely aided by better coating homogeneity and the controlled incubation conditions, whereas MC-Zn offered the highest level of protection, showing minimal contamination after incubation.

Both PA63 and MC-Zn coatings showed improved antimildew performance compared to the untreated substrates However, further experiments are needed to determine whether the remaining mildew is due to inhomogeneity in the coating or reflects inherent limitations of the antimildew activity of these coatings.

3.3.6 Effect of the coating on seeds germination

In this first experiment, the germination of lentil seeds on cotton as substrate was investigated. This was done by placing the seed atop untreated cotton, cotton heated under MLD conditions, and PA63-coated cotton and observing their germination over time. Each plate was supplied with 2 mL of water, sealed, and kept at ambient temperature and light conditions.

Figure 3.24 illustrates the germination process of the lentil seeds on the various cotton substrates over 21 days. The germination started first on the PA63-coated cotton. By day 21, the positive effect of the PA63 coating on the seed germination was evident, promoting faster and possibly more robust growth than the other cotton substrates. This observation may be related to the improved antibacterial and antimildew properties of PA63-coated cotton, which could provide a more favorable microenvironment for seed germination

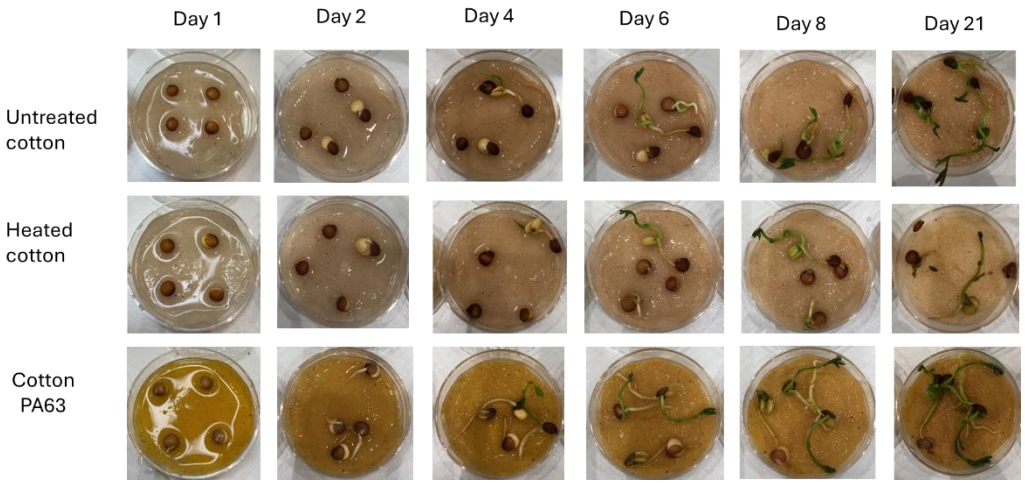

***Figure 3.24**: Germination process of lentil seeds on untreated, heated and PA63 coated cotton over 21 days.*

The experiment was repeated with doubled seed quantity. After one month, the germination was considerably advanced for the seeds placed on PA63-coated cotton, as shown in **Figure 3.25**.

***Figure 3.25**: Germination process of lentil seeds on untreated and PA63 coated cotton after one month.*

The experiment was repeated in darkness to test whether the PA63 coating could also promote the early stages of germination under unfavorable conditions for plant development. **Figure 3.26** shows that after 7 days the PA63-coated cotton promoted seed germination more effectively than the untreated cotton, similar to the trend observed in the light-exposed experiments. However, unlike under light conditions, where germination continued over several weeks, in darkness all seeds inactivated after 7 days, indicating that while PA63 may stimulate the initial germination phase, further development requires light and is not sustained by the coating.

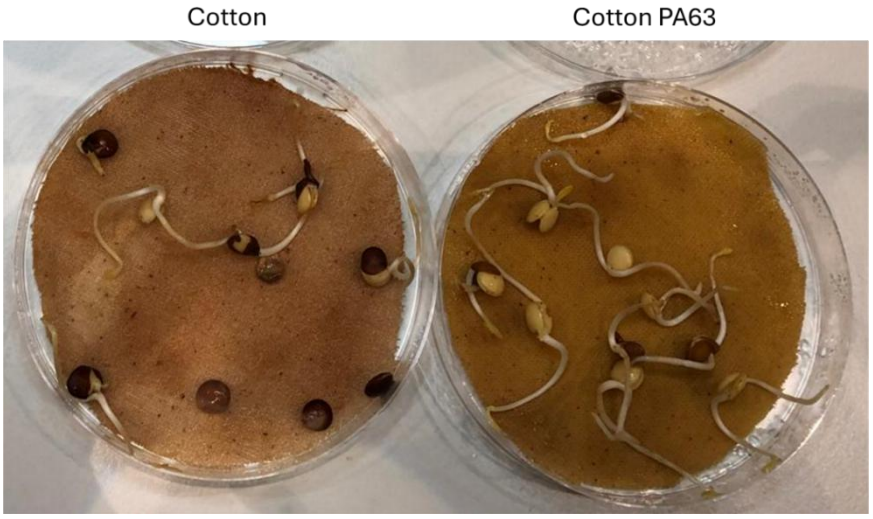

***Figure 3.26**: Germination process of lentil seeds on untreated and PA63 coated cotton after 7 days in darkness.*

In the last experiment additional samples, namely cotton coated with hybrid MC-Zn and with ZnO, were added as additional substrates. **Figure 3.27** shows the germination state on each of the five samples (untreated, heated, coated with PA63, MC-Zn, and ZnO) after 4 days. Among them, PA63-coated cotton promoted germination most effectively, followed by ZnO-coated cotton. Interestingly, and in contrast to the antimildew tests, the MC-Zn-coated cotton was negatively affected by mold growth, suggesting that the hybrid coating may not provide the same balance between antifungal protection and seed compatibility as observed for PA63.

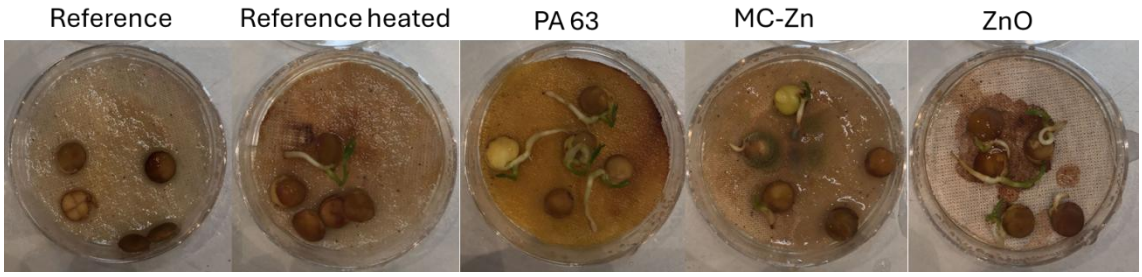

***Figure 3.27**: Germination process of lentil seeds on untreated, heated, PA63-, MC-Zn- and ZnO- coated cotton after 4 days.*

PA63-coated cotton significantly improved lentil seed germination compared to untreated and heated cotton, promoting faster and stronger growth. This was further confirmed with a higher seed quantity, where PA63-coated cotton showed the most advanced germination. Under dark conditions, PA63 still outperformed untreated cotton within 7 days, although all seeds died by day 7.

The higher germination observed in cotton coated with PA63 could be related to a greater hydrophilicity of the coating, which might improve substrate wetting and allow a more uniform water supply to the seed during imbibition. Additionally, the amide groups in PA63 could possibly interact via hydrogen bonding with proteins in the seed coat, enhancing contact between the seed and the cotton. In contrast, the MC–Zn hybrid might release Zn^{2+} ions or acidic byproducts freely into the surrounding substrate, potentially generating a microenvironment with reduced pH and concentrations of Zn that could be phytotoxic, which would be consistent with the lower germination observed. Overall, these features could hypothetically explain the differences in seed viability between the tested coatings.

3.4 CONCLUSIONS

The MLD process for Nylon 6,3 successfully produced uniform films exhibiting linear growth, with thickness increasing proportionally to the number of deposition cycles. The process is highly temperature-dependent, with the growth per cycle (GPC) reaching a maximum at 70 °C before

declining, consistent with trends observed in other polyamide MLD processes. FTIR and XPS analyses confirmed the complete conversion of precursors and the absence of residual reactants, validating the chemical integrity of the films. QCM studies demonstrated a reproducible and linear mass gain per cycle, reflecting the controlled nature of the deposition process.

The hybrid materials formed by combining organic precursors such as MC with inorganic precursors showed differences depending on the metal: DEZ allowed the incorporation of zinc into the hybrid, whereas $TiCl_4$ did not react effectively with MC, mainly producing titanium dioxide (TiO_2) instead of an organic–inorganic hybrid. MC residue was detected in the hybrid coatings, but the presence of zinc was confirmed, demonstrating successful hybrid formation only with DEZ.

MC-Zn coatings showed higher antibacterial efficacy than PA63, with effectiveness depending on both substrate type and bacterial strain; all coatings fully inhibited *S. aureus* on jeans, PET, and cotton, while only MC-Zn was fully effective on carton. For *E. coli*, MC-Zn achieved complete or near-complete inhibition on all substrates, whereas PA63 was largely ineffective except on jeans. These results highlight the key roles of coating composition, Zn^{2+} ions, and substrate properties in antibacterial performance.

In antifungal tests, PA63 and MC-Zn coatings demonstrated variable inhibition of fungal spore germination, with MC-Zn showing the most pronounced reduction, especially on jeans. PA63 exhibited a more modest antifungal effect, particularly on carton. These results emphasize the importance of both surface chemistry and substrate morphology in determining the effectiveness of antifungal coatings.

The antifungal performance of the coatings depended on both substrate type and surface properties. Across all tested materials, the MC-Zn hybrid coating showed the most effective reduction in fungal spore germination, particularly on jeans, likely due to enhanced Zn ion leaching. On carton, PA63 exhibited the strongest antifungal activity, whereas on cotton, both ZnO and MC-Zn coatings showed moderate effectiveness. Flat PET surfaces had minimal effect, while corrugated surfaces enhanced antifungal performance, indicating that surface morphology plays a dominant role, with surface chemistry (coating) providing an additional contribution.

Antimildew tests showed that both PA63 and MC-Zn coatings provided substantial protection against mildew growth under humid conditions. PA63 offered moderate protection, whereas MC-Zn hybrid coatings delivered superior mildew resistance on cotton and birch wood, highlighting the advantage of zinc-containing hybrids for environments prone to moisture and fungal growth.

Regarding seed germination, PA63-coated cotton promoted the fastest and most robust lentil seed growth. This may be related to the higher hydrophilicity of the PA63 coating, which could improve substrate wetting and provide a more uniform water supply to the seeds during imbibition. Additionally, the amide groups in PA63 might interact with proteins in the seed coat, potentially enhancing contact between the seed and the cotton. In contrast, the MC-Zn coating, while effective against mildew, negatively impacted seed germination, likely due to the release of Zn^{2+} and acidic byproducts that create a microenvironment less favorable for germination.

Overall, the results demonstrate the versatility of PA63 and MC-Zn coatings for antibacterial, antifungal, and antimildew applications. However, coating performance is strongly dependent on both the material composition and the substrate characteristics. Nevertheless, in a optimized material and process setup, PA63 promises good application potential in controlled cultivation and sustainable farming as well as healthcare by suppressing mildew.

***Table 3.2**: Summary of the antibacterial, antifungal and antimildew results.*

	ANTIBACTERIAL		ANTIFUNGAL	ANTIMILDEW	SEED GERMINATION
	S. aureus	*E. coli*			
Jeans PA63	✓	✓	✓	-	-
Jeans MC-Zn	✓	✓	✓	-	-
PET PA63	✓	✗	?	-	-
PET MC-Zn	✓	✗	? /✓	-	-
Carton PA63	✓	✗	? /✓	✓	-
Carton MC-Zn	✓	✓	? /✓	✓	-
Cotton PA63	✗	✗	✗	✓	✓
Cotton MC-Zn	✓	✓	✓	✓	✗

Chapter 4 PHOTOCATALYTIC DEGRADATION OF NITROGEN OXIDES (NOx) BY POROUS TIO2–COATED GLASSES FROM HYBRID INORGANIC–ORGANIC THIN FILMS PREPARED BY A COMBINED ALD/MLD DEPOSITION STRATEGY.

4.1 INTRODUCTION

The combustion of fossil fuels in mobile and stationary power sources results in the generation of various nitrogen oxides (NO_X), which are key contributors to the photochemical smog and air pollution in urban areas. Photochemical smog consists mainly of tropospheric ozone (O_3), peroxyacyl nitrates (PANs), particulate matter (PM), and nitric acid. The latter is formed by the reaction of NO_2 with water, whilst the generation of radicals by the interaction of NO_X and sunlight is, to a great extent, the origin of O_3, PANs and PM. The environmental and health related problems associated with the emissions of NO_X are diverse and include *(i)* acidic depositions, which are harmful to aquatic life, crops and forests, and *(ii)* adverse effects on human health, which primarily affect the respiratory and cardiovascular systems. In this context, the development of systems that reduce the concentration of NO_X in the atmosphere is of paramount importance to improve the quality of life in major cities.[73,74,75]

Titanium dioxide (TiO_2) is a prolific semiconductor photocatalyst [76,77,78,79,80] that has shown activity in the degradation of NO_X via UV irradiation, since the band-gap of these materials usually ranges approximately from 3.0 to 3.2 eV. Shorter wavelength absorption has been achieved by doping with nitrogen and transition metals, which allows the photocatalyst to work under visible light irradiation.[81]

TiO_2 exists in nature in three crystalline phases; namely, anatase, rutile and brookite.[82,83,84] Rutile is the most thermodynamically stable phase, while anatase and brookite are metastable and, therefore, may be converted irreversibly into the rutile phase at high temperatures.[85,86,87,88,89] The physical and chemical properties of TiO_2 depend on the structural parameters of each polymorph, which determines the photocatalytic activity of the material. TiO_2-anatase shows better catalytic performance than TiO_2-rutile due to (i) greater number of active sites (oxygen vacancies), and (ii) the broader band-gap of anatase (3.20 eV for anatase and 3.02 eV for rutile),

which results in a slightly superior redox capability.[90] The photocatalytic activity of TiO_2-anatase may be improved by increasing the porosity of the material.[91] This porosity may be achieved by supporting the TiO_2 on intrinsically porous surfaces, such as, zeolites, tiles, ceramics or asphalt pavement[80,92,93,94] or by the preparation of porous TiO_2 materials.[95,96,97,98,99,100,101,102,103]

The MLD technique is a variation of ALD that makes use of molecular organic and inorganic precursors, thus allowing for the formation of molecular layers or the preparation of hybrid inorganic-organic films, respectively. The use of $TiCl_4$ and bifunctional organic reactants (e.g., ethylene glycol, glycerol or hydroquinone) as precursors has been reported as a suitable method for the preparation of titanicone thin-films.[104,105,106] The successive provision of $TiCl_4$ and organic spacers during MLD processes leads to the formation of an inorganic-organic film. Subsequent thermal annealing causes the combustion and removal of the organic spacers, thus creating cavities in the structure that eventually result in the formation of porous TiO_2.[33,107,108,109] This apparently simple methodology, however, has shortcomings regarding the size of the spacer and the conditions employed for the thermal annealing. The former involves the difficult vaporization of large molecules under MLD conditions, limiting the range of available pore sizes. The latter is caused by the fact that high temperatures and long annealing times are required for the formation of anatase from amorphous TiO_2, but the collapse of the porous structure, and even anatase-to-rutile phase transformation, may occur under these conditions.[34] Therefore, fine-tunning of MLD and annealing conditions is key to achieving appropriate porosity and anatase proportions able to induce photocatalytic activity.

The activity of TiO_2, deposited by MLD, has been investigated by employing benchmark test reactions such as the photodegradation of methylene blue,[34,110,111] Azure B[112] or porphyrin.[113] However, to the best of our knowledge, in contrast to TiO_2 coatings deposited by other techniques,[114] the photodegradation of NO_x remains unexplored for TiO_2 films generated by MLD.

The photocatalytic removal of nitric oxide (NO) employing functionalized ceramic materials is regulated by the ISO 22197-1:2007, thus providing a standardized methodology to test the photocatalytic activity of different coatings and substrates. In the case of TiO_2 surfaces, the oxidation of NO under UV-irradiation entails the set of reactions depicted in **Figure 4.1**. The irradiation of TiO_2 with UV-light (< 387 nm) triggers the creation of electron (e^-) / hole (h^+) pairs as electrons are excited from the valence to the conduction band. H_2O molecules or OH^- ions adsorbed on the TiO_2 surface react with the holes, while adsorbed O_2 is reduced by an electron. These reactions yield hydroxyl (OH•) and superoxide (O_2^-•) radicals, which are responsible for the oxidation of NO_x. Ultimately, the oxidation of NO_x leads to the formation of HNO_3 and NO_3^-

on the TiO_2 surface (Scheme 1).[115] The build-up of these species on the TiO_2 surface deactivates the photocatalyst, which is re-activated by rinsing the surface with water.[116]

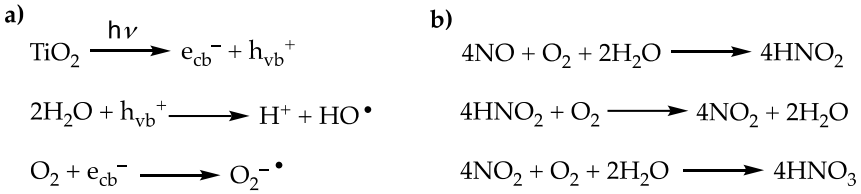

***Figure 4.1**: a) Generation of hydroxyl and superoxide radicals. b) Overall photocatalytic reactions for the oxidation of NO on a TiO_2 surface.*

4.2 EXPERIMENTAL PART

The studies were carried out on flat soda-lime glasses of 100 x 50 x 6 mm (height, width and thickness), manufactured by Guardian, coated with a 10 nm thin film of SiO_2 deposited by PVD (Physical Vapor Deposition-Magnetron Sputtering) at the Department of Applied Physics of the University of Zaragoza.[117] Previously, the glasses were washed with water and soap and dried on absorbent paper. The role of the SiO_2 coating is to inhibit the diffusion of alkaline ions from the glass substrate into the photocatalytic coating during the annealing process.[118]

The ALD/MLD depositions were carried out in a PLAY Series ALD reactor (CTECHnano, Coating Technologies S.L) using nitrogen (N_2) as a carrier gas for the precursors and as a purging gas. Flat soda-lime glasses with 10 nm of SiO_2 coating by sputtering and silicon wafers were used as substrates. Different titanium-based coatings were tested.

Films were deposited using titanium tetrachloride ($TiCl_4$; Honeywell Fluka ≥99.0%), water, ethylene glycol (EG; Sigma-Aldrich 99.8%), glycerol (GL; Sigma-Aldrich ≥99.5%) and hydroquinone (HQ; Sigma-Aldrich ≥99.5%) as precursors for the different processes. After the deposition, the samples were subjected to a thermal treatment.

Film thicknesses were determined by means of X-ray reflectivity (XRR) in a X'Pert PRO PANalytical X-ray diffractometer. Scanning Electron Microscopy (SEM) and High-Resolution Transmission Electron Microscopy (HRTEM) images of the coated-glasses were obtained using eSEM-FEI QuantaTM 250 and FEI Titan 80-300 TEM microscopes, respectively, at the Structural-Morphology Characterization Service of CIC NanoGUNE. Raman spectra were recorded on a JASCO NRS 3100 dispersive Raman spectrometer, equipped with a high-performance green laser (532 nm, 20 mW) and 1800 line grating. The spectra were recorded at the Chromatography and Spectroscopy service of the ISQCH (Instituto de Síntesis Química y Catálisis Homogénea). The

spectra are the result of subtracting the glass signal from the Raman spectra of the coated glasses.

The photocatalytic activity of the coated glasses was measured in an inert flat-bed photoreactor designed and manufactured by the company Ariño Duglass according to ISO 22197- 1:2007.[39] The experimental setup, including the gas supply, photoreactor, and analytical system, is shown in **Figure 4.2**. The photoreactor consists of a stainless-steel reaction chamber, designed to host 50 cm^2 glass samples (50 mm x 100 mm) of variable thicknesses on teflon holders equipped with a borosilicate glass window. The irradiation source was a 36 W black light (Philips Actinic BL TL-DK) placed over the reactor 6.5 cm from the sample with an irradiance (incident power/area) of 10 W/m^2. The reactor was fed with a NO/N_2 certified mixture as polluting gas (120 ppm of NO(g), Nippon Gases) and high purity synthetic air (Nippon Gases). A stream of air was bubbled through a gas wash bottle containing water to control the humidity. The dry air, moist air and N_2/NO streams were regulated with mass flow controllers (Bronkhorst, F-201CV) and mixed to obtain the desired NO(g) concentration. The system is equipped with a stainless-steel static gas mixer (Koflo Pipe Mixer) before the reactor inlet, and temperature and humidity sensors at the reactor inlet and outlet. The gas flows were: 1.50 and 1.47 L/min for dry and wet synthetic air, respectively, and 30 mL/min for the N_2/NO polluting gas. After a stabilization period, the concentration of NO(g) through the reactor was 1 ± 0.05 ppm with a flow rate of 3 L/min. NO(g) and NO_2(g) concentrations in the outlet gas stream from the reactor were continuously monitored by using electrochemical gas sensors (Alphasense Ltd, NO-A4 and NO_2-A4F3). The concentration of both gases, temperature and humidity data were recorded in a computer by using software designed by the Electronic Instrumentation Service (SAI) from the University of Zaragoza for this purpose. The outlet gas stream is bubbled through a gas wash bottle containing a concentrated NaOH solution.

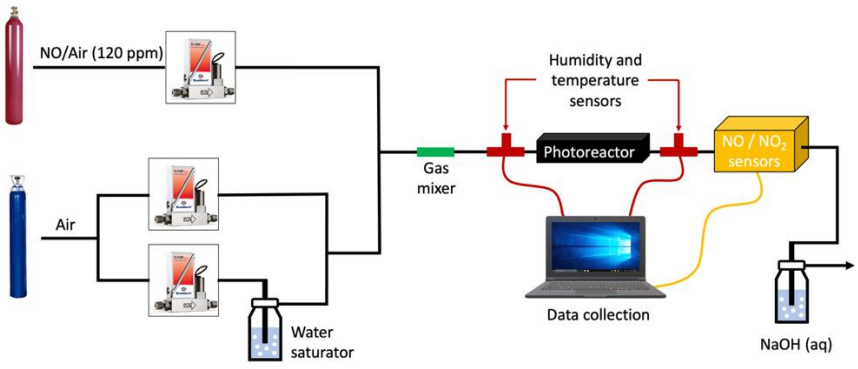

Figure 4.2: Schematic representation of the experimental setup for the measurement of the photocatalytic activity.

The photocatalytic tests were performed at room temperature with a relative humidity of 50% at 25 °C. The measurements were carried out continuously for 4-5 h with an automatic data collection every 7 seconds. After the measurement, the coated glasses were washed with distilled water to determine the NO_3^- concentration using a colorimetric indicator. Coated glasses with significant photocatalytic activity were washed with Milli-Q water, dried on an absorbent paper and subjected to successive photocatalytic measurements every 24 h under the same conditions.

4.3 RESULTS

4.3.1 Photocatalytic coatings on glass with thin TiO_2 films.

Titanium oxide (TiO_2) was deposited using titanium tetrachloride ($TiCl_4$; Honeywell Fluka ≥99.0%) and water as precursors, applying following pulse sequence: $TiCl_4$ (0.2 s)/N_2 (40 s)/H_2O (0.2 s)/N_2 (45 s). This sequence was repeated 600 times (cycles) at a process temperature of 180 °C. After the process, the coated glass was annealed at 400°C for 3 hours to convert the amorphous TiO_2 into the anatase crystalline phase. **Figure 4.3** indicates no photocatalytic activity of the TiO_2-coated glass in the degradation of NO.

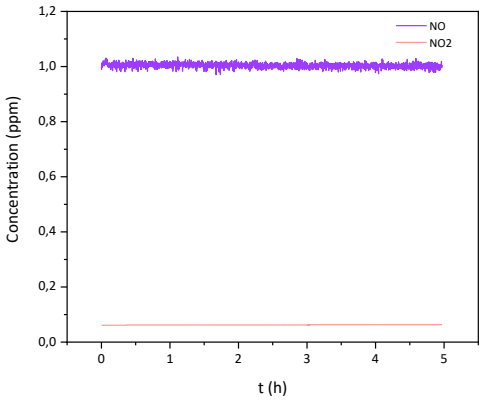

***Figure 4.3**: Photocatalytic activity of glass with a TiO_2 film grown from $TiCl_4$ and H_2O at 180°C. Thermal treatment: 3 hours at 400°C.*

The Raman spectrum in **Figure 4.4** shows three strong characteristic absorptions at 639, 513 and 399 cm^{-1}, all of which correspond to the anatase phase. No absorption bands stemming from the rutile phase were observed. The reduced photocatalytic activity, despite the presence of the anatase phase, could be attributed to the material's low porosity, which may limit the accessible surface area and hinder effective interaction with reactants.

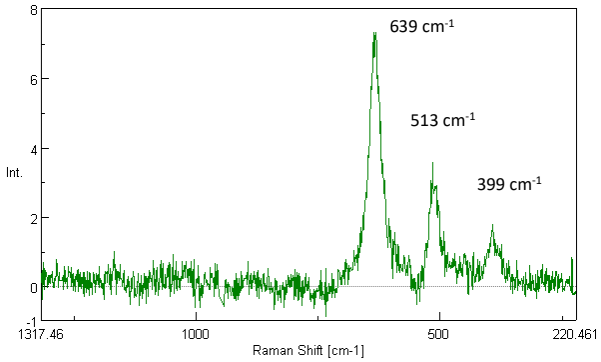

***Figure 4.4**: Raman spectra of an ALD TiO_2-coated glass ($TiCl_4/H_2O$). Absorption bands: 639, 513, 399 cm^{-1}.*

4.3.2 Photocatalytic coatings on glass from titanicone thin films.

To increase the porosity of the coating material, an organic precursor was used to fabricate hybrid inorganic-organic thin films. The films were prepared according to the procedure described in literature.[104] The titanicone coatings were deposited using $TiCl_4$ and ethylene glycol (EG), a volatile diol, as precursors applying the following pulse sequence: $TiCl_4$ (0.3 s)/15 s/N_2 (80 s)/EG (1 s, 70 °C)/15 s/N_2 (90 s). An exposure step was introduced between the precursor pulse and purge, providing sufficient time for the precursors to react. This cycle was repeated 200 times at a process temperature of 110 °C.

In parallel, the deposition was also performed on silicon wafers (1 cm x 1 cm) to determine the thickness of the coating by XRR. The measured film thickness after 200 cycles was about 90 nm, which corresponds to a GPC of 0.45 nm/cycle. Finally, the sample was annealed at 400 °C for 2 h in air to remove the organic component and transform the amorphous TiO_2 into anatase, which resulted in uniform and transparent coated glass. The thickness of the coating was reduced to 30 nm after the thermal treatment, which agrees with the elimination of the organic groups interconnecting the titanium within the hybrid material.

The photocatalytic degradation of NO(g) with the coated glass is shown in **Figure 4.5**. As can be seen, the NO(g) concentration is slightly reduced, by 0.04 ppm, once the illumination is turned on and it is maintained over the complete 4 h of the experiment until the illumination is turned off. NO_2(g) formation was not observed.

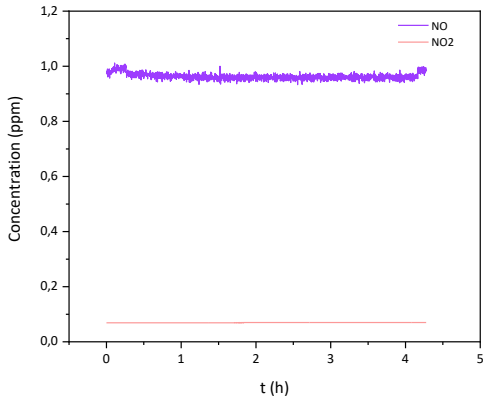

***Figure 4.5**: Photocatalytic activity of a TiO_2-coated glass after 2 hours thermal treatment at 400°C of an organic-inorganic film grown from $TiCl_4$ and EG (70°C) at 110°C.*

SEM analysis of the surface morphology showed no evidence of porosity (**Figure 4.6**). The coating thickness, determined from the cross-sectional image, was approximately 20 nm, which is of the same order of magnitude as that determined by XRR (30 nm).

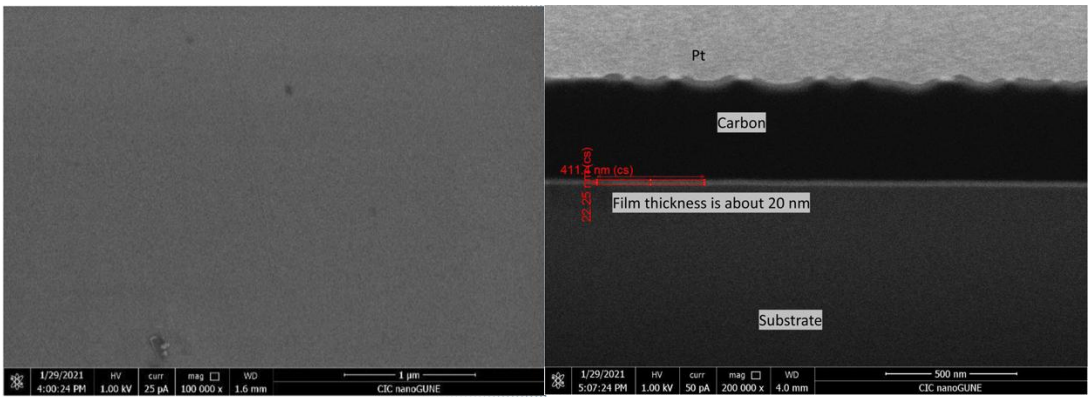

***Figure 4.6**: SEM Top view (left) and cross-sectional view (right) of a coated glass, fabricated from an MLD titanicone thin film ($TiCl_4$/EG).*

To increase the porosity of the coatings, the possibility of using larger organic molecules to increase the inter-titania spacing was explored. The deposition of the organic-inorganic film was performed using $TiCl_4$ and glycerol (GL) as reactants under the following pulse sequence: $TiCl_4$ (0.8 s)/15 s/N_2 (65 s)/GL (0.8 s, 120 °C)/15 s/N_2 (70 s). An exposure step was introduced between the precursor pulse and purge. The cycle was repeated 300 times at a process temperature of 150 °C. The resulting coated glass maintained transparency after a thermal treatment at 400°C for 2 hours. As can be seen in **Figure 4.7**, it showed almost no photocatalytic activity. GL is a triol, which should facilitate the formation of the organic-inorganic film and the generation of a coating with enhanced porosity. However, a significant limitation of using GL as a porosity-inducing agent lies in its high boiling point (290°C) compared to that of EG (197°C). It is likely

that, under the conditions in which the deposition was performed, the supply of GL vapors was not sufficient, even upon increasing the GL temperature to the maximum of 120°C.

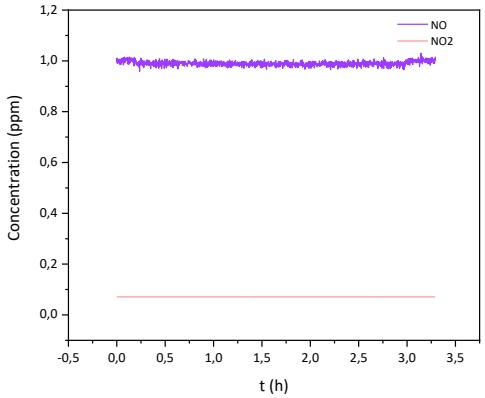

Figure 4.7: Photocatalytic activity of a TiO_2-coated glass after an organic-inorganic film was deposited using $TiCl_4$ and GL (120°C) at 150°C and the sample was thermally treated for 2 hours at 400°C.

Raman spectra (**Figure 4.8**) show no anatase phase, which is consistent with the lack of photocatalytic activity.

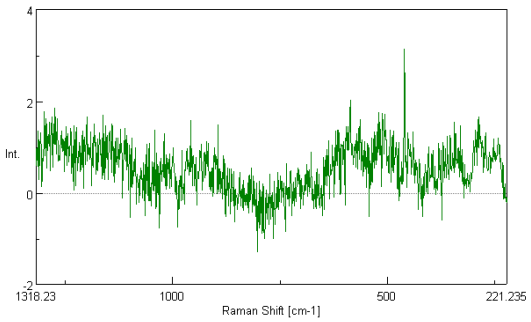

Figure 4.8: Raman spectra of a coated glass fabricated from an MLD thin film ($TiCl_4$/GL).

The influence of thermal treatment on the photocatalytic activity of the coated glasses has been investigated as well. Adjustments in temperature ramps and holding times during calcination can impact crystal size and surface area, thereby modifying the photocatalytic properties. Cooling should also be gradual, to avoid structural damage. Additionally, preheating at 150–200°C to remove residual precursors or water can further optimize the process, ensuring high surface area and controlled crystallization. Thus, a Ti-EG film, deposited on glass by MLD under the same conditions as described above, was subjected to a different annealing program. First, an instantaneous temperature rise to 250 °C was applied, a temperature ramp to 450 °C in 90 min (2.2°C/min), and finally 3 hours hold at that temperature. The resulting coated glass showed a slightly higher photocatalytic activity than the glass treated at 400 °C, with a reduction of the

NO(g) concentration of 0.05 ppm over 4 h (**Figure 4.9**). The slight improvement in the photocatalytic activity prompted us to apply these conditions in the following experiments.

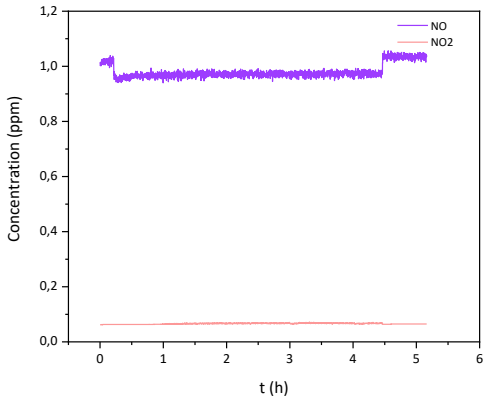

***Figure 4.9**: Photocatalytic activity of a glass, coated with an organic-inorganic film using $TiCl_4$ and EG (70°C) at 110°C, and subsequent thermal treatment with following parameters: RT to 250 °C (1 min), 250 °C to 450 °C (90 min), 3 h at 450 °C.*

The Raman spectrum (**Figure 4.10**) shows three strong characteristic absorptions at 639, 513 and 399 cm^{-1}, corresponding to the anatase phase, consistent with the observed photocatalytic activity.

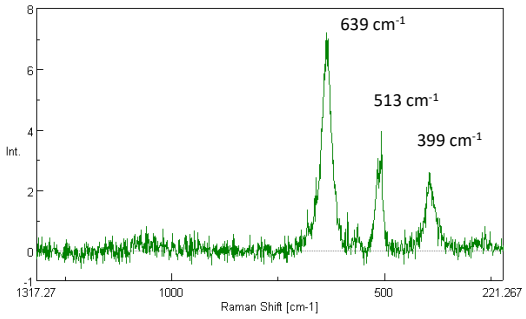

***Figure 4.10**: Raman spectra of a coated glass fabricated from an MLD thin film ($TiCl_4$/EG). Absorption bands: 639, 513, 399 cm^{-1}.*

The limited photocatalytic activity of this coated glass is probably a consequence of the lack of porosity. To find the best conditions to prepare porous TiO_2 anatase thin films on glass by MLD, we have investigated the influence of increasing i) the EG temperature from 70 °C to 80 °C to increase the vapor pressure, ii) the EG pulse time from 1 s to 1.5 s to provide more precursor to the reactor, iii) the maximum temperature of the heating ramp from 450 °C to 550 °C during annealing, and iv) the hold time at the maximum temperature during annealing (450 °C) for 5 h, both for improving the crystallinity.

As can be seen in **Figure 4.11**, no photocatalytic improvement is achieved when the temperature of EG is increased.

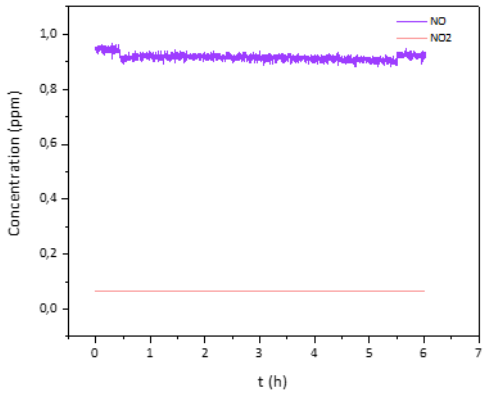

***Figure 4.11**: Photocatalytic activity of a glass with an organic-inorganic coating deposited using $TiCl_4$ and EG (80°C) at 110°C. Thermal treatment: RT to 250 °C (1 min), 250 °C to 450 °C (90 min), 3 h at 450 °C.*

Increasing the EG pulse time to 1.5 s leads to a slight initial improvement in the photocatalytic activity, as shown in **Figure 4.12**. However, after 2 hours, the average reduction in NO(g) concentration remains at 0.04 ppm, the same value observed when using a pulse time of 1.0 s (**Figure 4.5**).

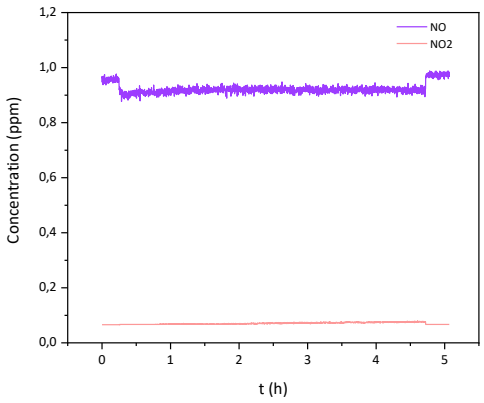

***Figure 4.12**: Photocatalytic activity of a glass with an organic-inorganic film deposited using $TiCl_4$ and EG 1.5s at 110°C. Thermal treatment: RT to 250 °C (1 min), 250 °C to 450 °C (90 min), 3 h at 450 °C.*

Increasing the maximum annealing temperature to 550°C had a negative effect on the photocatalytic activity **(Figure 4.13**). Although initially the glass shows stronger activity, with a reduction of the NO(g) concentration to 0.08 ppm and the formation of 0.01 ppm of NO_2, the photocatalytic activity is lost after 2 hours.

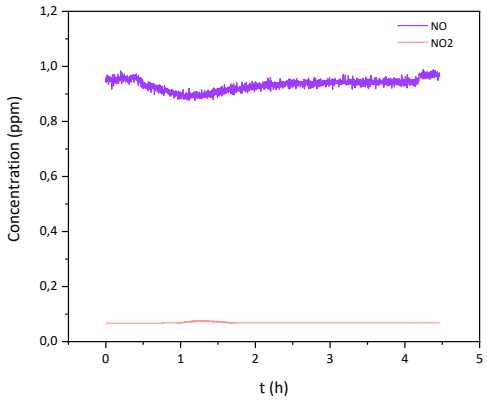

***Figure 4.13**: Photocatalytic activity of a glass with an organic-inorganic film deposited using $TiCl_4$ and EG (1.5s 80°C) at 110°C. Thermal treatment: RT to 250 °C (1 min), 250 °C to 450 °C (90 min), 3 h at 550 °C.*

Finally, as shown in **Figure 4.14**, increasing the hold time at the maximum temperature (450°C) from 3 to 5 hours has a similar effect. Although initially the concentration of NO(g) was reduced to 0.93 ppm, the photocatalytic activity decreases progressively in the course of the experiment.

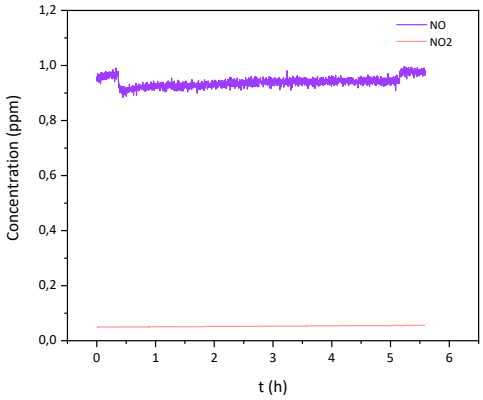

***Figure 4.14**: Photocatalytic activity of a glass with an organic-inorganic film deposited using $TiCl_4$ and EG (1.5s 80°C) at 110°C. Thermal treatment: RT to 250 °C (1 min), 250 °C to 450 °C (90 min), 5 h at 450 °C.*

Among the four strategies followed, only increasing the EG pulse had a positive effect. Therefore, two additional coated glasses were prepared to maximize EG transfer to the substrate. In the first one, the EG pulse time was increased to 4.0 and using the optimized annealing treatment. The first of the coated glasses showed an initial decrease in NO(g) concentration to 0.89 ppm and NO_2(g) formation of 0.02 ppm, although the photocatalytic activity decays with time and stabilizes at 0.97 ppm of NO(g) after 2 h (**Figure 4.15**).

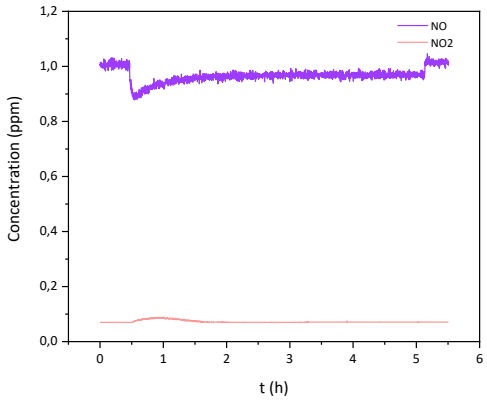

***Figure 4.15**: Photocatalytic activity of a glass with an organic-inorganic film deposited using $TiCl_4$ and EG (4s 80°C) at 110°C. Thermal treatment: RT to 250 °C (1 min), 250 °C to 450 °C (90 min), 3 h at 450 °C.*

In the second sample, two consecutive EG pulses of 4.0 s each were used. Surprisingly, the second coated-glass showed no photocatalytic activity (**Figure 4.16**).

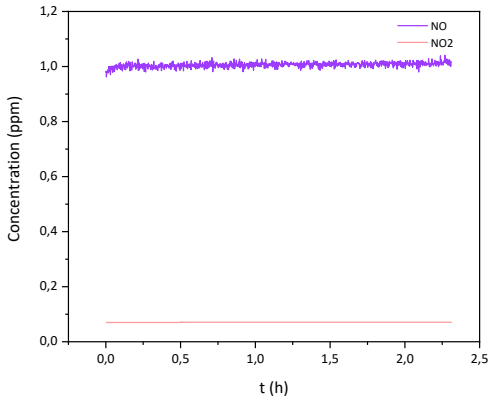

***Figure 4.16**: Photocatalytic activity of a glass with an organic-inorganic film deposited using $TiCl_4$ and EG (2x4s) at 110°C. Thermal treatment: RT to 250 °C (1 min), 250 °C to 450 °C (90 min), 3 h at 450 °C.*

Unfortunately, no significant increase in photocatalytic activity was observed in any of the cases. Therefore, other organic molecules were tested instead of EG. Klepper and co-workers have described the preparation of alucones, inorganic-organic hybrid films based on trimethylaluminum (TMA). A range of aromatic and aliphatic dicarboxylic acids have been used for the preparation of alucone coatings on soda-lime glass and silicon single crystals.[119,120] An analogous inorganic-organic hybrid thin film was prepared using $TiCl_4$ and terephthalic acid (benzene-1,4-dicarboxylic acid); however, a thickness greater than 6 nm could not be achieved due to equipment limitations. As a result, these films did not exhibit photocatalytic activity in the degradation of NO(g).

4.3.3 Photocatalytic coatings on glass from hybrid inorganic-organic superlattice thin films.

Recently, Knez and co-workers have described the reaction of TMA with hydroquinone (HQ) as an organic substrate.[121] According to this study, the preparation of inorganic-organic hybrid coatings using $TiCl_4$ and hydroquinone (HQ) could be achievable. The methodology reported by Karppinen and co-workers, who developed a combined ALD/MLD deposition strategy to prepare inorganic-organic thin films using $TiCl_4$, H_2O and HQ as precursors, was used. [122] Here, the combination of hybrid $(Ti–O–C_6H_4–O–)_k$, prepared by $TiCl_4$/HQ, with TiO_2 layers, prepared by $TiCl_4/H_2O$, result in the formation of $[(TiO_2)_m(Ti\text{-}O\text{-}C_6H_4\text{-}O\text{-})_k]_n$ coatings which are composed of layers of amorphous TiO_2 linked to HQ (**Figure 4.17**). Thermal annealing should result in the formation of a porous TiO_2 coating after removal of the HQ template.

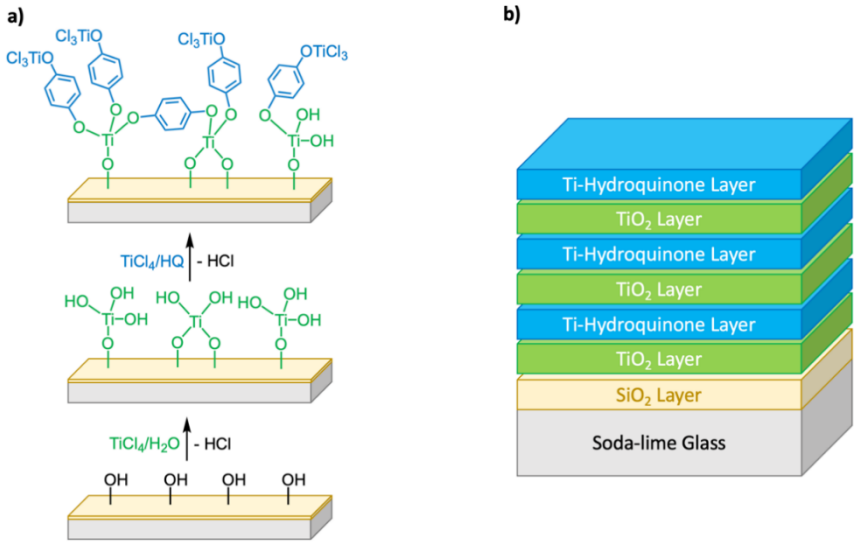

***Figure 4.17**: Schematic representation of the deposition of inorganic-organic thin films on glass. The coating is composed of TiO_2 layers (prepared by $TiCl_4/H_2O$ ALD) and hybrid Ti/HQ layers (prepared by $TiCl_4$/HQ MLD): a) Sequential deposition of single cycle ALD/MLD layers, b) sequential deposition of TiO_2 and Ti-HQ layers generated by multiple ALD and MLD cycles, respectively.*

The first coating was prepared in two steps. Initially, $TiCl_4$ and H_2O were pulsed according to the following sequence $TiCl_4$ (0.2 s)/N_2 (60 s)/H_2O (0.2 s)/N_2 (65 s), 20 cycles, to deposit a TiO_2 layer. Subsequently, a layer of the hybrid film was deposited using $TiCl_4$ and HQ following the pulse sequence $TiCl_4$ (0.2 s)/N_2 (60 s)/HQ (12 s)/N_2 (80 s), 500 cycles. The resulting coating had a thickness of 85 nm, which was reduced to about 25 nm (XRR) after the optimized annealing treatment. The obtained coated glass was transparent and showed a uniform coating. However, it showed almost no photocatalytic activity (**Figure 4.18**).

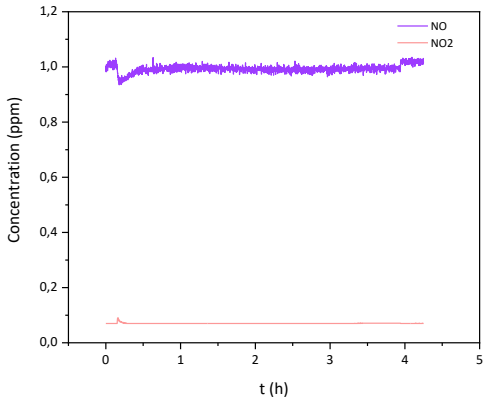

***Figure 4.18**: Photocatalytic activity of a glass coated with an inorganic film (TiO_2) and an inorganic-organic layer ($TiCl_4$/HQ). Thermal treatment: RT to 250 °C (1 min), 250 °C to 450 °C (90 min), 3 h at 450 °C.*

In view of this result, it was decided to explore a more homogeneous alternating deposition sequence maintaining the pulse sequence. First, $TiCl_4/H_2O$ were used as precursors (2 cycles) and subsequently $TiCl_4$/HQ (4 cycles). This sequence was repeated 120 times to obtain a multilayer structure (**Figure 4.17**).

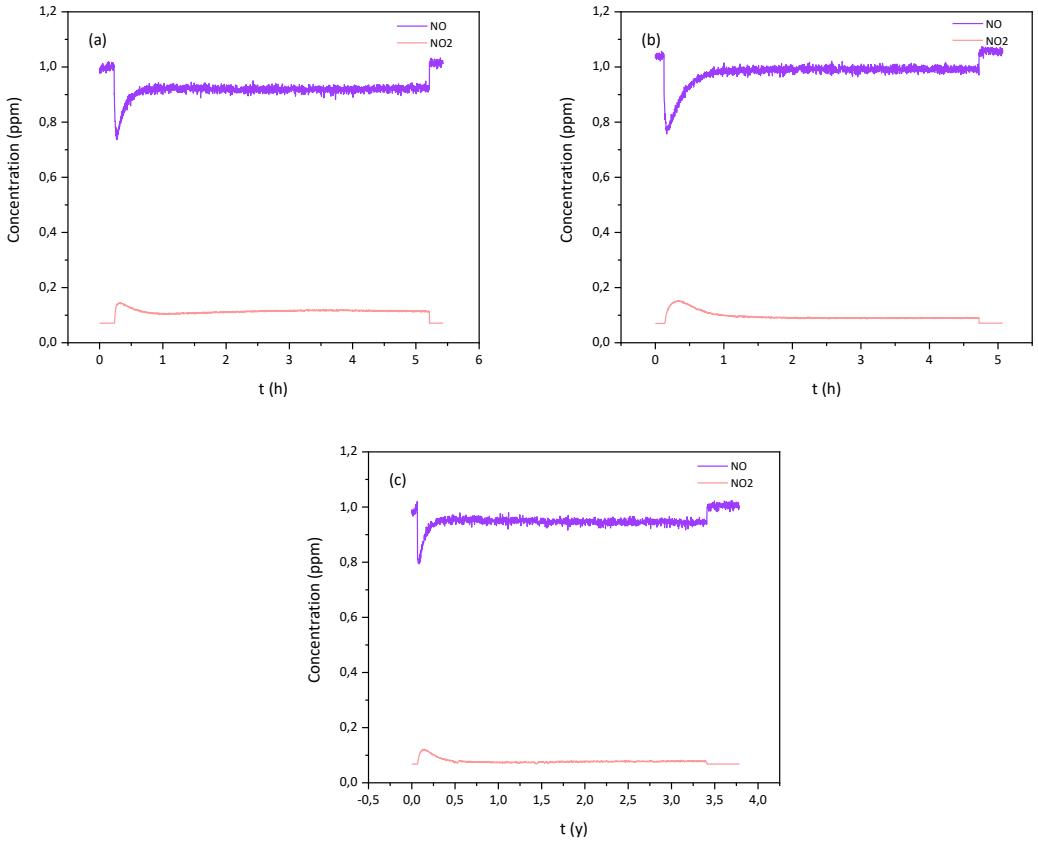

***Figure 4.19**: Photocatalytic degradation of NO(g) by the coated glasses formed by alternating inorganic (TiO_2) and inorganic-organic ($TiCl_4$/HQ) layers after optimized thermal treatment: a) layers deposited at 2/4 ratio (120 cycles), b) Photocatalytic activity of the same sample in the second and (c) third photocatalytic measurement.*

The coated glass was also transparent and showed a uniform coating over the entire surface after the optimized annealing treatment. However, in contrast to the previous sample the film thickness after the thermal treatment increased to nearly double its original thickness, which could be indicative of increased porosity induction. The thus fabricated transparent coated glass showed photocatalytic activity. **Figure 4.19** shows an initial decrease in NO(g) concentration to 0.75 ppm and NO_2(g) formation to 0.07 ppm and afterwards the photocatalytic activity stabilizes at 0.90 ppm of NO(g) and 0.04 ppm of NO_2(g) over the remaining 4 h of the experiment duration. The coated glass was subjected to successive photocatalytic measurements by washing several times with distilled water and dried on absorbent paper after each measurement. Although the photocatalytic activity is maintained in the second photocatalytic measurement, a slight decrease was observed in the third measurement.

The Raman spectrum (**Figure 4.20**) showed three strong characteristic absorptions at 639, 513 and 399 cm^{-1} corresponding to the anatase phase, which is consistent with the observed photocatalytic activity.

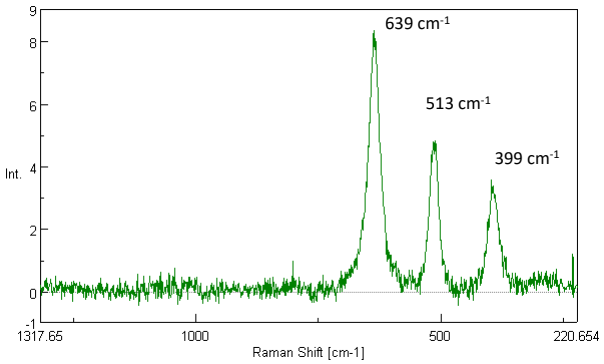

***Figure 4.20**: Raman spectra of a coated glass formed by alternating inorganic (TiO_2) and inorganic-organic ($TiCl_4$/HQ) layers after optimized thermal treatment. Absorption bands: 639, 513, 399 cm^{-1}*

After this successful experiment, we decided to explore a similar alternating deposition sequence increasing the number of $TiCl_4$/HQ cycles. Alternating layers of inorganic (TiO_2) and hybrid (Ti/HQ) films have been deposited using $TiCl_4/H_2O$ (2 cycles) and $TiCl_4$/HQ (8 cycles) as precursors, repeating this sequence 120 times, under the conditions specified above. The coated glass, fabricated after annealing under standard conditions, showed higher photocatalytic activity. Initially, the amount of NO(g) decreased to 0.64 ppm and stabilized at 0.85 ppm NO(g) and 0.08 ppm NO_2(g) during the experiment (**Figure 4.21**). The pronounced decrease in NO(g) concentration at the beginning of the experiment in comparison to the previous glass is indicative of increased coating porosity, which is consistent with the improved photocatalytic

activity. It should be noted that this coated glass showed stable photocatalytic behavior, since the activity is preserved in successive photocatalytic measurements. The NO(g) concentration stabilizes at 0.87 ppm with NO_2(g) formation of 0.07 ppm along the second and third photocatalytic measurements.

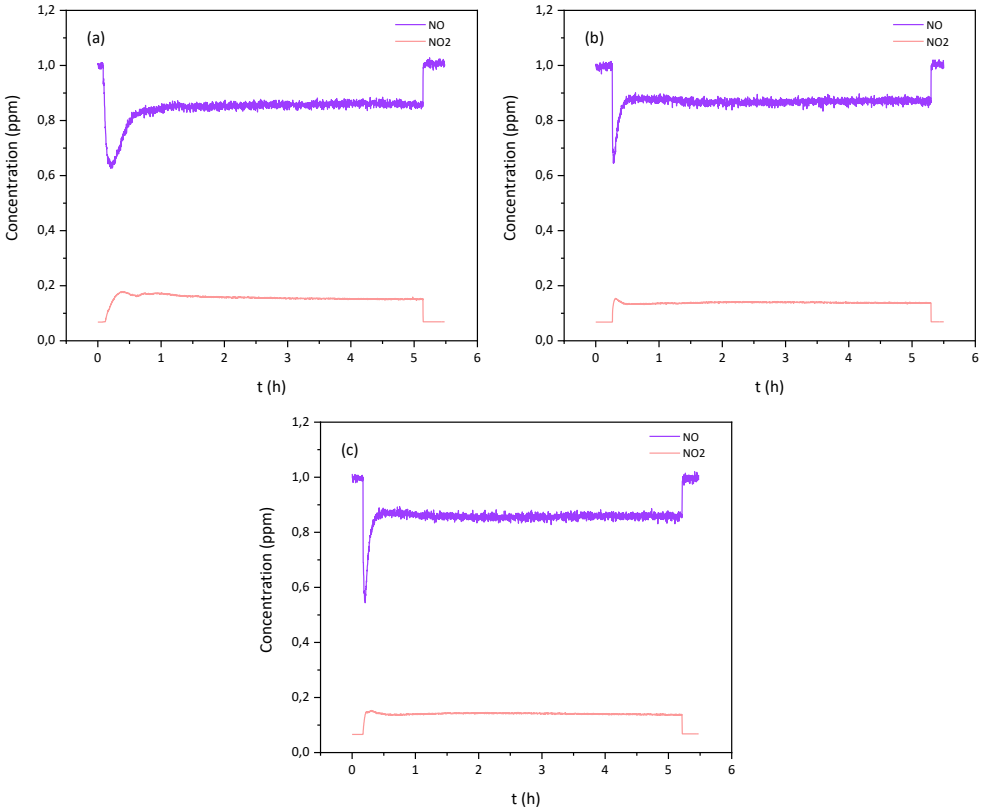

***Figure 4.21**: Photocatalytic degradation of NO(g) with coated glasses formed by alternating inorganic (TiO_2) and inorganic-organic ($TiCl_4$/HQ) layers after optimized thermal treatment: a) layers deposited at 2/8 ratio (120 cycles), b) Photocatalytic activity in the second (c) and third photocatalytic measurement (c).*

SEM images of the coated glass samples exhibiting the best photocatalytic performance (**Figure 4.21**) are shown in **Figure 4.22**. Top-view SEM images show a granular structure (grain sizes ≈ 30-150 nm) with smaller features resulting in a porous structure with an average pore size of 3-4 nm (min. 0.8 nm, max. 13 nm).

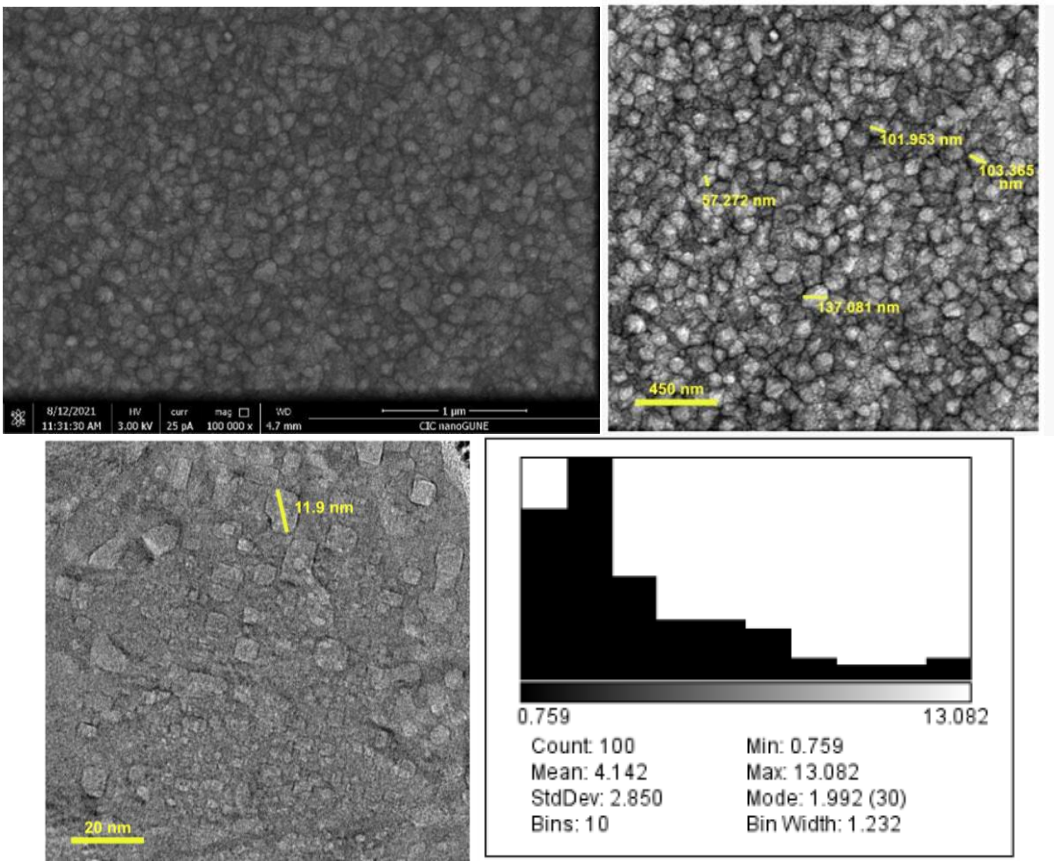

***Figure 4.22**: SEM images of a coated glass fabricated from an inorganic-organic thin film composed of TiO_2 layers (prepared by $TiCl_4$/H2O ALD) and hybrid Ti/HQ layers (prepared by $TiCl_4$/HQ MLD) (2:8 pulse sequence) after annealing under optimized conditions.*

Low magnification cross-sectional TEM images (**Figure 4.23a**) show a film thickness of about ≈ 180 nm and evidence grains elongated along the thickness of the film. TEM images at higher magnification (**Figure 4.23b**) reveal two distinct regions in the film: a dense zone (≈ 45 nm) was observed at the bottom (near the substrate) and a less dense zone at the top (≈ 125 nm). A thin layer of SiO_2 (≈ 10nm) is observed below the deposited film.

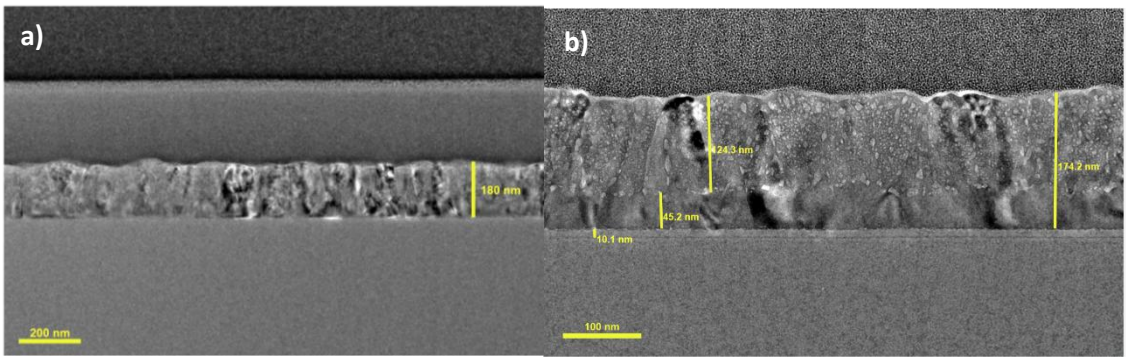

***Figure 4.23**: TEM images of a coated glass with a thin film composed of TiO_2 layers (prepared by $TiCl_4$/H_2O ALD) and hybrid Ti/HQ layers (prepared by $TiCl_4$/HQ MLD) (2:8 pulse sequence) after annealing under optimized conditions. Low magnification cross-sectional TEM images (a) and high magnification TEM images (b).*

EDX analysis confirms that the composition of the coating is compatible with TiO_2 layer (Figure **4.24**).

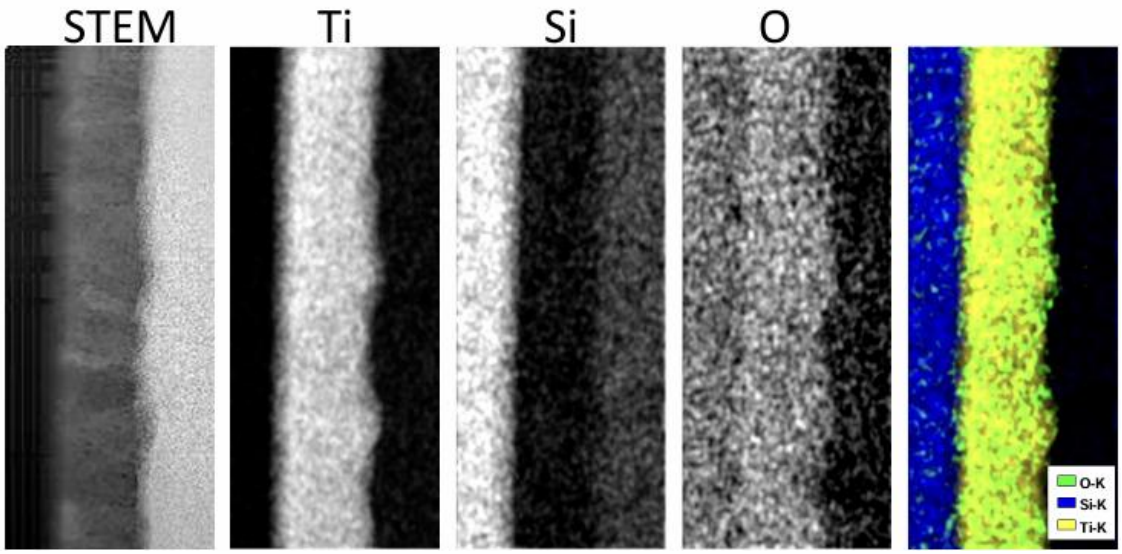

***Figure 4.24**: EDX analysis of a coated glass with a thin film composed of TiO_2 layers (prepared by $TiCl_4/H_2O$ ALD) and hybrid Ti/HQ layers (prepared by $TiCl_4$/HQ MLD) (2:8 pulse sequence) after annealing under optimized conditions.*

The highly porous TiO_2 layer on top of the coating accounts for the observed photocatalytic activity. However, the appearance of a dense non-porous TiO_2 layer at the bottom of the coating was completely unexpected. The formation of the dense bottom layer could be related to compressive stress exerted by the overlying porous TiO_2, potentially inducing densification during the thermal treatment. To rule out incomplete removal of the hydroquinone template, we fabricated coated glass under the same deposition conditions, but with increasing the hold time at the maximum temperature in the thermal treatment from 3 to 5 hours. However, this coated glass showed significantly lower photocatalytic activity (**Figure 4.25**).

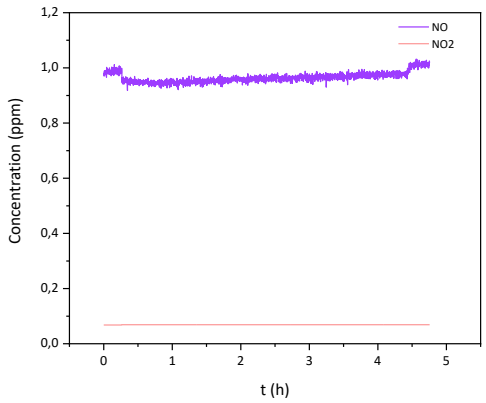

***Figure 4.25**: Photocatalytic activity of a coated glass with alternating inorganic (TiO_2) and inorganic-organic ($TiCl_4$/HQ) layers in a ratio 2/8. Thermal treatment: RT to 250 °C (1 min), 250 °C to 450 °C (90 min), 5 h at 450 °C.*

Finally, we explored the effect of increasing the number of the $TiCl_4/H_2O$ cycles vs $TiCl_4$/HQ in the composite. A deposition sequence of $TiCl_4/H_2O$ (4 cycles) and $TiCl_4$/HQ (2 cycles) was applied and repeated 120 times. The coated glass prepared under these conditions showed very little photocatalytic activity with a NO(g) concentration stabilization at 0.98 ppm throughout the experiment (**Figure 4.26**). Therefore, increasing the thickness of the inorganic TiO_2 layer has a negative impact on the photocatalytic activity, which confirms the important role of hydroquinone for the generation of porous structures.

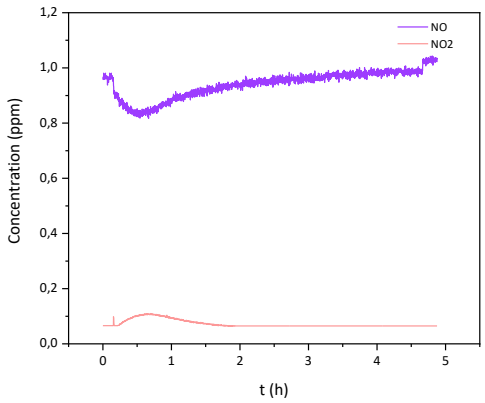

***Figure 4.26**: Photocatalytic activity of a coated glasses with alternating inorganic (TiO_2) and inorganic-organic ($TiCl_4$/HQ) layers in a ratio 4/2. Thermal treatment: RT to 250 °C (1 min), 250 °C to 450 °C (90 min), 3 h at 450 °C.*

The photocatalytic performance of the coatings is strongly influenced by the deposition sequence, layer thickness, and the porosity induced by the hydroquinone (HQ) template. The first coating, consisting of a thick TiO_2 layer followed by a hybrid Ti/HQ layer, was uniform and transparent but showed almost no activity; after annealing, its thickness decreased from 85 nm to 25 nm, indicating densification and the formation of a compact, non-porous structure that limited access to active sites. In contrast, alternating 2 cycles of $TiCl_4/H_2O$ with 4 cycles of $TiCl_4$/HQ repeated 120 times produced a multilayer whose thickness nearly doubled after annealing, reflecting the development of porosity and moderate photocatalytic activity with partial NO(g) conversion and characteristic anatase crystallinity. Increasing the number of Ti/HQ cycles to 8 (2/8 cycles) further enhanced activity and stability. SEM and TEM revealed a porous top layer (~125 nm) over a denser bottom layer (~45 nm), indicating that the combination of porosity and structural support is key for photocatalytic efficiency. Extended annealing reduced activity, confirming the importance of preserving the porous architecture. In contrast, increasing the proportion of $TiCl_4/H_2O$ (4/2 cycles) produced coatings with very low activity, indicating that a thicker inorganic layer suppresses porosity and the formation of accessible anatase surfaces, thereby confirming the essential role of HQ in generating functional porous structures.

Table 4.1 presents a summary of the photocatalytic effects observed for all prepared samples. The table highlights the different samples and their corresponding photocatalytic behavior, indicating whether each sample exhibited a photocatalytic effect, an improvement, or no significant change.

***Table 4.1**: Summary of photocatalytic effects for all prepared samples.*

Nº	SAMPLE	EFFECT ON PHOTOCATALYSIS
1	$TiCl_4$/Water	No photocatalytic effect
2	$TiCl_4$/EG 1s pulse	Photocatalytic effect
3	$TiCl_4$/GL	No photocatalytic effect
4	$TiCl_4$/EG with Temperature ramp	Improvement
5	$TiCl_4$/EG Increase T of EG	No improvement
6	$TiCl_4$/EG 1.5s pulse	Improvement
7	$TiCl_4$/EG 1.5s pulse. Higher annealing T	No improvement
8	$TiCl_4$/EG 1.5s pulse. Higher annealing time	No improvement
9	$TiCl_4$/EG 4s pulse	No improvement
10	$TiCl_4$/EG 4s pulse + EG 4s pulse	No photocatalytic effect
11	TiO2 + Ti-HQ	No photocatalytic effect
12	Ti/HQ 2/4	Improvement
13	**Ti/HQ 2/8**	**Best photocatalytic effect**
14	Ti/HQ 4/2	No improvement

4.4 CONCLUSIONS

We have developed a convenient ALD/MLD methodology for the deposition of porous TiO_2-coatings on soda-lime glass that show activity in the photocatalytic oxidation of nitrogen oxide. Initially, we studied the deposition of hybrid inorganic-organic coatings using $TiCl_4$ and EG by MLD, which leads to a maximum NO removal of 4% over 4h. A study of the annealing process on these samples reveals that long thermal treatments result in the loss of catalytic activity, likely due to the collapse of the porous structure. Subsequently, we explored the preparation of TiO_2-coatings by the deposition of inorganic-organic superlattice thin films. The best performing coating was prepared by deposition of a TiO_2 layer by pulsing $TiCl_4/H_2O$ (2 cycles), followed by a hybrid film using $TiCl_4$ and HQ (8 cycles), and repeating this sequence 120 times. The resulting

material was able to reduce the NO concentration by ca. 15% in three successive photocatalytic measurements of 5 h duration each. The TEM and SEM images of this TiO_2-coating show two regions, a porous columnar structure on top, and a denser region immediately above the thin barrier layer of SiO_2 deposited by PVD. EDX analysis and Raman spectroscopy confirm the presence of the anatase phase, which, together with the porosity of the material, account for the observed photocatalytic activity.

Chapter 5 VALIDATION OF THE ALD PROTOTYPE WITH A VERSATILE ADJUSTABLE VOLUME CHAMBER.

5.1 INTRODUCTION

This chapter details the validation process of an ALD reactor prototype with a versatile chamber that allows operation with three different volumes. The prototype was manufactured by Ctechnano, where I worked during the industrial internships of the thesis.

5.2 PROTOTYPE DESCRIPTION

The developed ALD prototype has an adaptable reactor that enables selection among three operational volumes. These volumes are adjusted through placement of separators into the chamber, allowing modifications to the internal chamber space according to the deposition process requirements. The three outlets are always pumping independent of the volume used. In **Figure 5.1**, the diagram of the chamber is shown. The heaters are located at the bottom of the chamber and in the lid to ensure the desired temperature and maintain its uniformity throughout the entire chamber.

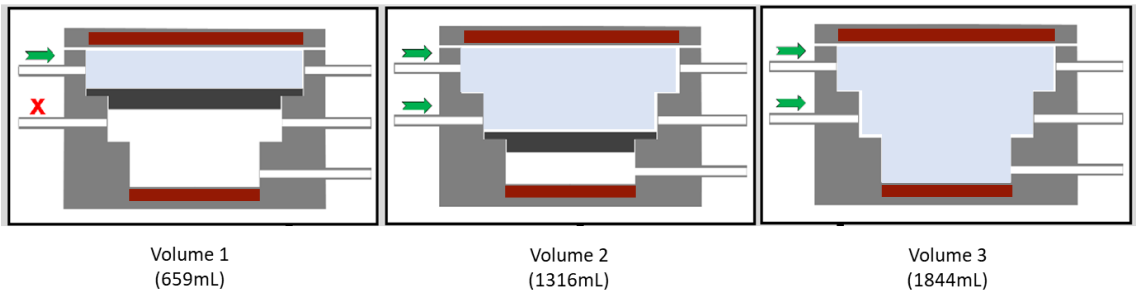

***Figure 5.1**: Diagram of the versatile chamber.*

5.3 EXPERIMENTAL SECTION

Experiments were conducted to validate the prototype's performance under each volume configuration. Deposition tests were carried out in all three volumes, evaluating different deposited materials (Al_2O_3 and ZnO) and process temperatures. Since the volume adjustment design poses a risk to the integrity of the polymeric seal upon heating of the reactor, a dedicated experiment was conducted to verify the feasibility of operating without the seal between

volumes. Five silicon wafer chips were placed in a cross pattern within the sample area (see **Figure 5.2**). Such tests were carried out in all three individual volumes. The validation process was done by measuring the thickness of the deposited layers with X-ray reflectivity.

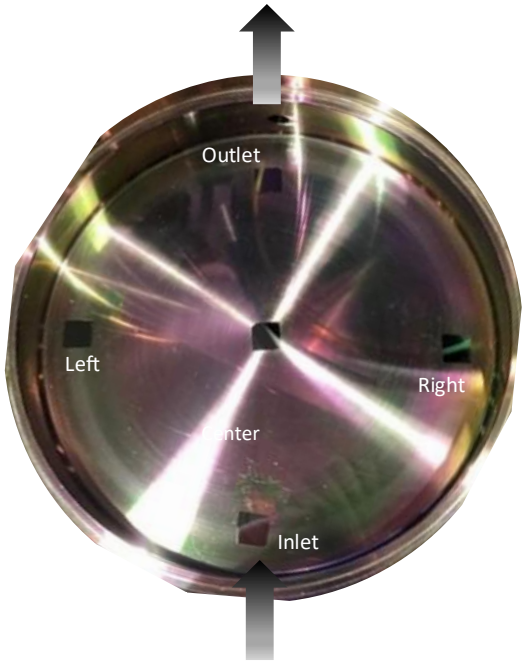

***Figure 5.2**: Distribution of the wafer chips in the chamber.*

Table 5.1 summarizes all the experiments conducted. Alumina films were deposited at 250°C using trimethylaluminum (TMA, Sigma-Aldrich 97%) and water as precursors. The tests were performed at 250°C in volume 1, both with and without an O-ring, in volume 2, and in volume 3. Zinc oxide films were deposited using diethylzinc (DEZ, Strem Chemicals 95%) and water as precursors. The process was tested with an O-ring at 150°C and 200°C in volume 1 and in volume 3.

The deposition parameters have been adjusted to meet the requirements of the different volumes. A larger volume requires a greater amount of precursor and a longer purge time.

Experimental parameters of each process are provided below the table.

***Table 5.1**: Resume of experiments.*

Test	Material	Volume	Temperature (°C)	O-ring
1	Al_2O_3	1	250	Yes
2	Al_2O_3	2	250	Yes
3	Al_2O_3	3	250	Yes
4	ZnO	1	150	Yes
5	ZnO	1	200	Yes
6	ZnO	3	150	Yes
7	ZnO	3	200	Yes
8	Al_2O_3	1	250	Yes
9	Al_2O_3	1	250	No

5.3.1 Al_2O_3 tests

For volume 1: The reactor was evacuated together with a concurrent N_2 gas purge at a flow rate of 20 sccm (10^{-1}mbar). The pulse sequence TMA(0.06 s)/N_2(32 s)/H_2O(0.06 s)/N_2(32 s) was applied for 500 cycles.

For Volume 2: The reactor was evacuated together with a concurrent N_2 gas purge at a flow rate of 100 sccm (10^{-1}mbar). The pulse sequence TMA(0.15 s)/N_2(40 s)/H_2O(0.15 s)/N_2(40 s) was applied for 150 cycles.

For Volume 3: The reactor was evacuated together with a concurrent N_2 gas purge at a flow rate of 100 sccm (1 mbar). The pulse sequence TMA(0.4 s)/N_2(50 s)/H_2O(0.4 s)/N_2(50 s) was applied for 500 cycles.

5.3.2 ZnO tests

5.3.2.1 Volume 1

The reactor was evacuated together with a concurrent N_2 gas purge at a flow rate of 20 sccm (10^{-1}mbar). The pulse sequence DEZ (0.05 s)/N_2(40 s)/H_2O(0.05 s)/N_2(40 s) was applied for 190 cycles at 150°C.

At 200°C, the pulse sequence changed to DEZ (0.05 s)/N_2(30 s)/H_2O(0.05 s)/N_2(30 s) was applied for 190 cycles.

5.3.2.2 Volume 3

The reactor was evacuated together with a concurrent N_2 gas purge at a flow rate of 100 sccm (1mbar). The pulse sequence DEZ (0.5 s)/N_2(70 s)/H_2O(0.5 s)/N_2(70 s) was applied for 200 cycles at 150°C.

At 200°C, the pulse sequence change to DEZ (0.4 s)/N_2(40 s)/H_2O(0.4 s)/N_2(40 s) was applied for 190 cycles.

5.3.3 O-ring tests

The same tests were carried out with and without the O-ring in volume 1. The reactor was evacuated together with a concurrent N_2 gas purge at a flow rate of 20 sccm (10^{-1}mbar). Alumina films were deposited according to the following pulse sequence TMA(0.06 s)/N_2(32 s)/H_2O(0.06 s)/N_2(32 s) for 500 cycles at 250°C.

5.4 RESULTS

5.4.1 Al_2O_3 results

Figure 5.3 illustrates the thickness of the Al_2O_3 layer on Si wafer pieces as a function of the position in the reactor using volume 1 (a), volume 2 (b), and volume 3 (c). The thickness values are comparable at all points in the chamber, demonstrating high reproducibility. In **Figure 5.3b**, deviations of 2 nm are observed at thicknesses below 20 nm, resulting in a relative error greater than 10%. This variability could be attributed to the incomplete optimization of the process, which led to a dispersion in the thickness values within the deposition chamber due to insufficient saturation or incomplete reaction.

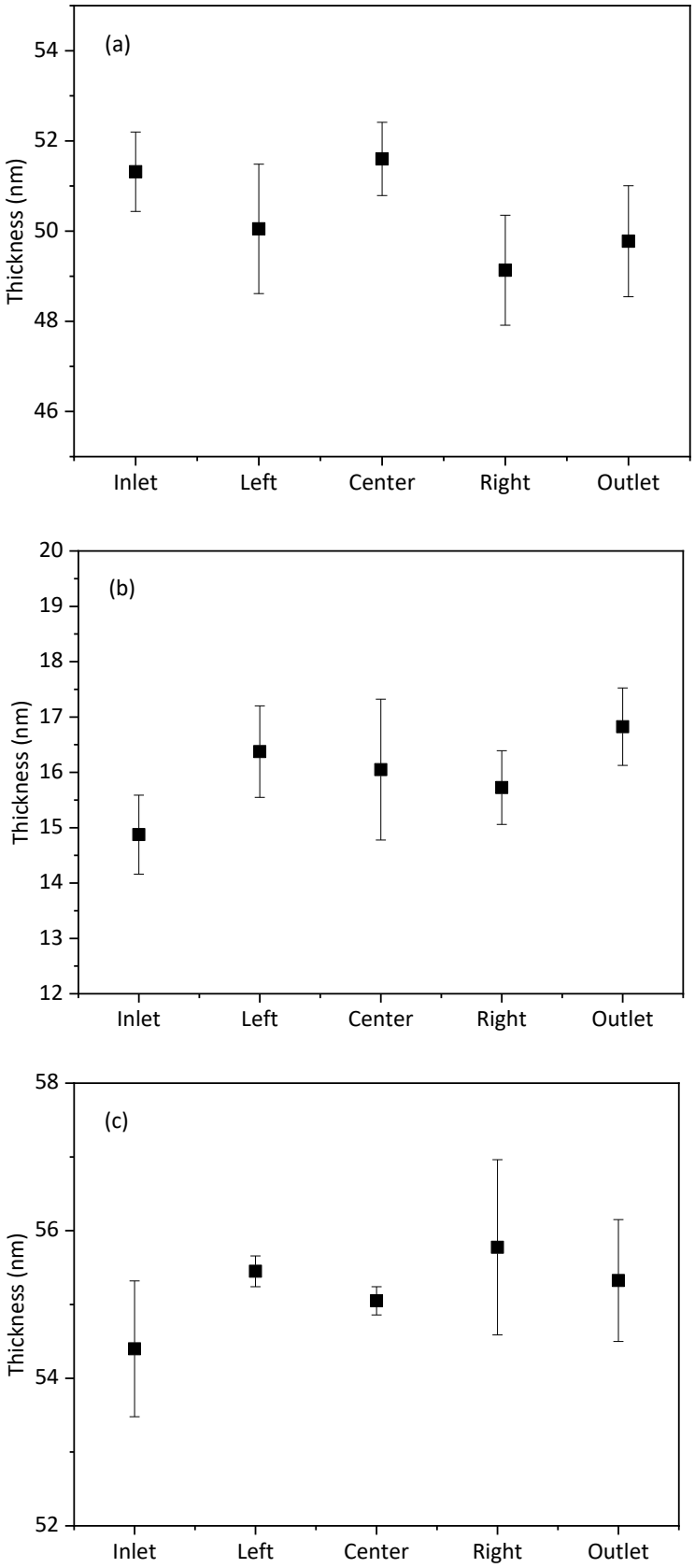

***Figure 5.3**: Thickness of Al_2O_3 after 500 ALD cycles at 250°C for volume 1 (a), volume 2 (b), and volume 3 (c). The error bars for the ALD films on silicon substrates represent multiple measurements taken from each wafer within the same experiment.*

Figure 5.4 presents the GPC for each position in the chamber, extracted from the thicknesses in **Figure 5.3** and the cycle numbers. These values also show high reproducibility throughout the chamber. The standard value reported by Cambridge Nanotech, a commercial supplier of ALD reactors (Supporting Information), for the Al_2O_3 ALD process is approximately 1.07 Å/cycle. The experimentally obtained values in our system, averaged from five points in each volume, are 1.01 Å/cycle, 1.06 Å/cycle, and 1.10 Å/cycle for Volume 1, Volume 2, and Volume 3, respectively, which are close to the standard value of 1.07 Å/cycle. This indicates that the ALD process of Al_2O_3 is generally reliable in the system. However, there are differences: the processes performed with Volume 1 and Volume 3 are more stable, while Volume 2 shows greater variability and larger error bars. This instability in Volume 2 is related to the lower number of cycles used for the deposition. As the number of ALD cycles increases, the overall film thickness also increases, which tends to reduce the relative error associated with measurement variability. In contrast, at lower cycle numbers—particularly in the case of ultra-thin films—the same absolute deviation can correspond to a substantially higher relative error.

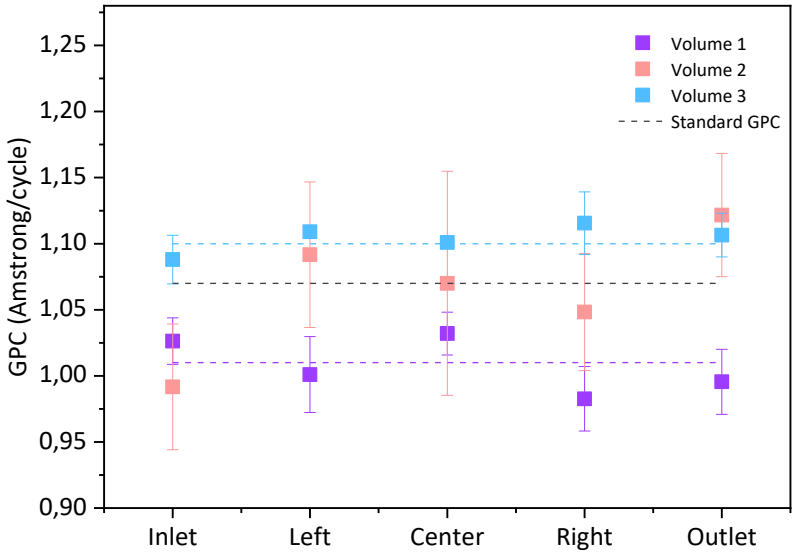

***Figure 5.4**: GPC of Al_2O_3 at 250°C for Volume 1 (purple), Volume 2 (coral), and Volume 3 (blue). The gray dotted line represents the standard GPC, the blue dotted line represents the experimental GPC for Volume 3, and the purple dotted line represents the experimental GPC for Volume 1. The error bars for the ALD films on silicon substrates represent multiple measurements taken from each wafer within the same experiment.*

5.4.2 ZnO results

Figure 5.5 shows the values of the thickness of the ZnO coating at different positions in volume 1 at 150°C (a) and 200°C (b). The variation is 1.7% at 150°C and 4% at 200°C across the deposition area and with this within the range of expected deviations.

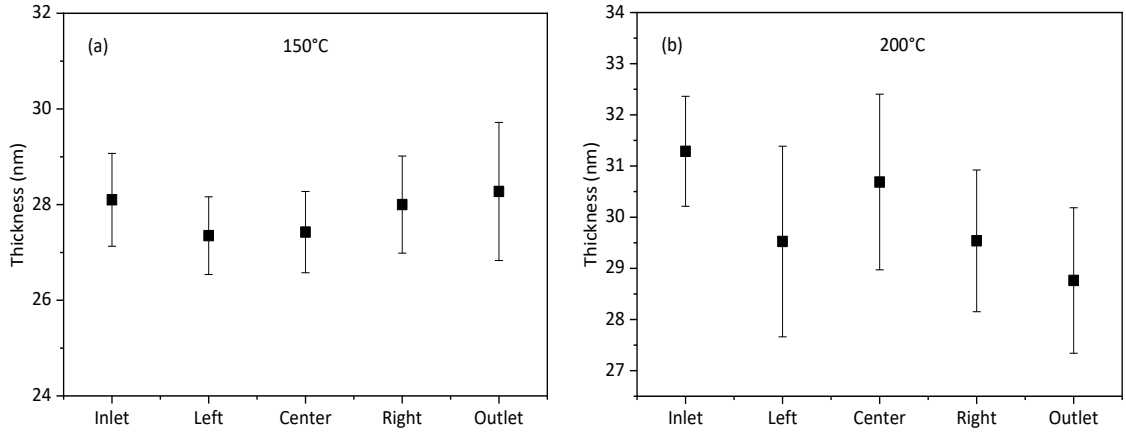

***Figure 5.5**: Thickness values of the ZnO layer at various positions, grown in volume 1 at 150°C (a) and 200°C (b). The error bars for the ALD films on silicon substrates represent multiple measurements taken from each wafer within the same experiment.*

Figure 5.6 compares the values of the thickness of the ZnO layer, deposited in volume 3 at 150°C (a) and 200°C (b). The variation is 2.7% at 150°C and 1.7% at 200°C across the deposition area and with this within the range of expected deviations.

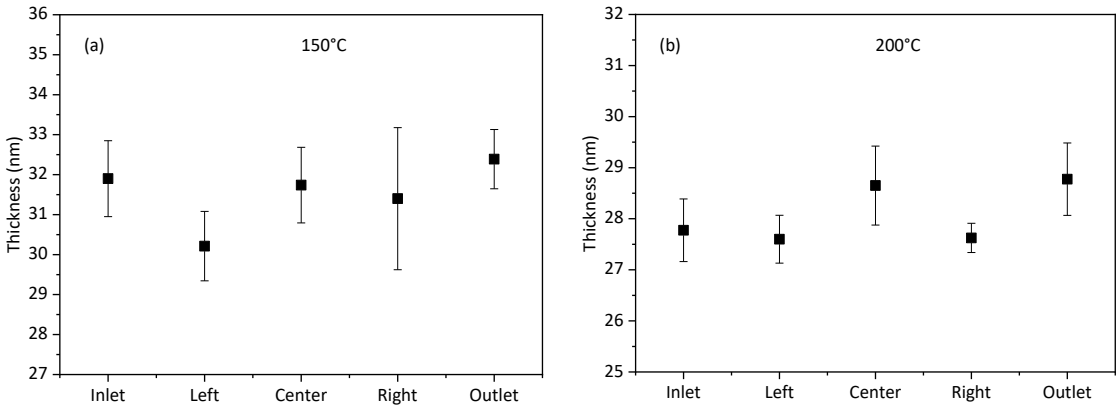

***Figure 5.6**: Thickness values of the ZnO layers at various positions, grown in volume 3 at 150°C (a) and 200°C (b). The error bars for the ALD films on silicon substrates represent multiple measurements taken from each wafer within the same experiment.*

Figure 5.7 shows the GPC values of the ZnO ALD process in volume 3 at 150°C (a) and 200°C (b). The growth values remain uniform at all points in the chamber, demonstrating high reproducibility. The value reported by Cambridge Nanotech for the ZnO ALD process at 150°C is 1.66 Å/cycle, and at 200°C it is 1.46 Å/cycle. For comparison, the experimentally obtained values in our reactor at 150°C process temperature are 1.47 Å/cycle in volume 1 and 1.6 Å/cycle in volume 3. At 200°C, the experimental values are 1.57 Å/cycle in volume 1 and 1.47 Å/cycle in volume 3. Thus, the values are close to the values reported by Cambridge Nanotech (Supporting information).

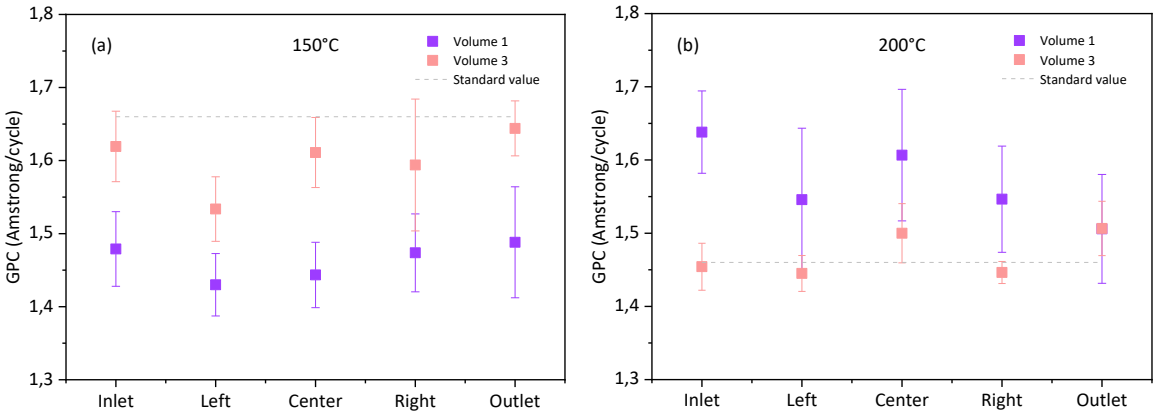

***Figure 5.7**: GPC values for ZnO ALD process at 150°C (a) and 200°C (b). The error bars for the ALD films on silicon substrates represent multiple measurements taken from each wafer within the same experiment.*

At 150°C, both volumes show GPCs below the reference line, while at 200°C, the opposite occurs. Additionally, at 150°C, the GPC in Volume 1 is lower than in Volume 3, but at 200°C, it becomes inverted. While the GPC in Volume 3 remains close to the reference line in both cases, the one in Volume 1 shows greater variation. At 150°C, the values are slightly lower than the reported ones, while at 200°C, they align more closely, with small differences between volumes. Overall, these results indicate that the process in Volume 3 is more stable than in Volume 1 and confirm the reliability of the ZnO ALD process across different volumes and temperatures.

Although the average thickness values obtained are reasonable, some variation in coating uniformity was observed, especially in thinner films, where small absolute deviations result in relatively high errors (over 10% in some cases). This contrasts with the uniformity levels typically achieved in commercial ALD systems, where deviations are usually below 1% across the full wafer.

It's important to note that these measurements were carried out using a prototype ALD chamber that has not yet been fully optimized. This likely explains part of the variation, as key process parameters like gas flow, precursor dosing, and purge times still require fine-tuning.

To improve uniformity, further optimization of these parameters is recommended. Additionally, performing simulations, such as computational fluid dynamics (CFD), could help better understand the gas distribution inside the reactor. This would make it possible to identify problematic areas and improve precursor delivery, which is essential for achieving more homogeneous and reproducible coatings.

5.4.3 O-ring tests

Figure 5.8 shows the thickness of the Al_2O_3 coating on the 5 chips, processed in the chamber sealed with an O-ring (a) and without an O-ring (b). The values from both experiments are comparable.

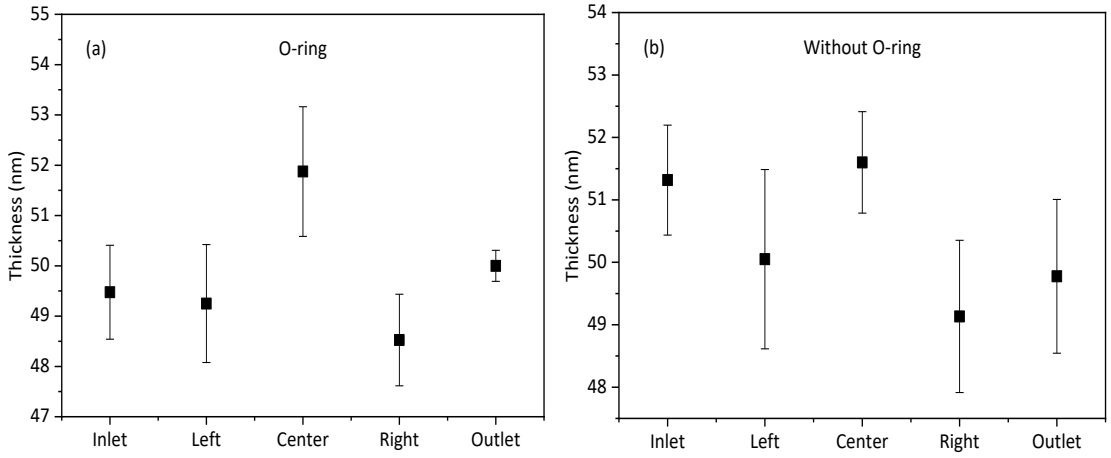

***Figure 5.8**: Thickness of Al_2O_3 at different chamber positions after 500 ALD cycles, deposited at 250°C with (a) and without (b) the O-ring. The error bars for the ALD films on silicon substrates represent multiple measurements taken from each wafer within the same experiment.*

The GPC of the processes is shown in **Figure 5.9**. The experimentally obtained value after the process with the O-ring is 1.00 Å/cycle and without it 1.01 Å/cycle. Both values are slightly lower than the reference value of Cambridge Nanotech. The tests conducted with and without the O-ring confirm that its presence in the equipment is not necessary.

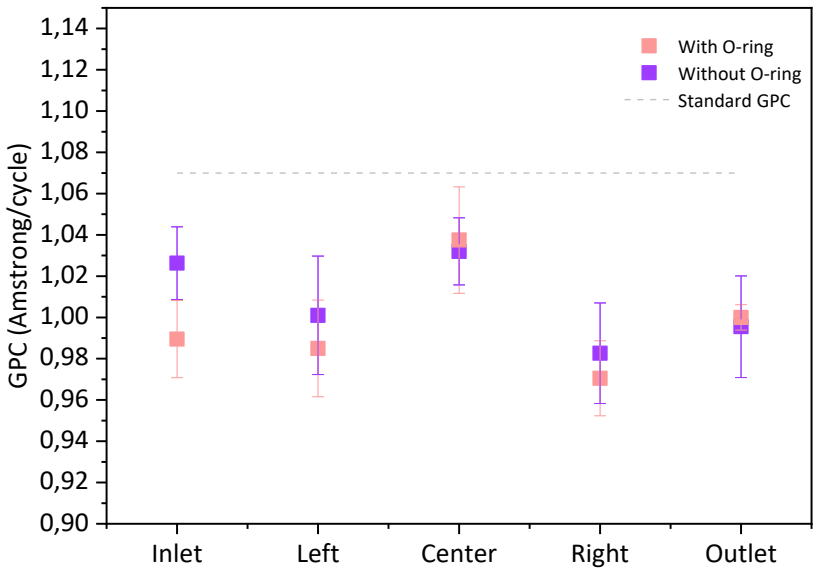

***Figure 5.9**: GPC of the Al_2O_3 processes at 250°C with (coral) and without (purple) the O-ring. The grey dotted line represents the standard GPC. The error bars for the ALD films on silicon substrates represent multiple measurements taken from each wafer within the same experiment.*

5.5 CONCLUSIONS

The thickness values for the Al_2O_3 layer across all reactor volumes (1, 2, and 3) show good reproducibility, with consistent values across different points in the chamber, indicating uniform deposition. The GPC values for Al_2O_3 are close to the reference values reported by Cambridge Nanotech (1.07 Å/cycle), with experimental values of 1.01 Å/cycle for volume 1, 1.06 Å/cycle for volume 2, and 1.10 Å/cycle for volume 3. This suggests that the ALD process for Al_2O_3 is functioning well and can be reliably used in each volume.

The thickness variations for ZnO deposition at 150°C and 200°C across the deposition area are within acceptable limits, with a variation of 2% at 150°C and 4% at 200°C at different points in volume 1. Similar trends are seen in volume 3, indicating good uniformity. The GPC values for the ZnO process show excellent reproducibility, with values of 1.47 Å/cycle in volume 1 and 1.6 Å/cycle in volume 3 at 150°C, and 1.57 Å/cycle in volume 1 and 1.47 Å/cycle in volume 3 at 200°C. These values are close to the reference values reported by Cambridge Nanotech, further confirming the reliability of the ZnO ALD process across different volumes and temperatures.

The thickness and GPC values for the Al_2O_3 coating in experiments conducted with and without the O-ring are well comparable. The values from both tests show a marginal difference of 0.01 Å/cycle in GPC. This suggests that the presence of the O-ring in the chamber does not significantly impact the coating process, and its absence does not alter the overall quality of the deposition. Therefore, the use of the O-ring is not essential for the process to perform reliably.

Overall, the results indicate that both Al_2O_3 and ZnO ALD processes are highly reproducible and reliable across the different volumes of the reactor, at the tested temperatures, with or without the O-ring.

Chapter 6 INDUSTRIAL COLLABORATION

As part of the development of this thesis, I had the opportunity to collaborate directly with Ctechnano Coating Technologies S.L. in an industrial setting. My work included carrying out client services, collaborating on various projects and providing technical services.

Some details of the work described in this chapter cannot be disclosed as they contain proprietary and confidential information with intellectual property (IP) owned by the customers. We have provided as much as possible relevant data while ensuring compliance with confidentiality requirements.

6.1 CLIENT SERVICES

Table 6.1 shows a summary of the services performed at Ctechnano, detailing the different deposited materials and their respective applications.

Table 6.1: Summary of client services in the company.

Material	Application
Al_2O_3	Electronic devices Jewellery Semiconductors Photonics Cultural heritage
TiO_2	Photonics
SiO_2	Semiconductors Photonics
HfO_2	Electronic devices
FeO_x	Photonics
Alumina-doped zinc oxide (AZO)	Jewellery Plastics
HfO_2/Al_2O_3 bilayers	Electronic devices
Al_2O_3/TiO_2 bilayers	Jewellery
HfO_2/SiO_2 bilayer	Optics
Al_2O_3 coating with a Terminal Organic Layer	Hydrophobicity Textile

6.2 INNOVATION PROJECTS

Apart from services, I was involved in some investigative projects, carried out in collaboration with other institutions:

6.2.1 Functionalization and modification of delignified wood through Vapor Phase Infiltration (VPI).

The objective of this project was to develop an alternative for the manufacturing of transparent wood, which could be used in construction as a substitute for glass. Wood in its natural state is not transparent, primarily due to the presence of lignin, which scatters light. Once the lignin is removed, the wood loses part of its opacity. Furthermore, the removal of air inside the structure of the delignified wood facilitates the transmission of light. Methods for manufacturing transparent wood have been studied by various research groups.[123,124] However, none of them have employed VPI to achieve this.

Birch wood was selected as model material for the experiments. First, a delignification process was applied.[125] As can be seen in **Figure 6.1**, after the delignification process, wood loses its brown colour.

Once the wood was delignified, different inorganic oxides (Al_2O_3, TiO_2, SiO_2, HfO_2, ZnO) were infiltrated by VPI under different conditions, including temperature, pulse and exposure time. Finally, the samples were mechanically pressed and their transmittance measured.

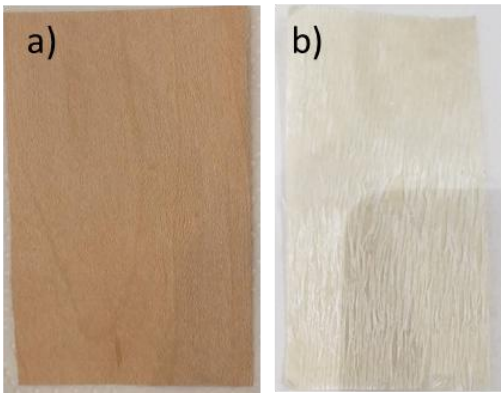

***Figure 6.1**: Birch wood sample before (a) and after (b) delignification.*

The detailed results of the conducted tests have not been received, making it impossible to comment on or analyse their outcomes at this time.

6.2.2 Development of ceramic coatings for the surface biofunctionalization of polymeric scaffolds in collaboration with Tecnun: School of Engineering (University of Navarra).

Regenerative medicine, particularly tissue engineering, is a growing field driven by the progressive aging of our society. This discipline focuses on creating artificial polymeric tissues that serve as scaffolds or support structures for the growth of healthy cells within the body. These structures often degrade during the repopulation process and eventually disappear once the new healthy tissue has fully formed. However, in many cases, certain polymers do not adequately support cell proliferation. The application of ceramic coatings on scaffolds can enhance their mechanical properties, biocompatibility, and bioactivity, improving their effectiveness in tissue regeneration.

Tecnun was manufacturing the structures using the following materials: PLLA, PVA, PETG, and PLGA. TiO_2 was selected as the coating material. Two different thicknesses of TiO_2 were deposited on these structures using ALD. Finally, the samples were returned to Tecnun, where cellular viability studies were conducted. The results obtained allowed us to conclude that the ceramic coating applied to biocompatible substrates did not have an adverse effect on cell proliferation, although it did not promote enhanced cell growth either.

6.2.3 Deposition of ceramic coatings for UV damage prevention in collaboration with the University of Minho.

Eco-friendly products, made from sustainable materials with low environmental impact, such as cork or rubber, help reduce waste and preserve the planet. However, they present some drawbacks, such as aging and degradation. When exposed to sunlight (UV radiation), they can suffer discoloration, loss of flexibility, and degradation of the natural polymers that make up their structure. In this regard, surface treatments for composite materials are a key aspect of their manufacturing process, as they can significantly improve their properties and make them more suitable for specific applications. Coatings should be opaque in the UV spectrum to block the damage caused by ultraviolet radiation and transparent in the visible range to preserve the material's colour and appearance. Transparent metal oxide films, such as zinc oxide (ZnO) and titanium dioxide (TiO_2), stand out as promising options for this purpose. [126,127]

Particles were coated with ZnO and TiO_2 in a fluidized bed reactor (FBR). FBR is a type of reactor in which solid particles are suspended and behave like a fluid when a gas or liquid is passed through them at a specific velocity. Different conditions were applied to rubber and cork. The

coated particles were sent to the University of Minho to test the effect of the coating on UV damage prevention. Up to this point, the detailed results of the conducted tests have not been provided, and therefore, it is not possible to comment on or analyse their outcomes at this time.

6.2.4 Plant seeds

Seed coating has evolved over time to fulfill multiple functions, such as protecting the seed against various insect pests, fungal strains, and rhizobia, supplying nutrients in the root absorption zone, incorporating compounds with high water retention capacity, applying substances that stimulate and regulate growth, adding agents that promote germination, including compounds that provide oxygen under partial anaerobic conditions, and optimizing seed size and weight for more precise sowing. [128]

Lentil seeds were coated with ZnO. The effect of the coating on germination was studied in water with different pH levels. For this purpose, varying thicknesses of ZnO were applied to the seeds. One of the tests is shown in **Figure 6.2**, which displays lentil seeds without ALD treatment (a) and lentil seeds with a ZnO coating (b) after 72 hours of exposure to 4 mL of water at ambient temperature. It was observed that the seeds coated with ZnO exhibited slower growth compared to the untreated seeds, suggesting that the coating may negatively impact the growth rate under the experimental conditions used.

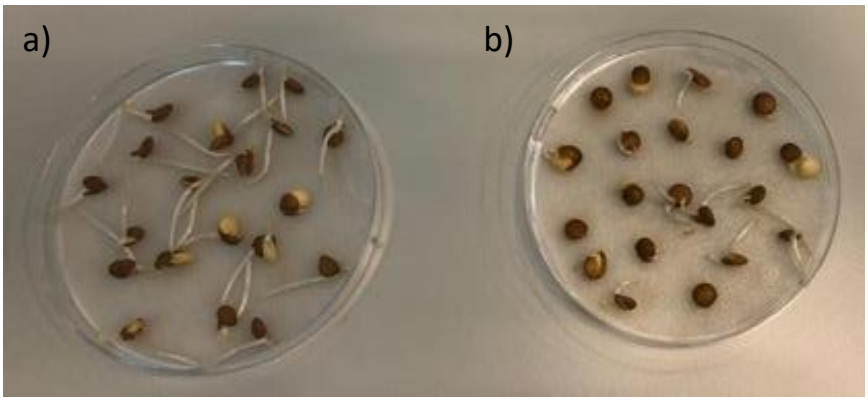

***Figure 6.2**: Lentil seeds without ALD treatment (a) and lentil seeds with a ZnO coating (b) after 72 hours of exposure to 4 mL of water at ambient temperature.*

6.3 OTHER ACTIVITIES

I also contributed to several other activities in the company, including:

1. Testing a new plasma reactor for Plasma-Enhanced Atomic Layer Deposition (PEALD).
2. Preparation of manuals for tools and recipes for the primary materials used in ALD.

3. Technical support for clients.
4. Involvement in the design of a new Fluidized Bed Reactor (FBR).
5. Optimization of a new reactor (**chapter 5**).

This industrial experience allowed me to validate various technical aspects and adapt them to real market needs, in addition to interacting with customers and gaining firsthand insight into the company's operations. This provided me with a practical and applied perspective that complements the theoretical foundations of this research.

Chapter 7 SUMMARY AND OUTLOOK

This doctoral thesis has explored the use of Molecular Layer Deposition (MLD) and combined Atomic Layer Deposition/Molecular Layer Deposition (ALD/MLD) strategies for the synthesis of functional thin films, particularly hybrid organic–inorganic materials. The research focused on their application in antibacterial and antifungal surface coatings, photocatalytic materials, and seed-coating technologies, with a view toward practical implementation in fields such as food packaging and agriculture.

In this thesis, polyamide 6,3 (PA63) thin films were synthesized using malonyl chloride and hexamethylenediamine as precursors. Additionally, hybrid materials were fabricated by integrating organic precursors (malonyl chloride, ethyleneglycol, glycerol, hydroquinone) with metal-containing components such as diethylzinc (DEZ) and titanium tetrachloride ($TiCl_4$), leading to the formation of metal-organic structures with unique properties.

Comprehensive characterization was conducted through techniques such as XRR, XRD, ATR-FTIR, XPS, QCM, SEM, TEM, and Raman spectroscopy. These analyses confirmed the successful deposition and structural integrity of the films and revealed valuable insights into their physical and chemical characteristics.

One of the key outcomes of this research was the demonstration of antibacterial functionality. Coatings based on PA63 and the hybrid Zn-based material exhibited significant antibacterial activity against both *Staphylococcus aureus* and *Escherichia coli*, representing Gram-positive and Gram-negative strains, respectively. However, antifungal assays with Aspergillus nidulans indicated that these coatings still need to be improved in order to effectively inhibit both hyphal growth and spore germination. Antimildew experiments performed under different conditions, show promising resistance to mold formation. These properties collectively make the developed materials attractive for extending product shelf life and improving safety in packaging and agricultural applications.

A novel aspect of this thesis involved the application of these functional coatings to seed germination platforms. Coated cotton samples exhibited enhanced resistance to fungal colonization without compromising germination viability. These preliminary results suggest that ALD/MLD coatings could be a viable alternative to traditional seed treatment methods, potentially reducing the use of chemical fungicides and supporting more sustainable agricultural practices.

In parallel, the photocatalytic activity of Ti-based hybrid coatings was studied. Glass substrates were coated with hybrid organic–inorganic multilayers using a combination of $TiCl_4$, H_2O, and various organic spacers (EG, GL, HQ). After thermal annealing to remove the organic content and generate porous anatase-rich TiO_2 structures, the samples were evaluated for their ability to degrade NO under UV light in accordance with ISO 22197-1:2007 standards. Notably, superlattice structures generated from alternating ALD and MLD cycles exhibited sustained photocatalytic efficiency over multiple testing cycles. These findings demonstrate the feasibility of tailoring material properties through ALD/MLD strategies to achieve enhanced performance in air purification or pollutant degradation applications.

In parallel with the materials research, the thesis focused on validating a custom-designed ALD reactor prototype incorporating a modular, adjustable-volume chamber. The reactor was tested with typical ALD materials (Al_2O_3 and ZnO), and the results confirmed its suitability for precise and reproducible thin film growth. This flexible system offers new opportunities for high-throughput screening and multi-material synthesis in research and industrial environments.

The industrial relevance of this work was further reinforced through collaboration with Ctechnano, contributing to the development and evaluation of functional coatings aimed at real-world applications. These projects included the surface functionalization of wood, scaffolds, and textiles. The integration of academic research with industrial development provided valuable insight into technology transfer, scalability, and the challenges associated with the commercialization of advanced coating technologies.

The findings presented in this thesis open multiple pathways for future research and technological development. First, expanding the range of metal and organic precursors could allow coatings to be tailored for specific functionalities such as UV blocking, self-cleaning, or biocompatibility.

Second, further studies are needed on the long-term stability, mechanical robustness, biocompatibility, and environmental impact of these coatings, in order to facilitate their transition from the laboratory to commercial applications. In particular, understanding the degradation mechanisms and durability of the materials under real-use conditions—such as humidity, abrasion, or UV exposure—will be crucial for their implementation in sectors such as food packaging and agriculture.

Third, it would be of interest to explore a broader range of bacterial strains and different families of fungi, in order to more comprehensively evaluate the antibacterial and antifungal spectrum of the developed coatings.

In summary, the work presented in this thesis illustrates how the precise control of atomic and molecular layers can be utilized to create multifunctional coatings with adjustable characteristics. The explored uses in antibacterial defense, photocatalytic activity, and reactor development underscore the adaptability of ALD/MLD techniques. These findings establish a strong platform for future research, offering opportunities to advance sustainable technologies and innovative material solutions across a wide range of industries.

LIST OF PUBLICATIONS

Azpiroz, R.; Borraz, M.; González, A.; Mansilla, C.; Iglesias, M.; Pérez-Torrente, J. J. Photocatalytic Activity in the In-Flow Degradation of NO on Porous TiO_2–Coated Glasses from Hybrid Inorganic–Organic Thin Films Prepared by a Combined ALD/MLD Deposition Strategy. *Coatings* **2022**, *12* (4), 488. https://doi.org/10.3390/coatings12040488

REFERENCES

1 Jolivet, A.; Labbé, C.; Frilay, C.; Debieu, O.; Marie, P.; Horcholle, B.; Lemarié, F.; Portier, X.; Grygiel, C.; Duprey, S.; Jadwisienczak, W.; Ingram, D.; Upadhyay, M.; David, A.; Fouchet, A.; Lüders, U.; Cardin, J. Structural, Optical, and Electrical Properties of TiO_2 Thin Films Deposited by ALD: Impact of the Substrate, the Deposited Thickness and the Deposition Temperature. *Appl. Surf. Sci.* **2022**, *608*, 155214. https://doi.org/10.1016/j.apsusc.2022.155214

2 Ylivaara, O. M. E.; Langner, A.; Ek, S.; Malm, J.; Julin, J.; Laitinen, M.; Ali, S.; Sintonen, S.; Lipsanen, H.; Sajavaara, T.; Puurunen, R. L. Thermomechanical Properties of Aluminum Oxide Thin Films Made by Atomic Layer Deposition. *J. Vac. Sci. Technol. A* **2022**, *40* (6). https://doi.org/10.1116/6.0002095

3 Adochițe, C.; Vițelaru, C.; Parau, A. C.; Kiss, A. E.; Pană, I.; Vlădescu, A.; Costinaș, S.; Moga, M.; Muntean, R.; Badea, M.; Idomir, M. Synthesis and Investigation of Antibacterial Activity of Thin Films Based on TiO_2-Ag and SiO_2-Ag with Potential Applications in Medical Environment. *Nanomaterials* **2022**, *12* (6), 902. https://doi.org/10.3390/nano12060902

4 Raut, H. K.; Ganesh, V. A.; Nair, A. S.; Ramakrishna, S. Anti-Reflective Coatings: A Critical, In-Depth Review. *Energy Environ. Sci.* **2011**, *4* (10), 3779. https://doi.org/10.1039/c1ee01297e

5 Ozaydin-Ince, G.; Coclite, A. M.; Gleason, K. K. CVD of Polymeric Thin Films: Applications in Sensors, Biotechnology, Microelectronics/Organic Electronics, Microfluidics, MEMS, Composites and Membranes. *Rep. Prog. Phys.* **2012**, *75* (1), 016501. https://doi.org/10.1088/0034-4885/75/1/016501

6 Alghamdi, H. M.; Rajeh, A. Synthesis and Improved Optical, Electrical, and Dielectric Properties of PEO/PVA/$CuCo_2O_4$ Nanocomposites. *Sci. Rep.* **2024**, *14* (1). https://doi.org/10.1038/s41598-024-69982-4

7 Kumar, A.; Mishra, V.; Negi, S.; Kar, S. A Systematic Review on Polymer-Based Superhydrophobic Coating for Preventing Biofouling Menace. *J. Coat. Technol. Res.* **2023**, *20* (5), 1499–1512. https://doi.org/10.1007/s11998-023-00773-8

8 Song, Q.; Xiao, Z.; Gao, H.; Chen, X.; Wang, K.; Zhao, R.; Wei, D. Antibacterial Polymeric Coatings Synthesized by Solvent-Free Initiated Chemical Vapor Deposition: A Review. *Chem. Eng. J.* **2024**, *494*, 152287. https://doi.org/10.1016/j.cej.2024.152287

9 Kanno, I. Fundamentals of Piezoelectric Thin Films for Microelectromechanical Systems. In *Elsevier eBooks*; Elsevier, 2019; pp 237–255. https://doi.org/10.1016/b978-0-12-813856-4.00008-9

10 Puurunen, R. L. A Short History of Atomic Layer Deposition: Tuomo Suntola's Atomic Layer Epitaxy. *Chem. Vap. Depos.* **2014**, *20* (10–12), 332–344. https://doi.org/10.1002/cvde.201402012

11 Álvarez Yenes, A. *Growth of Boron Nitride by Atomic Layer Deposition*; Master's Thesis, Universidad del País Vasco, 2021; Unpublished manuscript.

12 George, S. M. Atomic Layer Deposition: An Overview. *Chem. Rev.* **2010**, *110* (1), 111–131. https://doi.org/10.1021/cr900056b

13 Johnson, R. W.; Hultqvist, A.; Bent, S. F. A Brief Review of Atomic Layer Deposition: From Fundamentals to Applications. *Mater. Today* **2014**, *17* (5), 236–246. https://doi.org/10.1016/j.mattod.2014.04.026

14 Meng, X. An Overview of Molecular Layer Deposition for Organic and Organic–Inorganic Hybrid Materials: Mechanisms, Growth Characteristics, and Promising Applications. *J. Mater. Chem. A* **2017**, *5*, 18326–18378. https://doi.org/10.1039/C7TA04449F

15 Du, Y.; George, S. M. Molecular Layer Deposition of Nylon 66 Films Examined Using *in Situ* FTIR Spectroscopy. *J. Phys. Chem. C* **2007**, *111* (24), 8509–8517. https://doi.org/10.1021/jp067041n

16 Dameron, A. A.; Seghete, D.; Burton, B. B.; Davidson, S. D.; Cavanagh, A. S.; Bertrand, J. A.; George, S. M. Molecular Layer Deposition of Alucone Polymer Films Using

Trimethylaluminum and Ethylene Glycol. *Chem. Mater.* **2008**, *20* (10), 3315–3326. https://doi.org/10.1021/cm7032977

17 Wilson, C. A.; Grubbs, R. K.; George, S. M. Nucleation and Growth during Al_2O_3 Atomic Layer Deposition on Polymers. *Chem. Mater.* **2005**, *17* (23), 5625–5634. https://doi.org/10.1021/cm050704d

18 Knez, M. Diffusion Phenomena in Atomic Layer Deposition. *Semicond. Sci. Technol.* **2012**, *27* (7), 074001. https://doi.org/10.1088/0268-1242/27/7/074001

19 Lee, S.; Pippel, E.; Gösele, U.; Dresbach, C.; Qin, Y.; Chandran, C. V.; Bräuniger, T.; Hause, G.; Knez, M. Greatly Increased Toughness of Infiltrated Spider Silk. *Science* **2009**, *324* (5926), 488–492. https://doi.org/10.1126/science.1168162

20 Peng, Q.; Elam, J. W. Nanoscopic Patterned Materials with Tunable Dimensions via Atomic Layer Deposition on Block Copolymers. *Adv. Mater.* **2010**, *22*, 5129–5133. https://doi.org/10.1002/adma.201002465

21 Gong, B.; Parsons, G. N. Sequential Vapor Infiltration of Metal Oxides into Sacrificial Polyester Fibers: Shape Replication and Controlled Porosity of Microporous/Mesoporous Oxide Monoliths. *Chem. Mater.* **2011**, *23* (15), 3476–3485. https://doi.org/10.1021/cm200694w

22 Leng, C. Z.; Losego, M. D. Vapor Phase Infiltration (VPI) for Transforming Polymers into Organic–Inorganic Hybrid Materials: A Critical Review of Current Progress and Future Challenges. *Mater. Horiz.* **2017**, *4* (5), 747–771. https://doi.org/10.1039/c7mh00196g

23 Azpitarte, I.; Knez, M. Vapor Phase Infiltration: From a Bioinspired Process to Technologic Application, a Prospective Review. *MRS Commun.* **2018**, *8* (3), 727–741. https://doi.org/10.1557/mrc.2018.126

24 McGuinness, E. K.; Zhang, F.; Ma, Y.; Lively, R. P.; Losego, M. D. Vapor Phase Infiltration of Metal Oxides into Nanoporous Polymers for Organic Solvent Separation Membranes. *Chem. Mater.* **2019**, *31* (15), 5509–5518. https://doi.org/10.1021/acs.chemmater.9b01141

25 Rejab, M. R.; Hamdan, M. H.; Quanjin, M.; Siregar, J. P.; Bachtiar, D.; Muchlis, Y. Historical Development of Hybrid Materials. In *Elsevier eBooks*; 2019; pp 445–455. https://doi.org/10.1016/b978-0-12-803581-8.10546-6

26 Arnold, D. E. *Maya Blue*. In *Springer eBooks*; 2014; pp 1–4. https://doi.org/10.1007/978-94-007-3934-5_10170-1

27 Faustini, M.; Nicole, L.; Ruiz-Hitzky, E.; Sanchez, C. History of Organic–Inorganic Hybrid Materials: Prehistory, Art, Science, and Advanced Applications. *Adv. Funct. Mater.* **2018**, *28* (27). https://doi.org/10.1002/adfm.201704158

28 Krasia-Christoforou, T. *Organic–Inorganic Polymer Hybrids: Synthetic Strategies and Applications*; In *Springer eBooks*; Springer: **2015**; pp 11–63. https://doi.org/10.1007/978-3-319-12868-9_2

29 Nilsen, O.; Fjellvåg, H. *Thin Films Prepared with Gas Phase Deposition Technique (WO 2006/071126 A1)*; World Intellectual Property Organization: **2006**.

30 Gregorczyk, K.; Knez, M. Hybrid Nanomaterials through Molecular and Atomic Layer Deposition: Top Down, Bottom Up, and In-Between Approaches to New Materials. *Prog. Mater. Sci.* **2015**, *75*, 1–37. https://doi.org/10.1016/j.pmatsci.2015.06.004

31 Capuano, E.; Van Ruth, S. Infrared Spectroscopy: Applications. In *Elsevier eBooks*; Elsevier: **2015**; pp 424–431. https://doi.org/10.1016/b978-0-12-384947-2.00644-9

32 Subramanian, A.; Rodriguez-Saona, L. Fourier Transform Infrared (FTIR) Spectroscopy. In *Elsevier eBooks*; Elsevier: **2009**; pp 145–178. https://doi.org/10.1016/b978-0-12-374136-3.00007-9

33 Yasaka, M. X-Ray Thin-Film Measurement Techniques. *The Rigaku Journal* **2010**, *26* (2).

34 Dann, S. E. *Reactions and Characterization of Solids.* In *The Royal Society of Chemistry eBooks*; The Royal Society of Chemistry: 2000. https://doi.org/10.1039/9781847551825

35 Bunaciu, A. A.; Udriştioiu, E. G.; Aboul-Enein, H. Y. X-Ray Diffraction: Instrumentation and Applications. *Crit. Rev. Anal. Chem.* **2015**, *45* (4), 289–299. https://doi.org/10.1080/10408347.2014.949616

36 Stevie, F. A.; Donley, C. L. Introduction to X-Ray Photoelectron Spectroscopy. *J. Vac. Sci. Technol. A* **2020**, *38* (6). https://doi.org/10.1116/6.0000412

37 Teramura, Y.; Takai, M. Quartz Crystal Microbalance. In *Springer eBooks*; Springer: 2018; pp 509–520. https://doi.org/10.1007/978-981-10-6156-1_83

38 Liu, L.; Bhatia, R.; Webster, T. Atomic layer deposition of nano-TiO_2 thin films with enhanced biocompatibility and antibacterial activity for orthopedic implants. International Journal Of Nanomedicine 2017, Volume 12, 8711-8723. https://doi.org/10.2147/ijn.s148065.

39 ISO 22197-1:2007. *Fine Ceramics, Advanced Technical Ceramics – Test Method for Air-Purification Performance of Semiconducting Photocatalytic Materials. Part 1: Removal of Nitric Oxide*; International Organization for Standardization: Geneva, Switzerland, 2007.

40 *Modern Techniques of Spectroscopy.* In *Progress in Optical Science and Photonics*; Springer: 2021. https://doi.org/10.1007/978-981-33-6084-6

41 Metilli, L.; Francis, M.; Povey, M.; Lazidis, A.; Marty-Terrade, S.; Ray, J.; Simone, E. Latest Advances in Imaging Techniques for Characterizing Soft, Multiphasic Food Materials. *Adv. Colloid Interface Sci.* **2020**, *279*, 102154. https://doi.org/10.1016/j.cis.2020.102154

42 Deopura, B.; Padaki, N. Synthetic Textile Fibres. In *Elsevier eBooks*; Elsevier: 2014; pp 97–114. https://doi.org/10.1016/b978-1-84569-931-4.00005-2

43 Gomes, I. M.; Monteiro, A. H.; Chaves, E. G.; Teixeira, S. C. D. S.; Berry, N. G.; De Gans-Li, L.; Dias, F. V. L.; Da Silva, M. J. G. Integrity Analysis of Polyamide 12 Applied in Oil Pipelines. *J. Therm. Anal. Calorim.* **2024**, *149* (24), 14615–14623. https://doi.org/10.1007/s10973-024-13843-9

44 Cozzarini, L.; Benedetti, E.; Piras, A.; Terenzi, A.; Pricl, S.; Schmid, C. Mechanical and Flammability Properties of a Polyamide 6,6 Nanocomposite for Nonstructural Marine

Engine Components. *J. Polym. Eng.* **2020**, *41* (1), 27–33. https://doi.org/10.1515/polyeng-2020-0179

45 Latko, P.; Boczkowska, A. Electronic Applications of Polyamide Elastomers and Its Composites. In *Springer Series on Polymer and Composite Materials*; Springer: 2015; pp 135–160. https://doi.org/10.1007/978-3-319-23663-6_5

46 Maitz, M. F. Applications of Synthetic Polymers in Clinical Medicine. *Biointerphases* **2015**, *1* (3), 161–176. https://doi.org/10.1016/j.bsbt.2015.08.002

47 Tyuftin, A. A.; Kerry, J. P. Review of Surface Treatment Methods for Polyamide Films for Potential Application as Smart Packaging Materials: Surface Structure, Antibacterial and Spectral Properties. *Food Packag. Shelf Life* **2020**, *24*, 100475. https://doi.org/10.1016/j.fpsl.2020.100475

48 Rhim, J.; Park, H.; Ha, C. Bio-Nanocomposites for Food Packaging Applications. *Prog. Polym. Sci.* **2013**, *38* (10–11), 1629–1652. https://doi.org/10.1016/j.progpolymsci.2013.05.008

49 Huang, W.; Hu, X.; Zhai, J.; Zhu, N.; Guo, K. Biorenewable Furan-Containing Polyamides. *Mater. Today Sustain.* **2020**, *10*, 100049. https://doi.org/10.1016/j.mtsust.2020.100049

50 Sanchez, C.; Belleville, P.; Popall, M.; Nicole, L. Applications of Advanced Hybrid Organic–Inorganic Nanomaterials: From Laboratory to Market. *ChemInform* **2011**, *42* (24). https://doi.org/10.1002/chin.201124253

51 Yoon, B.; O'Patchen, J. L.; Seghete, D.; Cavanagh, A. S.; George, S. M. Molecular Layer Deposition of Hybrid Organic–Inorganic Polymer Films Using Diethylzinc and Ethylene Glycol. *Chem. Vap. Depos.* **2009**, *15* (4–6), 112–121. https://doi.org/10.1002/cvde.200806756

52 Berger, R.; Seiler, M.; Perrotta, A.; Coclite, A. M. Study on Porosity in Zinc Oxide Ultrathin Films from Three-Step MLD Zn-Hybrid Polymers. *Materials* **2021**, *14* (6), 1418. https://doi.org/10.3390/ma14061418

53 Imani, S. M.; Ladouceur, L.; Marshall, T.; Maclachlan, R.; Soleymani, L.; Didar, T. F. Antibacterial Nanomaterials and Coatings: Current Mechanisms and Future Perspectives to Control the Spread of Viruses Including SARS-CoV-2. *ACS Nano* **2020**, *14*, 12341–12369. https://doi.org/10.1021/acsnano.0c05937

54 Shirvanimoghaddam, K.; Akbari, M. K.; Yadav, R.; Al-Tamimi, A. K.; Naebe, M. Fight Against COVID-19: The Case of Antiviral Surfaces. *APL Mater.* **2021**, *9*, 031112. https://doi.org/10.1063/5.0043009

55 Srisa, A.; Promhuad, K.; San, H.; Laorenza, Y.; Wongphan, P.; Wadaugsorn, K.; Sodsai, J.; Kaewpetch, T.; Tansin, K.; Harnkarnsujarit, N. Antibacterial, Antifungal and Antiviral Polymeric Food Packaging in Post-COVID-19 Era. Polymers 2022, 14 (19), 4042. https://doi.org/10.3390/polym14194042

56 Aguirre-Joya, J. A.; De Leon-Zapata, M. A.; Alvarez-Perez, O. B.; Torres-León, C.; Nieto-Oropeza, D. E.; Ventura-Sobrevilla, J. M.; Aguilar, M. A.; Ruelas-Chacón, X.; Rojas, R.; Ramos-Aguiñaga, M. E.; Aguilar, C. N. Basic and Applied Concepts of Edible Packaging for Foods. In *Elsevier eBooks*; Elsevier, **2018**; pp 1–61. https://doi.org/10.1016/b978-0-12-811516-9.00001-4

57 Van Long, N. N.; Dantigny, P. Fungal Contamination in Packaged Foods. In *Elsevier eBooks*; Elsevier, **2016**; pp 45–63. https://doi.org/10.1016/b978-0-12-800723-5.00004-8

58 Johnson, R. W.; Hultqvist, A.; Bent, S. F. A Brief Review of Atomic Layer Deposition: From Fundamentals to Applications. *Mater. Today* **2014**, *17* (5), 236–246. https://doi.org/10.1016/j.mattod.2014.04.026

59 Nazarov, D.; Kozlova, L.; Rogacheva, E.; Kraeva, L.; Maximov, M. Atomic Layer Deposition of Antibacterial Nanocoatings: A Review. *Antibiotics* **2023**, *12* (12), 1656. https://doi.org/10.3390/antibiotics12121656

60 Haq, I. U.; Vieira, R. P.; Lima, W. G.; De Lima, M. E.; Krukiewicz, K. Antibacterial Polymers: Elucidating the Role of Functional Groups on Antibacterial Activity. *Arab. J. Basic Appl. Sci.* **2024**, *31* (1), 325–344. https://doi.org/10.1080/25765299.2024.2366543

61 Sun, Q.; Li, J.; Le, T. Zinc Oxide Nanoparticle as a Novel Class of Antifungal Agents: Current Advances and Future Perspectives. *J. Agric. Food Chem.* **2018**, *66* (43), 11209–11220. https://doi.org/10.1021/acs.jafc.8b03210

62 Riseh, R. S.; Vazvani, M. G.; Vatankhah, M.; Kennedy, J. F. Chitosan Coating of Seeds Improves the Germination and Growth Performance of Plants: A Review. *Int. J. Biol. Macromol.* **2024**, *278*, 134750. https://doi.org/10.1016/j.ijbiomac.2024.134750

63 ISO 22196:2011 – *Measurement of Antibacterial Activity on Plastics and Other Non-Porous Surfaces*; International Organization for Standardization: Geneva, Switzerland, 2011. Available online: https://www.iso.org/standard/54431.html (accessed 2025-06-10).

64 Sun, Q.; Li, J.; Le, T. Zinc Oxide Nanoparticle as a Novel Class of Antifungal Agents: Current Advances and Future Perspectives. Journal Of Agricultural And Food Chemistry **2018**, 66 (43), 11209-11220. https://doi.org/10.1021/acs.jafc.8b03210.

65 Myers, T. J.; George, S. M. Molecular Layer Deposition of Nylon 2,6 Polyamide Polymer on Flat and Particle Substrates in an Isothermal Enclosure Containing a Rotary Reactor. *J. Vac. Sci. Technol., A* **2021**, *39* (5), 052405. https://doi.org/10.1116/6.0001162

66 Gakis, G. P.; Vahlas, C.; Vergnes, H.; Dourdain, S.; Tison, Y.; Martinez, H.; Bour, J.; Ruch, D.; Boudouvis, A. G.; Caussat, B.; Scheid, E. Investigation of the initial deposition steps and the interfacial layer of Atomic Layer Deposited (ALD) Al2O3 on Si. Applied Surface Science **2019**, 492, 245-254. https://doi.org/10.1016/j.apsusc.2019.06.215.

67 Bermúdez, M.; León, S.; Alemán, C.; Muñoz-Guerra, S. Structure and Morphology of Nylon 46 Lamellar Crystals: Electron Microscopy and Energy Calculations. *J. Polym. Sci., Part B: Polym. Phys.* **2000**, *38* (1), 41–52. https://doi.org/10.1002/(SICI)1099-0488(20000101)38:1<41::AID-POLB5>3.0.CO;2-D

68 Vitasovic, T.; Caniglia, G.; Eghtesadi, N.; Ceccato, M.; Bo Jesen, E. D.; Gosewinkel, U.; Neusser, G.; Rupp, U.; Walther, P.; Kranz, C.; Ferapontova, E. E. Antibacterial Action of Zn2+ Ions Driven by the In Vivo Formed ZnO Nanoparticles. ACS Applied Materials & Interfaces 2024, 16 (24), 30847-30859. https://doi.org/10.1021/acsami.4c04682.

69 Pasquet, J.; Chevalier, Y.; Pelletier, J.; Couval, E.; Bouvier, D.; Bolzinger, M.-A. The contribution of zinc ions to the antibacterial activity of zinc oxide. Colloids And Surfaces A Physicochemical And Engineering Aspects 2014, 457, 263-274. https://doi.org/10.1016/j.colsurfa.2014.05.057.

70 Ivanova, E. P.; Linklater, D. P.; Aburto-Medina, A.; Le, P.; Baulin, V. A.; Nguyen, H. K. D.; Curtain, R.; Hanssen, E.; Gervinskas, G.; Ng, S. H.; Truong, V. K.; Luque, P.; Ramm, G.; Wösten, H. A.; Crawford, R. J.; Juodkazis, S.; Maclaughlin, S. Antifungal versus Antibacterial Defence of Insect Wings. *J. Colloid Interface Sci.* **2021**, *603*, 886–897. https://doi.org/10.1016/j.jcis.2021.06.093

71 Breijyeh, Z.; Jubeh, B.; Karaman, R. Resistance of Gram-Negative Bacteria to Current Antibacterial Agents and Approaches to Resolve It. Molecules **2020**, 25 (6), 1340. https://doi.org/10.3390/molecules25061340.

72 Steinberg, G. Hyphal Growth: a Tale of Motors, Lipids, and the Spitzenkörper. Eukaryotic Cell **2007**, 6 (3), 351-360. https://doi.org/10.1128/ec.00381-06.

73 Seinfeld, J. H.; Pandis, S. N. Atmospheric Chemistry and Physics: From Air Pollution to Climate Change; Wiley: New York, 1998.

74 Brimblecombe, P. *The Effects of Air Pollution on the Built Environment*; Imperial College Press: Cambridge, 2003.

75 Harrison, R. M.; Hester, R. E. *Air Quality in Urban Environments*; Royal Society of Chemistry: Cambridge, 2009.

76 Guo, Q.; Zhou, C.; Ma, Z.; Yang, X. Fundamentals of TiO_2 Photocatalysis: Concepts, Mechanisms, and Challenges. *Adv. Mater.* **2019**, *31*, 1901997. https://doi.org/10.1002/adma.201901997

77 Schneider, J.; Matsuoka, M.; Takeuchi, M.; Zhang, J.; Horiuchi, Y.; Anpo, M.; Bahnemann, D. W. Understanding TiO_2 Photocatalysis: Mechanisms and Materials. *Chem. Rev.* **2014**, *114*, 9919–9986. https://doi.org/10.1021/cr5001892

78 Nakata, K.; Fujishima, A. TiO_2 Photocatalysis: Design and Applications. *J. Photochem. Photobiol. C: Photochem. Rev.* **2012**, *13*, 169–189. https://doi.org/10.1016/j.jphotochemrev.2012.06.001

79 Fujishima, A.; Rao, T. N.; Tryk, D. A. Titanium Dioxide Photocatalysis. *J. Photochem. Photobiol. C: Photochem. Rev.* **2000**, *1*, 1–21. https://doi.org/10.1016/S1389-5567(00)00002-2

80 Fujishima, A.; Zhang, X. Fotocatálisis con Dióxido de Titanio: Situación Actual y Enfoques Futuros. *Chimie* **2006**, *9*, 750–760. https://doi.org/10.1016/j.crci.2005.02.055

81 Lasek, J.; Yu, Y.-H.; Wu, J. C. S. Removal of NOx by Photocatalytic Processes. *J. Photochem. Photobiol. C: Photochem. Rev.* **2013**, *14*, 29–52. https://doi.org/10.1016/j.jphotochemrev.2012.10.003

82 Dambournet, D.; Belharouak, I.; Amine, K. Tailored Preparation Methods of TiO_2 Anatase, Rutile, Brookite: Mechanism of Formation and Electrochemical Properties. *Chem. Mater.* **2010**, *22*, 1173–1179. https://doi.org/10.1021/cm902179t

83 Nosheen, S.; Galasso, F. S.; Suib, S. L. Role of Ti−O Bonds in Phase Transitions of TiO_2. *Langmuir* **2009**, *25*, 7623–7630. https://doi.org/10.1021/la900516c

84 Feist, T. P.; Davies, P. K. The Soft Chemical Synthesis of TiO_2(B) from Layered Titanates. *J. Solid State Chem.* **1992**, *101*, 275–295. https://doi.org/10.1016/0022-4596(92)90171-U

85 Zhang, J.; Li, M.; Feng, Z.; Chen, J.; Li, C. UV Raman Spectroscopic Study on TiO_2. I. Phase Transformation at the Surface and in the Bulk. *J. Phys. Chem. B* **2006**, *110*, 927–935. https://doi.org/10.1021/jp054283k

86 Su, W.; Zhang, J.; Feng, Z.; Chen, T.; Ying, P.; Li, C. Surface Phases of TiO_2 Nanoparticles Studied by UV Raman Spectroscopy and FT-IR Spectroscopy. *J. Phys. Chem. C* **2008**, *112*, 7710–7716. https://doi.org/10.1021/jp711924h

87 Shi, J.; Chen, J.; Feng, Z.; Chen, T.; Lian, Y.; Wang, X.; Li, C. Photoluminescence Characteristics of TiO_2 and Their Relationship to the Photoassisted Reaction of

Water/Methanol Mixture. *J. Phys. Chem. C* **2007**, *111*, 693–699. https://doi.org/10.1021/jp0640900

88 Zhang, J.; Xu, Q.; Li, M.; Feng, Z.; Li, C. UV Raman Spectroscopic Study on TiO_2. II. Effect of Nanoparticle Size on the Outer/Inner Phase Transformations. *J. Phys. Chem. C* **2009**, *113*, 1698–1704. https://doi.org/10.1021/jp807749n

89 Zhang, H. Z.; Banfield, J. F. Understanding Polymorphic Phase Transformation Behavior during Growth of Nanocrystalline Aggregates: Insights from TiO_2. *J. Phys. Chem. B* **2000**, 104, 3481–3487. https://doi.org/10.1021/jp994090m

90 Ma, Y.; Wang, X.; Jia, Y.; Chen, X.; Han, H.; Li, C. Titanium Dioxide-Based Nanomaterials for Photocatalytic Fuel Generations. *Chem. Rev.* **2014**, 114, 9987–10043. https://doi.org/10.1021/cr5001892

91 Wang, Y.; Li, B.; Zhang, C.; Cui, L.; Kang, S.; Li, X.; Zhou, L. Ordered Mesoporous CeO_2-TiO_2 Composites: Highly Efficient Photocatalysts for the Reduction of CO_2 with H_2O under Simulated Solar Irradiation. *Appl. Catal., B* **2013**, *130–131*, 277–284. https://doi.org/10.1016/j.apcatb.2013.01.031

92 Carp, O.; Huisman, C. L.; Reller, A. Photoinduced Reactivity of Titanium Dioxide. *Prog. Solid State Chem.* **2004**, *32*, 33–177. https://doi.org/10.1016/j.progsolidstchem.2004.08.001

93 Chen, M.; Chu, J.-W. NOx Photocatalytic Degradation on Active Concrete Road Surface — From Experiment to Real-Scale Application. *J. Cleaner Prod.* **2011**, *19*, 1266–1272. https://doi.org/10.1016/j.jclepro.2011.04.018

94 Hu, Y.; Higashimoto, S.; Martra, G.; Zhang, J.; Matsuoka, M.; Coluccia, S.; Anpo, M. Local Structures of Active Sites on Ti-MCM-41 and Their Photocatalytic Reactivity for the Decomposition of NO. *Catal. Lett.* **2003**, *90*, 161–163. https://doi.org/10.1023/A:1025382701322

95 Zheng, Z.; Huang, B.; Qin, X.; Zhang, X.; Dai, Y. Strategic Synthesis of Hierarchical TiO2 Microspheres with Enhanced Photocatalytic Activity. *Chem. Eur. J.* **2010**, *16*, 11266–11270. https://doi.org/10.1002/chem.201001456

96 Liu, B.; Nakata, K.; Sakai, M.; Saito, H.; Ochiai, T.; Murakami, T.; Takagi, K.; Fujishima, A. Mesoporous TiO2 Core–Shell Spheres Composed of Nanocrystals with Exposed High-Energy Facets: Facile Synthesis and Formation Mechanism. *Langmuir* **2011**, *27*, 8500–8508. https://doi.org/10.1021/la2015766

97 Li, H.; Bian, Z.; Zhu, J.; Zhang, D.; Li, G.; Huo, Y.; Li, H.; Lu, Y. Mesoporous Titania Spheres with Tunable Chamber Structure and Enhanced Photocatalytic Activity. *J. Am. Chem. Soc.* **2007**, *129*, 8406–8407. https://doi.org/10.1021/ja071231m

98 Chen, Y.; Tian, G.; Ren, Z.; Tian, C.; Pan, K.; Zhou, W.; Fu, H. Solvothermal Synthesis, Characterization, and Formation Mechanism of a Single-Layer Anatase TiO2 Nanosheet with a Porous Structure. *Eur. J. Inorg. Chem.* **2011**, 754–760. https://doi.org/10.1002/ejic.201001199

99 Zhan, S.; Chen, D.; Jiao, X.; Tao, C. Long TiO2 Hollow Fibers with Mesoporous Walls: Sol–Gel Combined Electrospun Fabrication and Photocatalytic Properties. *J. Phys. Chem. B* **2006**, *110*, 11199–11204. https://doi.org/10.1021/jp0616689

100 Ponnusamy, D.; Madanagurusamy, S. Porous Anatase TiO_2 Thin Films for NH_3 Vapour Sensing. *J. Electron. Mater.* **2015**, *44*, 4726–4733. https://doi.org/10.1007/s11664-015-3773-7

101 Sanzaro, S.; Smecca, E.; Mannino, G.; Bongiorno, C.; Pellegrino, G.; Neri, F.; Malandrino, G.; Catalano, M. R.; Condorelli, G. G.; Iacobellis, R.; De Marco, L.; Spinella, C.; La Magna, A.; Alberti, A. Multi-Scale-Porosity TiO_2 Scaffolds Grown by Innovative Sputtering Methods for High Throughput Hybrid Photovoltaics. *Sci. Rep.* **2016**, *6*, 39509. https://doi.org/10.1038/srep39509

102 Garcia-Valenzuela, A.; Alvarez, R.; Rico, V.; Cotrino, J.; Elipe, A. R.-G.; Palmero, A. Growth of Nanocolumnar Porous TiO_2 Thin Films by Magnetron Sputtering Using Particle Collimators. *Surf. Coat. Technol.* **2018**, *343*, 172–177. https://doi.org/10.1016/j.surfcoat.2018.03.041

103 Arconada, N.; Durán, A.; Suárez Gil, S.; Portela, R.; Coronado, J. M.; Sánchez, B.; Castro Martín, Y. Synthesis and Photocatalytic Properties of Dense and Porous TiO_2-

Anatase Thin Films Prepared by Sol–Gel. *Appl. Catal. B: Environ.* **2009**, *86*, 1–7. https://doi.org/10.1016/j.apcatb.2008.08.017

104 Abdulagatov, A. I.; Hall, R. A.; Sutherland, J. L.; Lee, B. H.; Cavanagh, A. S.; George, S. M. Molecular Layer Deposition of Titanicone Films using TiCl4 and Ethylene Glycol or Glycerol: Growth and Properties. *Chemistry Of Materials* **2012**, *24* (15), 2854-2863. https://doi.org/10.1021/cm300162v

105 Ishchuk, S.; Taffa, D. H.; Hazut, O.; Kaynan, N.; Yerushalmi, R. Transformation of Organic–Inorganic Hybrid Films Obtained by Molecular Layer Deposition to Photocatalytic Layers with Enhanced Activity. *ACS Nano* **2012**, *6* (8), 7263–7269. https://doi.org/10.1021/nn3022903

106 Chen, C.; Li, P.; Wang, G.; Yu, Y.; Duan, F.; Chen, C.; Song, W.; Qin, Y.; Knez, M. Nanoporous Nitrogen-Doped Titanium Dioxide with Excellent Photocatalytic Activity under Visible Light Irradiation Produced by Molecular Layer Deposition. *Angew. Chem. Int. Ed.* **2013**, *52* (35), 9196–9200. https://doi.org/10.1002/anie.201302329

107 Sarkar, D.; Ishchuk, S.; Taffa, D. H.; Kaynan, N.; Berke, B. A.; Bendikov, T.; Yerushalmi, R. Oxygen-Deficient Titania with Adjustable Band Positions and Defects: Molecular Layer Deposition of Hybrid Organic–Inorganic Thin Films as Precursors for Enhanced Photocatalysis. *J. Phys. Chem. C* **2016**, *120* (7), 3853–3862. https://doi.org/10.1021/acs.jpcc.5b11795

108 George, S. M.; Lee, B. H.; Yoon, B.; Abdulagatov, A. I.; Hall, R. A. Metalcones: Hybrid Organic–Inorganic Films Fabricated Using Atomic and Molecular Layer Deposition Techniques. *J. Nanosci. Nanotechnol.* **2011**, *11*, 7948–7955. https://doi.org/10.1166/jnn.2011.5034

109 Liang, X.; Yu, M.; Li, J.; Jiang, Y.-B.; Weimer, A. W. Ultra-Thin Microporous–Mesoporous Metal Oxide Films Prepared by Molecular Layer Deposition. *Chem. Commun.* **2009**, *7140–7142*. https://doi.org/10.1039/B911888H

110 Dey, N. K.; Kim, M. J.; Kim, K.-D.; Seo, H. O.; Kim, D.; Kim, Y. D.; Lim, D. C.; Lee, K. H. Adsorption and Photocatalytic Degradation of Methylene Blue over TiO2 Films on

Carbon Fiber Prepared by Atomic Layer Deposition. *J. Mol. Catal. A: Chem.* **2011**, *337* (1–2), 33–38. https://doi.org/10.1016/j.molcata.2011.01.010

111 Kim, S.; Chang, H.-K.; Kim, K. B.; Kim, H.-J.; Lee, H.-N.; Park, T. J.; Park, Y. M. Highly Porous SnO2/TiO2 Heterojunction Thin-Film Photocatalyst Using Gas-Flow Thermal Evaporation and Atomic Layer Deposition. *Catalysts* **2021**, *11* (10), 1144. https://doi.org/10.3390/catal11101144

112 Buchalska, M.; Surówka, M.; Hämäläinen, J.; Iivonen, T.; Leskelä, M.; Macyk, W. Photocatalytic Activity of TiO2 Films on Si Support Prepared by Atomic Layer Deposition. *Catal. Today* **2014**, *252*, 14–19. https://doi.org/10.1016/j.cattod.2014.09.032

113 Ishchuk, S.; Taffa, D. H.; Hazut, O.; Kaynan, N.; Yerushalmi, R. Transformation of Organic–Inorganic Hybrid Films Obtained by Molecular Layer Deposition to Photocatalytic Layers with Enhanced Activity. *ACS Nano* **2012**, *6* (8), 7263–7269. https://doi.org/10.1021/nn302370y

114 Russell, H. S.; Frederickson, L. B.; Hertel, O.; Ellermann, T.; Jensen, S. S. A Review of Photocatalytic Materials for Urban NOx Remediation. *Catalysts* **2021**, *11* (6), 675. https://doi.org/10.3390/catal11060675

115 Devahasdin, S.; Fan, C.; Li, K.; Chen, D. H. TiO_2 Photocatalytic Oxidation of Nitric Oxide: Transient Behavior and Reaction Kinetics. *J. Photochem. Photobiol. A: Chem.* **2003**, *156* (1–3), 161–170. https://doi.org/10.1016/s1010-6030(03)00005-4

116 Mills, A.; Elouali, S. The Nitric Oxide ISO Photocatalytic Reactor System: Measurement of NOx Removal Activity and Capacity. *J. Photochem. Photobiol. A: Chem.* **2015**, *305*, 29–36. https://doi.org/10.1016/j.jphotochem.2015.03.002

117 Baptista, A.; Silva, F.; Porteiro, J.; Míguez, J.; Pinto, G. Sputtering Physical Vapour Deposition (PVD) Coatings: A Critical Review on Process Improvement and Market Trend Demands. *Coatings* **2018**, *8* (11), 402. https://doi.org/10.3390/coatings8110402

118 Guanghui, F.; Jiafeng, D.; Donghui, P.; Ouli, H. The Migration of Alkali Ions from Glass Substrates Coated with Sol-Gel Barrier Films. *J. Non-Cryst. Solids* **1989**, *112* (1–3), 454–457. https://doi.org/10.1016/0022-3093(89)90572-3

119 Klepper, K. B.; Nilsen, O.; Fjellvåg, H. Deposition of Thin Films of Organic–Inorganic Hybrid Materials Based on Aromatic Carboxylic Acids by Atomic Layer Deposition. *Dalton Trans.* **2010**, *39* (48), 11628. https://doi.org/10.1039/c0dt00817f

120 Klepper, K. B.; Nilsen, O.; Hansen, P.-A.; Fjellvåg, H. Atomic Layer Deposition of Organic–Inorganic Hybrid Materials Based on Saturated Linear Carboxylic Acids. *Dalton Trans.* **2011**, *40* (17), 4636. https://doi.org/10.1039/c0dt01716g

121 Yang, F.; Brede, J.; Ablat, H.; Abadia, M.; Zhang, L.; Rogero, C.; Elliott, S. D.; Knez, M. Reversible and Irreversible Reactions of Trimethylaluminum with Common Organic Functional Groups as a Model for Molecular Layer Deposition and Vapor Phase Infiltration. *Adv. Mater. Interfaces* **2017**, *4* (18), 1700237. https://doi.org/10.1002/admi.201700237

122 Niemelä, J.-P.; Karppinen, M. Tunable Optical Properties of Hybrid Inorganic–Organic $[(TiO_2)_m(Ti–O–C_6H_4–O–)_k]_n$ Superlattice Thin Films. *Dalton Trans.* **2015**, *44*, 591–597. https://doi.org/10.1039/C4DT02550D

123 Li, Y.; Fu, Q.; Yu, S.; Yan, M.; Berglund, L. Optically Transparent Wood from a Nanoporous Cellulosic Template: Combining Functional and Structural Performance. *Biomacromolecules* **2016**, *17* (4), 1358–1364. https://doi.org/10.1021/acs.biomac.6b00145

124 Zhu, M.; Song, J.; Li, T.; Gong, A.; Wang, Y.; Dai, J.; Yao, Y.; Luo, W.; Henderson, D.; Hu, L. Highly Anisotropic, Highly Transparent Wood Composites. *Adv. Mater.* **2016**, *28* (26), 5181–5187. https://doi.org/10.1002/adma.201600427

125 Frey, M.; Widner, D.; Segmehl, J. S.; Casdorff, K.; Keplinger, T.; Burgert, I. Delignified and Densified Cellulose Bulk Materials with Excellent Tensile Properties for Sustainable Engineering. *ACS Appl. Mater. Interfaces* **2018**, *10* (5), 5030–5037. https://doi.org/10.1021/acsami.7b18646

126 Phuinthiang, P.; Trinh, D. T. T.; Channei, D.; Ratananikom, K.; Sirilak, S.; Khanitchaidecha, W.; Nakaruk, A. Novel Strategy for the Development of Antibacterial

TiO_2 Thin Film onto Polymer Substrate at Room Temperature. *Nanomaterials* **2021**, *11* (6), 1493. https://doi.org/10.3390/nano11061493

127 Zhang, H.; Zhang, J.; Su, G.; Zhou, T.; Zhang, A. Ultraviolet Photodetector on Flexible Polymer Substrate Based on Nano Zinc Oxide and Laser-Induced Selective Metallization. *Compos. Sci. Technol.* **2020**, *190*, 108045. https://doi.org/10.1016/j.compscitech.2020.108045

128 Javed, T.; Afzal, I.; Shabbir, R.; Ikram, K.; Zaheer, M. S.; Faheem, M.; Ali, H. H.; Iqbal, J. Seed Coating Technology: An Innovative and Sustainable Approach for Improving Seed Quality and Crop Performance. *J. Saudi Soc. Agric. Sci.* **2022**, *21* (8), 536–545. https://doi.org/10.1016/j.jssas.2022.03.003

EUSKAL HERRIKO UNIBERTSITATEA - UNIVERSIDAD DEL PAIS VASCO

MATERIALEN FISIKA SAILA - DEPARTAMENTO DE FÍSICA DE MATERIALES

SUPPORTING INFORMATION

Marina Borraz Casanova
PhD Thesis

Thesis supervisors:
Prof. Dr. Mato Knez
Dra. Catalina Mansilla Sánchez

Donostia-San Sebastián, 2025

CambridgeNanoTech
Simply ALD

Al_2O_3 – Aluminum Oxide

Savannah Film Recipe

Precursors:

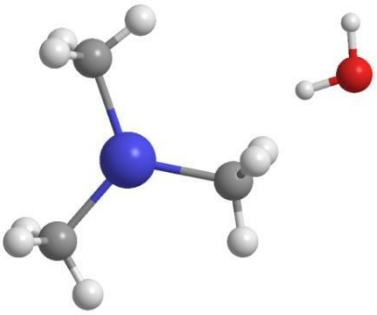

Trimethylaluminum, TMA, $Al(CH_3)_3$
CAS #: 75-24-1

Water, H_2O

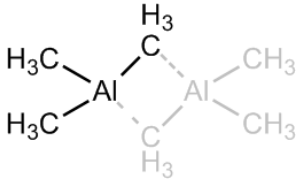

Note: Both Trimethylaluminum (TMA) and H_2O are unheated

300°C growth:
9=300°C, 8=270°C, 6=7=10=150°C, flow=20sccm

pulse H_2O (valve 0), 0.015 s
wait 4 s
pulse TMA (valve 1), 0.015 s
wait 4 s

Growth rate: ~1.0Å / cycle at 300°C on silicon

	Instruction	#	Value
0	flow		20
1	heater	9	300
2	heater	8	270
3	stabilize	9	
4	stabilize	8	
5	wait		600
6	pulse	0	0.015
7	wait		4
8	pulse	1	0.015
9	wait		4
10	goto	6	m
11	flow		5

250°C growth:
9=250°C, 8=250°C, 6=7=10=150°C, flow=20sccm

pulse H_2O (valve 0), 0.015 s
wait 5 s
pulse TMA (valve 1), 0.015 s
wait 5 s

Growth rate: ~1.07Å / cycle at 250°C on silicon

	Instruction	#	Value
0	flow		20
1	heater	9	250
2	heater	8	250
3	stabilize	9	
4	stabilize	8	
5	wait		600
6	pulse	0	0.015
7	wait		5
8	pulse	1	0.015
9	wait		5
10	goto	6	m
11	flow		5

One Kendall Square, Suite B7301
Cambridge, MA 02139, USA

T: 617-674-8800
F: 617-674-8850
www.cambridgenanotech.com

CambridgeNanoTech
Simply ALD

200°C growth:
9=200°C, 8=200°C, 6=7=10=150°C, flow=20sccm

pulse H_2O (valve 0), 0.015 s
wait 8 s
pulse TMA (valve 1), 0.015 s
wait 8 s

Growth rate: ~1.06Å / cycle at 200°C on silicon

	Instruction	#	Value
0	flow		20
1	heater	9	200
2	heater	8	200
3	stabilize	9	
4	stabilize	8	
5	wait		600
6	pulse	0	0.015
7	wait		8
8	pulse	1	0.015
9	wait		8
10	goto	6	m
11	flow		5

150°C growth:
9=150°C, 8=150°C, 6=7=10=150°C, flow=20sccm

pulse H_2O (valve 0), 0.015 s
wait 20 s
pulse TMA (valve 1), 0.015 s
wait 20 s

Growth rate: ~1.07Å / cycle at 150°C on silicon

	Instruction	#	Value
0	flow		20
1	heater	9	150
2	heater	8	150
3	stabilize	9	
4	stabilize	8	
5	wait		600
6	pulse	0	0.015
7	wait		20
8	pulse	1	0.015
9	wait		20
10	goto	6	m
11	flow		5

80°C growth:
9=80°C, 8=80°C, 6=7=10=150°C, flow=20sccm

pulse H_2O (valve 0), 0.015 s
wait 60 s
pulse TMA (valve 1), 0.015 s
wait 30 s

Growth rate: ~0.89Å / cycle at 80°C on silicon

	Instruction	#	Value
0	flow		20
1	heater	9	80
2	heater	8	80
3	stabilize	9	
4	stabilize	8	
5	wait		1200
6	pulse	0	0.015
7	wait		60
8	pulse	1	0.015
9	wait		30
10	goto	6	m
11	flow		5

CambridgeNanoTech
Simply ALD

Application notes:

Decomposition of $Al(CH_3)_3$ begins at temperatures above 375°C. ALD Al_2O_3 is readily deposited onto both planar and high aspect ratio structures. Refractive index = 1.62-1.69 varies on deposition temperature and film thickness.

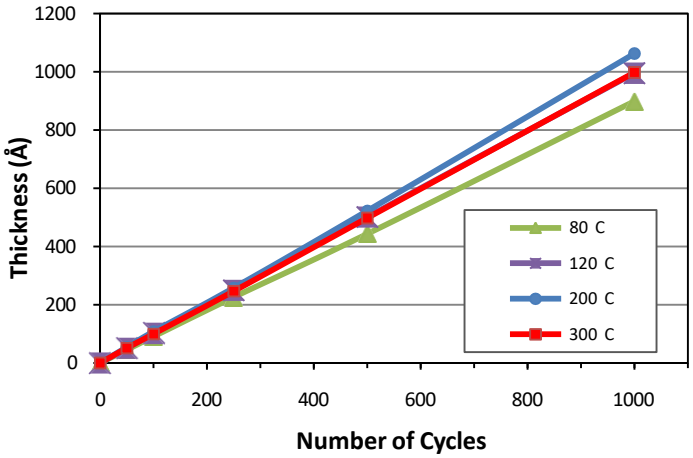

Figure 1: Linear ALD deposition of Al_2O_3 vs. deposition temperature.

Prefilled cylinders compatible with Savannah™ ALD reactors available from:

Strem Chemicals
http://www.strem.com/catalog/v/98-4003/1/

Sigma-Aldrich
http://www.sigmaaldrich.com/catalog/ProductDetail.do?N4=663301|ALDRICH&N5=SEARCH_CONCAT_PNO|BRAND_KEY&F=SPEC

CambridgeNanoTech
Simply ALD

ZnO – Zinc Oxide

Savannah Film Recipe

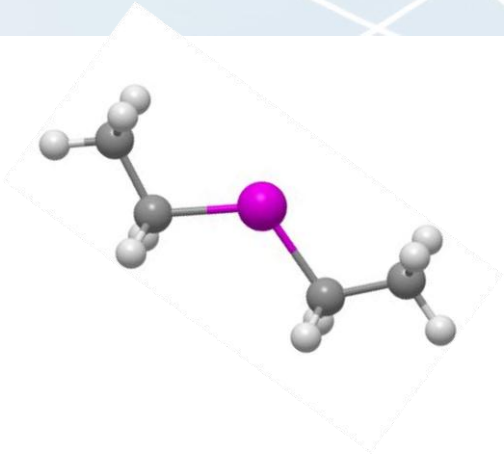

Precursrors:

Diethyl Zinc, DEZn, $ZnEt_2$, $(C_2H_5)_2Zn$
CAS Number: 557-20-0
Unheated

H_2O, unheated

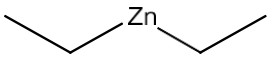

250°C growth
8=9=250°C, 6=7=10=150°C, flow=20sccm

pulse H_2O (Valve 0), 0.015 s
wait 5 s
pulse DEZn (Valve 1) , 0.015 s
wait 5 s

Growth rate per cycle: 1.01Å /cycle on silicon

	Instruction	#	Value
0	flow		20
1	heater	9	250
2	heater	8	250
3	stabilize	9	
4	stabilize	8	
5	wait		600
6	pulse	0	0.015
7	wait		5
8	pulse	1	0.015
9	wait		5
10	goto	6	m
11	flow		5

200°C growth
8=9=200°C, 6=7=10=150°C, flow=20sccm

pulse H_2O (Valve 0), 0.015 s
wait 10 s
pulse DEZn (Valve 1) , 0.015 s
wait 10 s

Growth rate per cycle: 1.46Å /cycle on silicon

	Instruction	#	Value
0	flow		20
1	heater	9	200
2	heater	8	200
3	stabilize	9	
4	stabilize	8	
5	wait		600
6	pulse	0	0.015
7	wait		10
8	pulse	1	0.015
9	wait		10
10	goto	6	m
11	flow		5

One Kendall Square, Suite B7301
Cambridge, MA 02139, USA

T: 617-674-8800
F: 617-674-8850
www.cambridgenanotech.com

CambridgeNanoTech
Simply ALD

150°C growth
8=9= 150°C, 6=7=10=150°C, flow=20sccm

pulse H_2O (Valve 0), 0.015 s
wait 20 s
pulse DEZn (Valve 1) , 0.015 s
wait 20 s

Growth rate per cycle: 1.66Å /cycle on silicon

	Instruction	#	Value
0	flow		20
1	heater	9	150
2	heater	8	150
3	stabilize	9	
4	stabilize	8	
5	wait		600
6	pulse	0	0.015
7	wait		20
8	pulse	1	0.015
9	wait		20
10	goto	6	m
11	flow		5

120°C growth
8=9= 120°C, 6=7=10=150°C, flow=20sccm

pulse H_2O (Valve 0), 0.015 s
wait 30 s
pulse DEZn (Valve 1) , 0.015 s
wait 30 s

Growth rate per cycle: 1.72Å /cycle on silicon

	Instruction	#	Value
0	flow		20
1	heater	9	120
2	heater	8	120
3	stabilize	9	
4	stabilize	8	
5	wait		1200
6	pulse	0	0.015
7	wait		30
8	pulse	1	0.015
9	wait		30
10	goto	6	m
11	flow		5

80°C growth
8=9= 80°C, 6=7=10=150°C, flow=20sccm

pulse H_2O (Valve 0), 0.015 s
wait 60 s
pulse DEZn (Valve 1) , 0.015 s
wait 60 s

Growth rate per cycle: 1.2Å /cycle on silicon

	Instruction	#	Value
0	flow		20
1	heater	9	80
2	heater	8	80
3	stabilize	9	
4	stabilize	8	
5	wait		1200
6	pulse	0	0.015
7	wait		60
8	pulse	1	0.015
9	wait		60
10	goto	6	m
11	flow		5

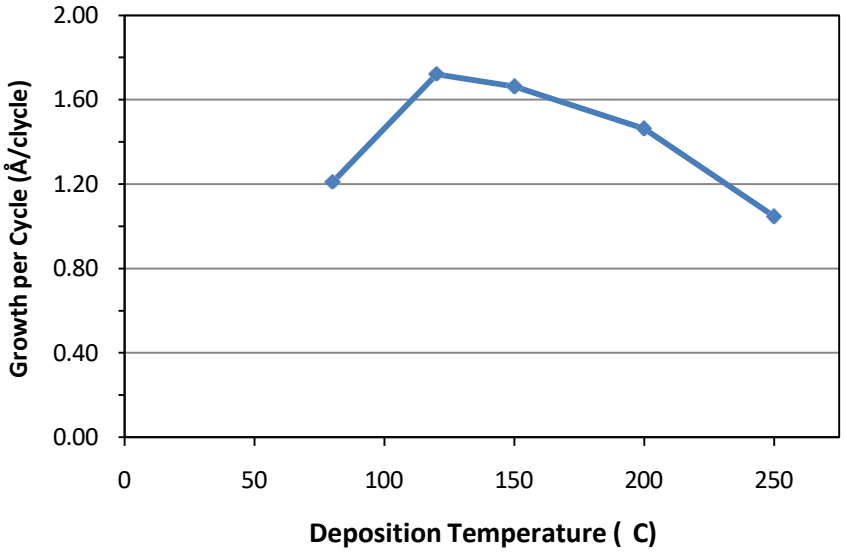

Figure 1: Deposition rate of ZnO versus deposition temperature.

Application notes:
The refractive index (RI) of ALD deposited ZnO varies between 1.9 and 2.0 depending on thickness and deposition temperature (thinner films under 20nm have RI closer to 1.93). Many papers have been published evaluating ZnO deposited on Savannah systems. For example:
http://www.cambridgenanotech.com/customers/customerpapers.php?searchfor=ZnO

Prefilled cylinders of $ZnEt_2$ compatible with Savannah™ ALD reactors available from:

Strem Chemicals
http://www.strem.com/catalog/v/98-4000/84/

Sigma-Aldrich
http://www.sigmaaldrich.com/catalog/ProductDetail.do?N4=668729|ALDRICH&N5=SEARCH_CONCAT_PNO|BRAND_KEY&F=SPEC